NUCLEAR DYNAMICS AND IONIZATION OF DIATOMIC MOLECULES IN INTENSE LASER FIELDS

by

MAIA MAGRAKVELIDZE

B.S., Ivane Javakhishvili Tbilisi State University, Georgia, 2003
M.S., Ivane Javakhishvili Tbilisi State University, Georgia, 2005

A THESIS

submitted in partial fulfillment of the
requirements for the degree

MASTER OF SCIENCE

Department of Physics
College of Arts and Sciences

KANSAS STATE UNIVERSITY
Manhattan, Kansas

2009

Approved by:
Major Professor
Uwe Thumm

Abstract

In this work we studied the dynamics of deuterium molecules in intense laser fields both experimentally and theoretically. For studying the dynamics of the molecule on a time scale that is less than the period of the laser field (2.7 fs for 800 nm), an advanced experimental technique: COLTRIMS (cold target recoil ion momentum spectroscopy) was used. COLTRIMS allows studying the nuclear dynamics without using attosecond laser pulses.

This thesis consists of two main parts. In the first part we deduced the angular dependence of the ionization probability of the molecule without aligning the molecules, by measuring the relative angle between a deuteron resulting from field dissociation and an emitted electron using electron-ion coincidence measurements with circularly polarized light in COLTRIMS. We found out that for 50 fs pulses (1850 nm wavelength and 2 $x10^{14}$ W/cm^2 intensity), D_2 molecules are 1.15 times more likely to be ionized when the laser field is parallel to the molecular axis than when the laser field is perpendicular. This result agreed perfectly with the result from our *ab initio* theoretical model and also with predictions of the molecular Ammosov-Delone-Krainov (mo-ADK) theory.

In the second part of this work we calculated the time evolution of an initial nuclear wave packet in D_2^+ generated by the rapid ionization of D_2 by an ultrashort laser pulse. We Fourier transformed the nuclear probability density with respect to the delay between the pump and probe pulses and obtained two-dimensional internuclear-distance-dependent power spectra which serve as a tool for visualizing and analyzing the nuclear dynamics in D_2^+ in an external laser field. We attempt to model realistic laser pulses, therefore in addition to the main spike of the pulse we include the Gaussian pedestal. The optimal laser parameters for observing field-induced bond softening and bond hardening in D_2^+ can be achieved by varying the intensity, wavelength, and duration of the probe-pulse pedestal. Despite the implicit “continuum wave” (*infinite* pulse length) assumption the validity of the “Floquet picture” is tested for the interpretation of short-pulse laser-molecule interactions.

Table of Contents

List of Figures

List of Tables

Acknowledgements

First of all I want to express my deepest gratitude to Dr. Igor Litvinyuk, and Dr. Uwe Thumm for giving me the chance to pursue my masters at Kansas State University, for their guidance and outstanding support during all stages of this work and for being so understanding.

I am very grateful to Dr. Lew Cocke for giving me valuable guidance and advice and for being so patient with me.

I wish to thank all my teachers past and present for all that they have taught me.

I am thankful to support staff starting with Scott Chainey, and Bob Krause, for being so supportive and helpful, Al Rankin, Mike Wells, Mark Newman, Peggy Matthews and Jane Peterson for being so patient and helpful. Also thanks to Joe Prockish and Larry McFeeters.

Thanks to my colleagues, Chakra Maharjan, Ben Gramkow, Irina Bocharova, Dipanwita Ray, Cao Wei, Sankar De, Kamal Singh, and Feng He for being there for me.

Finally, I heartily thank my family for all the encouragement and emotional support. My father would be very proud of me.

Dedication

To my father Guram Magrakvelidze.

Preface

“The most incomprehensible thing about the world is that it is comprehensible.”

Albert Einstein.

CHAPTER 1 - Introduction

The interaction of intense lasers with atoms and molecules has been a very important topic in current research in atomic and molecular physics. The length and time scales of the interactions are orders of magnitude less than those in our life. The typical length scales are less than 1 nanometer for small molecules, and time scales vary from attosecond for electronic dynamics, to femtosecond for molecular vibration, and picosecond for molecular rotation. To trace all the processes that take place during these interactions short laser pulses are used. To access the sub-femtosecond time scale, pump-probe techniques are being further developed to track electrons on their natural attosecond time scale [7, 14, 29, 37, 51, 55].

Recent advances in femtosecond (fs) laser technology have made it possible to observe, control and study nuclear dynamics in small molecules [19, 32, 40, 49, 53, 76, 97]. The "pump-probe" experiments, which use short and intense time-delayed laser pulses, are performed in many laboratories [7, 10, 14, 29, 37, 51, 55, 64, 67, 84]. In these experiments a short pump pulse (with pulse lengths of only a few fs corresponding to the bandwidths that are larger than the vibrational level spacing) electronically excites or ionizes the neutral target molecule and also coherently excites a superposition of stationary vibrational states of the molecular ion, resulting in a moving nuclear wave packet. With the help of a second delayed probe pulse the probability density of the wave packet can be imaged. The probe pulse rapidly ionizes the molecular ion leading to its fragmentation by Coulomb explosion (CE) [25, 26, 38]. The fragments of the reaction are detected and kinetic-energy release (KER) spectra are measured [7, 37, 60, 70, 81]. From the KER spectra, the dynamics of the nuclear wave packet can be reconstructed.

In the presence of a strong laser field, molecules can undergo single or multiple ionization. The probability of strong field ionization strongly depends on the angle between the molecular axes and the electric field direction [4, 56]. It is important to know the angular dependence of molecular ionization in order to interpret the angle-resolved molecular high-harmonic spectra. Experimentally, the angular anisotropy can be measured by aligning the molecules first with a linearly polarized laser field [7, 56, 75]. Measuring the angular anisotropy of ionization by aligning the molecules has some limitations, such as limited degree of field-free alignment that can be achieved.

Recently, Staudte *et al.* [88] suggested an ingenious method for measuring the angular dependence of ionization without having to align the molecules first. They used circularly polarized light to ionize and dissociate the molecules (H_2), and then measured electrons and fragmented ions in coincidence. This method has a much higher resolution, and most importantly no alignment of molecules is required. We expanded this method using D_2 molecules ionized by 1850 nm laser pulses – deep in the tunneling ionization regime.

This thesis is arranged as follows. Chapter 2 covers some of the basic concepts and theory related to the behavior of atoms and molecules in "intense" or "strong" laser fields. In Chapter 3 we explain the laser parameters and experimental techniques used with an overview of the apparatus, experimental setup and procedures. We also cover the working details of the cold target recoil ion momentum spectroscopy (COLTRIMS) multi-hit spectrometer which provides us with a 4D solid angle collection for ions and low energy electrons, enabling high resolution ion and electron momentum measurements. Chapter 4 explains our data recording, data processing and how we calibrate our experimental parameters.

The first main part of this work (Chapter 5) is dedicated to a further investigation of the angular anisotropy of strong-field ionization in molecular hydrogen by extending the approach of Staudte *et al.* [88] to laser pulses of a longer wavelength (1850 nm) and using deuterium molecules as our target [57]. In this experiment, using electron - ion coincidence momentum spectroscopy and circularly polarized light, we measured the relative angle between an emitted electron and a deuteron without aligning the molecules first. The final direction of the drift momentum of the detached electron will be opposite to the vector potential of the laser field at the moment of ionization. Therefore, for circularly polarized light, the vector potential trails the rotating electric field vector by a quarter-cycle, so that ejected electrons will ultimately drift perpendicularly to the direction of the laser electric field at the moment of ionization. Bond softening (BS) is anisotropic with fragment momentum emerging mostly within a 10° angle from the plane of circular polarization [21], but for a rapidly rotating electric field vector there is no preferred direction within its polarization plane and the molecular axis direction within this plane is not affected by a circularly polarized pulse. By measuring the distribution of relative angles within the plane of polarization between an electron and a proton coming from the same molecule, one can determine the dependence of the ionization yield on the angle between the molecule and the rotating electric field vector [57].

The second main part of this work (chapter 6) is dedicated to theoretical studies of the dependence of BS and bond hardening (BH) on laser intensity, wavelength, and pulse duration using two-dimensional internuclear-distance-dependent power spectra [58]. Variation in the intensity, wavelength, and duration of this probe-pulse pedestal allows us to identify the optimal laser parameters for the observation of field-induced BS and BH in D_2^+. This also suggests a scheme for quantitatively testing the validity of the "Floquet picture", which is commonly used for the interpretation of short-pulse laser-molecule interactions, despite its implicit "continuum wave" (*infinite* pulse length) assumption.

Using CE mapping [26, 39], the experimental KER spectra [7, 37, 40, 55, 60, 81] can be compared to theoretical models for the nuclear probability densities [38, 66, 69, 70, 91]. For instance, in the case of the simplest diatomic molecules (such as H_2^+), the nuclear probability densities can be approximately constructed by a direct numerical solution of the time-dependent Schrödinger equation using wave-packet propagation techniques [7, 24, 38, 48, 66]. For example, in recent experiments [7, 37, 55], the dephasing of nuclear vibrational wave packets in D_2^+ over a period of a few vibrational cycles and its subsequent revivals after many vibrational cycles were observed, which confirmed earlier model calculations [38, 44]. In this example the nuclear wave packets evolution shows very interesting purely quantum mechanical phenomena even in the absence of external (laser electric) forces. Typically, nuclear wave function evolution is analyzed by recording KER spectra as a function of the pump-probe delay τ. Subsequent CE mapping gives the nuclear probability density $\rho(R,\tau)$ [7, 37]. Graphs of $\rho(R,\tau)$ capture the nuclear dynamics in space (R) and time (τ) and allow the distinction of several pump-laser-induced phenomena, such as molecular fragmentation into different asymptotic dissociation channels and the coherent dephasing and revival [79] of bound vibrational wave packets in diatomic molecular ions [7, 16, 38, 44, 62, 70, 81].

An alternative and less explored method for investigating the nuclear dynamics in diatomic molecules (and possibly in more complex molecules) is the time-series analysis of KER spectra. This method captures the nuclear dynamics in space and frequency domain and applies equally well to nuclear probability densities that are calculated or derived from measured KER spectra by CE mapping. This method is the focus of the investigation in chapter 6. In Chapter 7 the conclusions and final remarks are presented. Note that in chapters 2 through 5 SI units are used unless it is specified otherwise and in chapter 6 atomic units are used.

CHAPTER 2 - Background and Theory

In this chapter I will cover some of the basic concepts and theory related to the behavior of atoms and molecules in “intense” or “strong” laser fields. Intense laser fields are fields with a very high power density. Intense fields are created by concentrating energy in time (short pulses) generating high power and on a small area (focusing) generating high density.

Intense laser pulses are highly suitable for studying atoms and molecules. The labeling of a laser field as “intense” depends not just on the strength of the field, but also on the application. It is dependent on the properties of the molecular system as well as the frequency of the electric field. For example, in terms of the Rabi oscillations (the measure of the strength of laser electric field induced coupling of molecular levels), the field is considered intense if the Rabi-period is shorter than the interaction time. Quantitatively, a laser field is considered intense if its intensity is higher than 10^{13} W/cm^2 [76].

2.1. Atoms in Strong Laser Field

Over the last decade the study of atoms and molecules in intense electric fields has been growing very rapidly. Advances in the technology has led to the generation of short pulses with intensities in the order of the atomic unit (1a.u. = $3.5\text{x}10^{16}$ W/cm^2). The ionization dynamics of atoms and molecules have been studied in great detail. In this section the single and double ionization of an atom by a laser field will be discussed.

2.1.1 Single Ionization

Single ionization is the most basic ionization process. In this ionization process an atom or molecule absorbs one or several photons with a total energy greater than the ionization potential of the atom or the molecule, and the electron takes away the excess energy. When the ionization potential is greater than photon energy, generally three different processes can happen (Fig. 2.1):

- ✓ Multiphoton Ionization
- ✓ Tunneling Ionization
- ✓ Over the Barrier Ionization

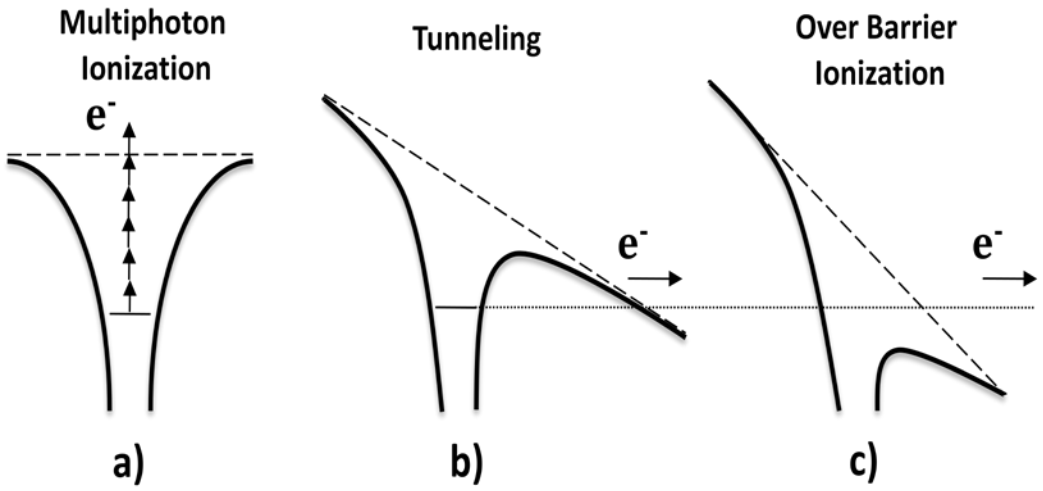

Fig. 2.1. Schematics of the ionization mechanisms in atoms.
a) For multiphoton ionization the laser field is not strong enough to sufficiently disturb the atom's potential. Ionization happens by absorbing several photons, overcoming the ionization potential. b) For higher intensity the potential shape changes sufficiently so that the electron wave packet can tunnel out. c) For higher intensity the laser field shapes the potential so that the electron is no longer bound and can overcome the barrier.

All the above processes can be described using the "Keldysh parameter". The ratio of the laser frequency to the tunneling frequency is known as the adiabaticity or the Keldysh parameter and is used to determine which ionization mechanism is dominant,

$$\gamma = \frac{\omega_{laser}}{\omega_{tun\ nel}} = \sqrt{\frac{I_p}{2U_p}} \tag{2.1}$$

where I_p is the atom's ionization potential, $U_p = I/4\omega^2$ is the ponderomotive energy (I is the laser intensity and ω is its angular frequency). For linearly polarized light, the ponderomotive energy can be expressed as

$$U_p = e^2 E_0^2/4m_e\omega^2 = 9.33 \times 10^{-14} I\lambda^2\ [eV], \tag{2.2}$$

where λ is expressed in μm and intensity in W/cm^2.

In 1965 in his early works Keldish [52] showed that all three mechanisms are just different sides of the same universal process: nonlinear ionization. While multiphoton ionization

can be treated appropriately using the perturbation theory [54, 76], the tunneling ionization needs a classical treatment of the field. To distinguish between these two regimes, Keldish examined the time needed for an electron to pass under the potential barrier at the unperturbed initial-state energy (assuming that electron velocity is $v = \sqrt{I_p/m_e}$, and the barrier width is $l = I_p/(eE)$).

$$t = \frac{\sqrt{2m_e I_p}}{eE} = \omega_{tunnel}^{-1} \tag{2.3}$$

where Ip is the ionization potential and E the instantaneous electric field strength, m_e and e are the electron mass and charge. Now, one can see that

i) if the oscillation period is small compared to the tunneling time, then ionization would have to be treated perturbatively in the multiphoton picture and correspondingly

$$\gamma \gg 1 \quad \text{corresponds to multiphoton ionization} \tag{2.4}$$

ii) if the oscillation period of the external electric field is large compared to the "tunneling time", then tunneling can occur and

$$\gamma \ll 1 \quad \text{corresponds to tunneling .} \tag{2.5}$$

2.1.1.1 Multi-photon process

At low intensities (<10^{13} W/cm^2), when $\gamma \gg 1$, we are in the multiphoton regime (Fig. 2.1 a). In this regime the ionization potential is high and the tunneling time is greater than the oscillation period of the field.

During a cycle of the laser field, the electron may gather sufficient energy to leave the atomic potential well. The ionization rate is given as

$$\omega_n = \sigma_n I^n \tag{2.6}$$

where I is the intensity and σ_n is the generalized n-photon ionization cross section [50]. The relation (2.6) is very difficult to test in an experiment because of the physical properties of the laser beam (such as focal volume, intensity). The power law (2.6) is not valid when the depletion of the initial state is non-negligible.

If an atom or molecule absorbs more photons than required for ionization, the process is called *Above Threshold Ionization* (ATI). This process was first reported by Agostini *et al.* [2] thirty years ago. A typical ATI electron energy spectrum is given on Fig. 2.2 where the peaks are separated by the photon energy. The ionization rate is given as:

$$\omega_{n+s} \sim I^{n+s} \tag{2.7}$$

where s is the number of excess photons absorbed. The photoelectron energy can be calculated from the extended Einstein photo effect formula

$$E = (n + s)\,\hbar\omega - I_p. \tag{2.8}$$

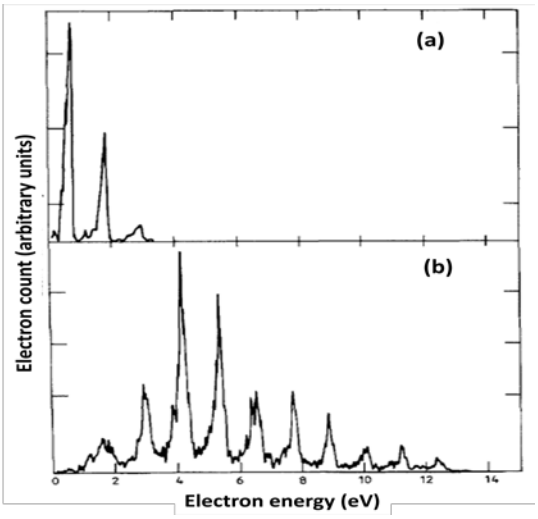

Fig. 2.2 ATI electron energy spectra of Xe with λ=1064 nm, 130 ps laser pulses (adapted from G. Petite et al. [75]) (a) I = 2.2 x 10 ^{12} W/cm^2; (b) I = 1.1 x 10^{13} W/cm^2

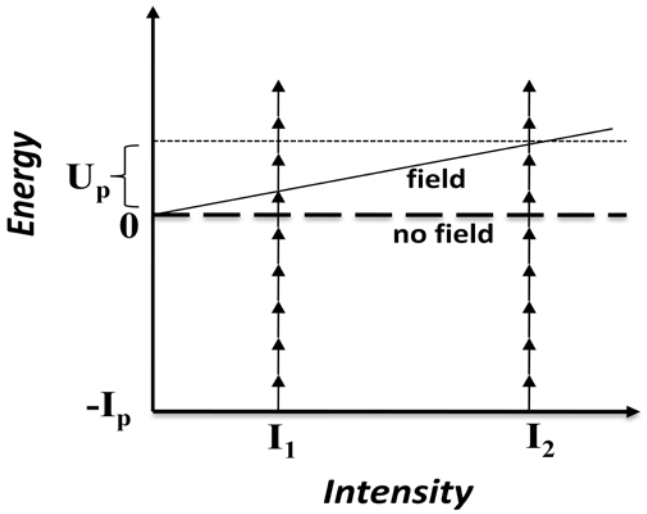

Fig. 2.3 Illustration of the Stark shift of the ionization potential depending on laser intensity.

A remarkable feature of ATI is the suppression of the low energy peaks (see Fig. 2.2) in the photoelectron spectra. By increasing the laser intensity, lower peaks start to get suppressed. The reason for this is the AC-Stark shift of the energies of atomic states in the presence of the

external field. This shift is characterized by the electron ponderomotive energy U_p. The ionization barrier is boosted by U_p in the laser field (Fig. 2.3) and the final photoelectron energy is given by

$$E = (n + s)\,\hbar\omega - (I_p + U_p). \tag{2.9}$$

A typical photoelectron spectrum at high intensities has several features of interest (Fig. 2.4): an intensity-independent part at lower energy and a plateau continuing up to a cutoff energy. Energies 0-2U_p corresponds to "direct electrons". A semi-classical theory (where the electron is treated quantum mechanically when ionizing though tunneling from the parent ion and electrons dynamics after tunneling is treated classically) has explained some of the high energy features, in particular the plateau and the well defined cut off energy at 10 U_p [71].

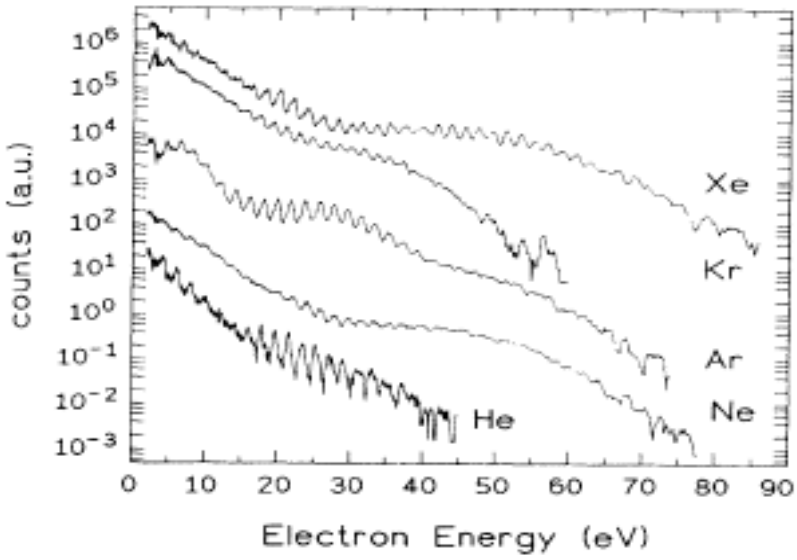

Fig. 2.4 Typical ATI spectra for noble-gas atoms.
The plateau feature results from elastic electron re-scattering [72].

2.1.1.2 Tunneling ionization

When γ**<1** (Fig. 2.1 (b)) we are in the tunneling ionization regime. In this regime, the laser period is greater than the tunneling time and so the laser field is treated classically. The tunneling regime is dominant at low laser frequencies. Unlike the multi-photon process, which involves the transition between states with different energies, tunneling is associated with the transition through a barrier, where the initial and final states have the same total energy. If the

laser field is strong enough to distort the Coulomb potential (at intensities between 10^{14} and 10^{15} W/cm^2) it is possible for the electron to tunnel through the barrier formed by the suppressed atomic potential.

One of the most commonly used theories in the tunneling ionization regime is the Amosov, Delane and Krainov (**ADK**) theory of ionization in intense laser fields. In this theory the electric field is treated as quasi-static because it is assumed that substantial ionization occurs in a short period (a fraction of an optical cycle). The basic point of the ADK model is that the ionization rate depends critically on the ionization potential of an atom [3].

The tunneling ionization ADK rate in atomic units is given as [20]

$$\varpi_{ADK} = \left(\frac{3e}{\pi}\right)^{3/2} \frac{Z^2}{n^{*9/2}} \left(\frac{4eZ^3}{n^{*4}F}\right)^{2n^*-3/2} \exp\left(-\frac{2Z^3}{3n^{*3}F}\right) \qquad (2.10)$$

where e=2.718, F is amplitude of the laser field, Z is ionic charge and n^* is effective quantum number which is expressed as:

$$n^* = \frac{Z}{\sqrt{2I_p}} \qquad (2.11)$$

To find the field strength one can use the formula:

$$F = \left(\frac{Intensity \cdot in \cdot W/cm^2}{3.51x10^{16}}\right)^{1/2}. \qquad (2.12)$$

The ionization rates found from these expressions agree closely with experimental results in the case of single ionization [20], but often disagree with them for double ionization [76].

2.1.1.3 Over the Barrier ionization

If we increase the laser intensity enough, eventually we reach the critical value for OB ionization. Beyond this value the Coulomb potential is strongly suppressed so that the ground state is no longer bound. In this regime (Fig. 2.1.c) the electron escapes from the potential well. Going from the tunneling regime to OB ionization regime, the ionization rate grows smoothly and reaches unity for a single pulse cycle. [76].

2.1.2 Double Ionization

In double ionization, two electrons are removed from the target atoms by a short laser pulse. Double ionization of atoms or molecules is classified as either sequential or nonsequential, depending on the intensity of the laser.

In sequential ionization both electrons are released by the field one after another at different phases of the laser pulse. The electrons can be released sequentially either by tunneling ionization or by OB ionization. The sequential process has been quantitatively explained with ADK rates [3]. Several experimental papers [28, 85, 94] showed clearly that the double ionization yield (plotted vs. intensity) had a knee part in the lower part of the intensity (Fig. 2.5).

The increase in double ionization yield was attributed to a new process called “Non-Sequential Double Ionization (NSDI)”. The theoretical explanation of the knee structure was first suggested by Corkum [28] and Kulander with co-workers [85]. The model is known as “Rescattering” or “Simple man’s” model and consists of three steps.

In the first step, the electron tunnels through the potential barrier and tunneling is treated quantum mechanically. Secondly, the freed electron then propagates in the laser field. The motion of the electron in the field is treated classically. Lastly, after a reverse of the field direction electron comes back to the ion core and depending on the electron’s energy it can either recombine with ion releasing excess energy, excite or knock out another electron. The excited second electron may be ionized by the field. The rescattering process depends on the laser polarization. There is no rescattering in a circularly polarized field because in this type of polarization the electron does not go back to the parent ion. Thus in non-sequential ionization one of the electrons tunnels out from the atom and is then driven back to the ion core due to the changing field direction, knocking out a second electron if it carries sufficient energy on the return [6].

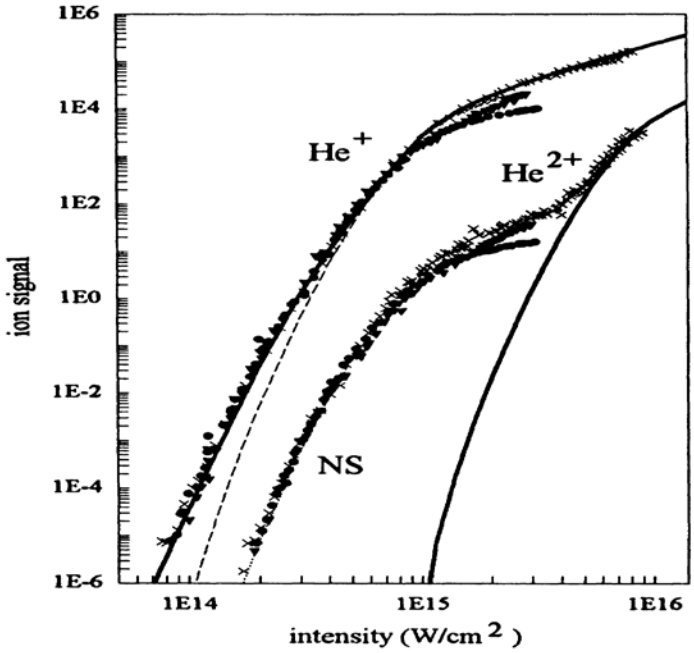

Fig. 2.5 Intensity dependence of the single and double ionization yield of He for linearly polarized, 100 fs, 780 nm laser pulse. The solid line shows the rate calculated in an independent event model (sequential) (From [94]).

2.1.2.1 Simple man's theory

In this section details of the Simple man's model proposed by Paul Corkum [30] will be discussed. As discussed above, after tunneling, the electron is treated classically (also neglecting the electron ion interactions). In an electromagnetic field, the Lorentz force acting on an electron

$$\vec{F} = e(\vec{E} + \vec{v} \times \vec{B}) \tag{2.13}$$

where v is the electron velocity and e is it's charge. For typical laser intensities of 10^{13}-10^{16} W/cm^2 and a wavelength of 800 nm, the velocity of the electron is much smaller than the speed of light, so we can neglect the magnetic field and write the electric fields as:

$$\vec{E} = e\overrightarrow{E_0}cos\omega t \tag{2.14}$$

where ω is the frequency of the field. Assuming that the field is polarized only in z direction, we have

$$m\dot{v}_x = 0\,, \qquad m\dot{v}_y = 0, \qquad m\dot{v}_z = \mathrm{eE_0(t)cos\omega t} \tag{2.15}$$

Assuming further that electron starts from position z=0 at time t_0, one can integrate (2.15) to get

$$v_z(t) = \frac{e}{m\omega} E_0(sin\omega t - sin\omega t_0) \tag{2.16}$$

$$z(t) = \frac{e}{m\omega^2} E_0 (cos\omega t_0 - cos\omega t - \omega(t - t_0) sin\omega t_0). \quad (2.17)$$

The plot of equation (2.17) is given on Fig. 2.6. The electron returns to the ion core at time $t_r > t_0$ if $z(t_r) = 0$. This equation cannot be solved analytically and has to be solved numerically. From equation (2.16) we can write the expression for kinetic energy

$$E_{kin}(t) = 2U_p (sin\omega t - sin\omega t_0)^2 \quad (2.18)$$

where U_p is defined as in equation (2.2).

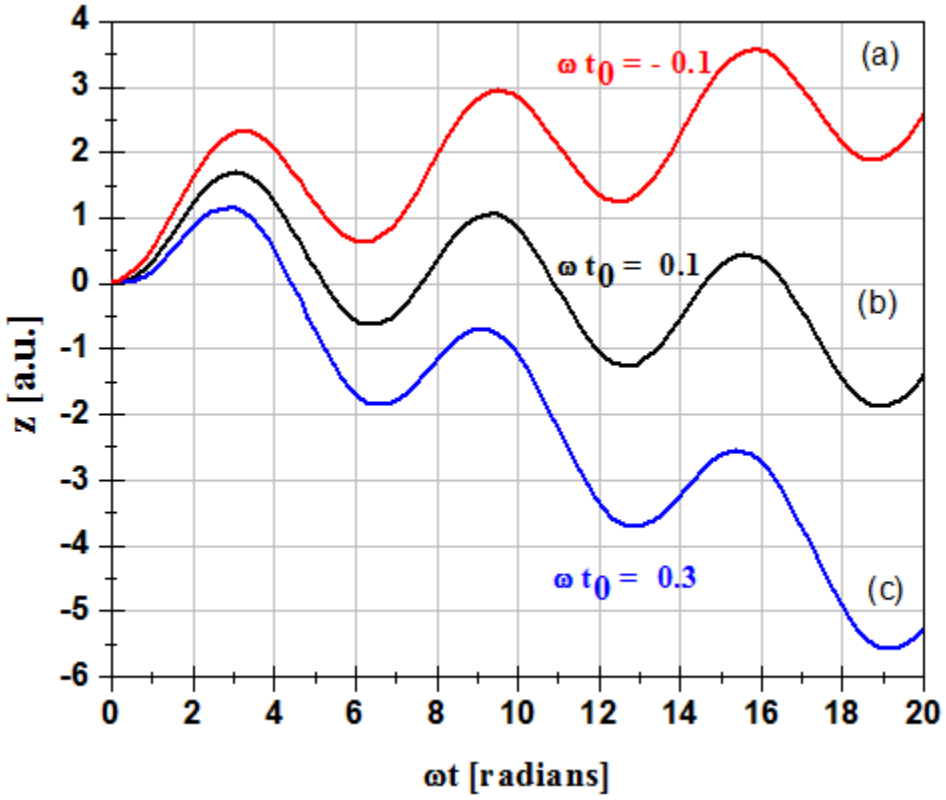

Fig. 2.6. Motion of the electron along z direction from equation (2.17)
For different initial times ωt_0= - 0.1, 0.1 and 0.3. (a) in this case electron never comes back to ion core, (b) electron will come back multiple times and (c) electron comes back single time (Initial phases for each cases).

The numerical solution for $z(t_r) = 0$ is given in Fig. 2.7. One can see that the electron born at ωt=0.3 returns to the ion core with maximum kinetic energy, and that value of energy gained after first revisit is $3.17U_p$. We can see that electrons with maximum energy are only born at particular phase whereas electrons born at all other phases have two birth phases (short and long trajectories). Electrons born at phases corresponding to a value left of the energy peak $3.17U_p$ (Fig. 2.7) will have longer trajectories and electrons born at phases corresponding to the

values right of the energy peak will have shorter trajectories. For observing rescattering, electrons with shorter trajectories are more important, because from a quantum mechanical point of view the electron wave packet has less spread.

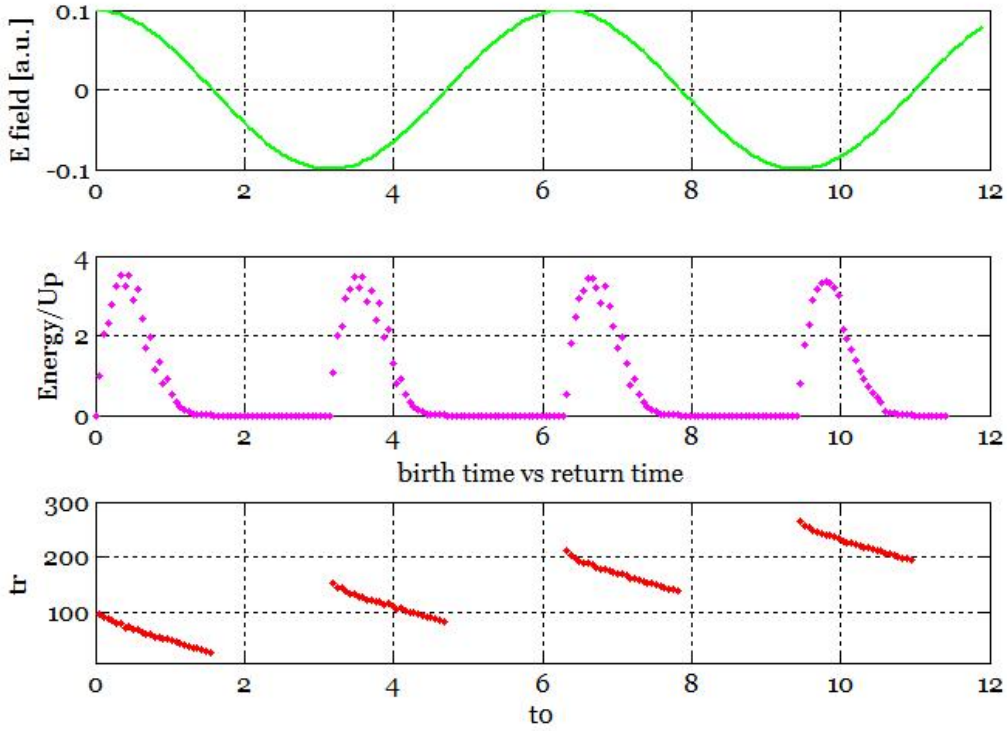

Fig. 2.7 Electric field used, maximum kinetic energy, and return phase all plotted as a function of birth phase (wt_0)
The first panel of the figure shows the electric field used (maximum value 0.1 a.u.) as a function of the time (more correct as a function of ωt phase). The second panel is showing the maximum kinetic energy that an electron can gain in the laser field as a function of the birth phase (ωt_0), and in the last panel the return phase (ωt_r), is plotted as a function of the birth phase (ωt_0).

2.2 Molecules in strong laser field

Interactions of a laser field with molecules are far more complicated than those involving atoms. The complexity of the interaction reveals new phenomena, which include above threshold dissociation (ATD), BS, BH and charge resonance enhanced ionization (CREI) which will be discussed in the next few sections.

2.2.1 Above Threshold Dissociation

Dissociation from low vibrational states results in ATD [45], which corresponds to the similar effect in atomic ionization called "above threshold ionization" (ATI) [2]. In the ATD process, molecules absorb more photons than required for dissociation, and the kinetic energy release (KER) spectrum has peaks separated by photon energy. ATD is marked with an arrow in Fig. 2.8. The dissociation would require extensive tunneling through the classically forbidden barrier and is very improbable at the given intensity. The more probable path for the fragmentation of the low vibrational states is ATD, which can happen through $2p\sigma_u$-3ω crossing (three photon absorption). The balance between ATD and one-photon absorption depends strongly on the initial vibrational state, laser frequency and intensity.

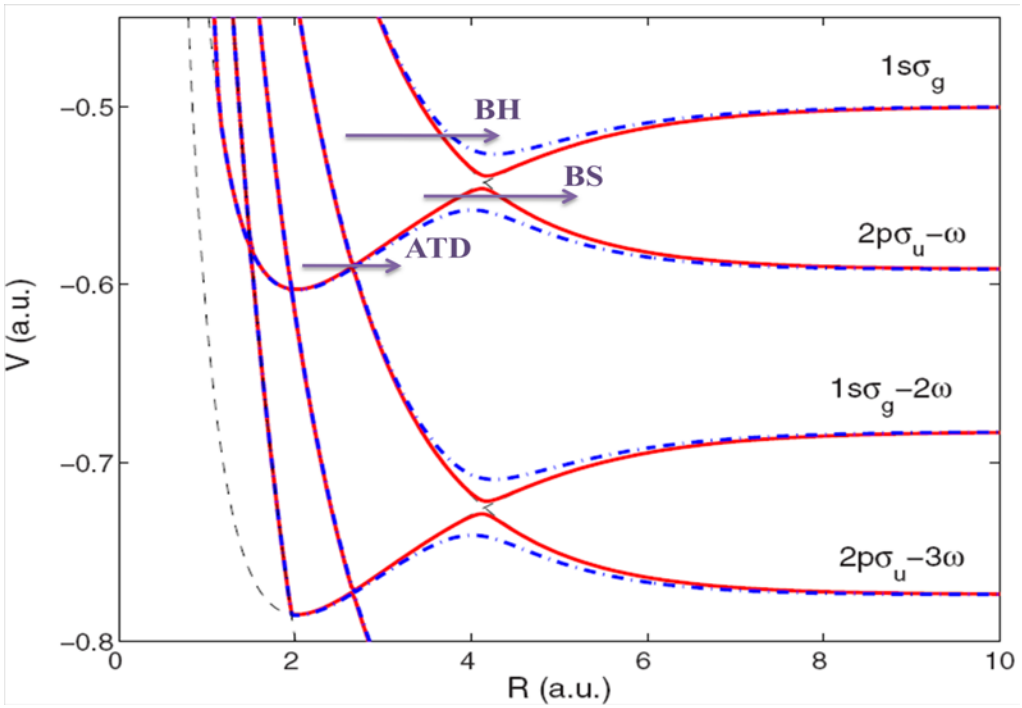

Fig. 2.8 Schematics of the ATD, BS, and BH processes (indicated with arrows). Thin black curves correspond to the field-free diabatic Floquet potentials for D_2^+. The field-dressed adiabatic molecular potential curves for D_2^+ are shown as solid red ($5x10^{11}$ W/cm^2) and blue dashed-dotted lines (10^{13} W/cm^2) for 500 nm cw laser field.

2.2.2 Bond Softening

At higher initial vibrational states there will be an intermediate energy value, which is above the adiabatic potential barrier, so that the molecule can dissociate over the barrier channel (Fig. 2.8.). This process was termed as "Bond Softening" by Bucksbaum *et al.* (1990) [21]. The main physics behind BS is simple. The molecule's bond "softens" in an intense laser field and the molecule dissociates. In Coulomb explosion, dissociation is caused by the sudden removal of electrons, whereas in BS the strength of the repulsion is quite gentle and doesn't involve the removal of any electrons. Molecular fragments typically have kinetic energies equivalent to or less than a single photon.

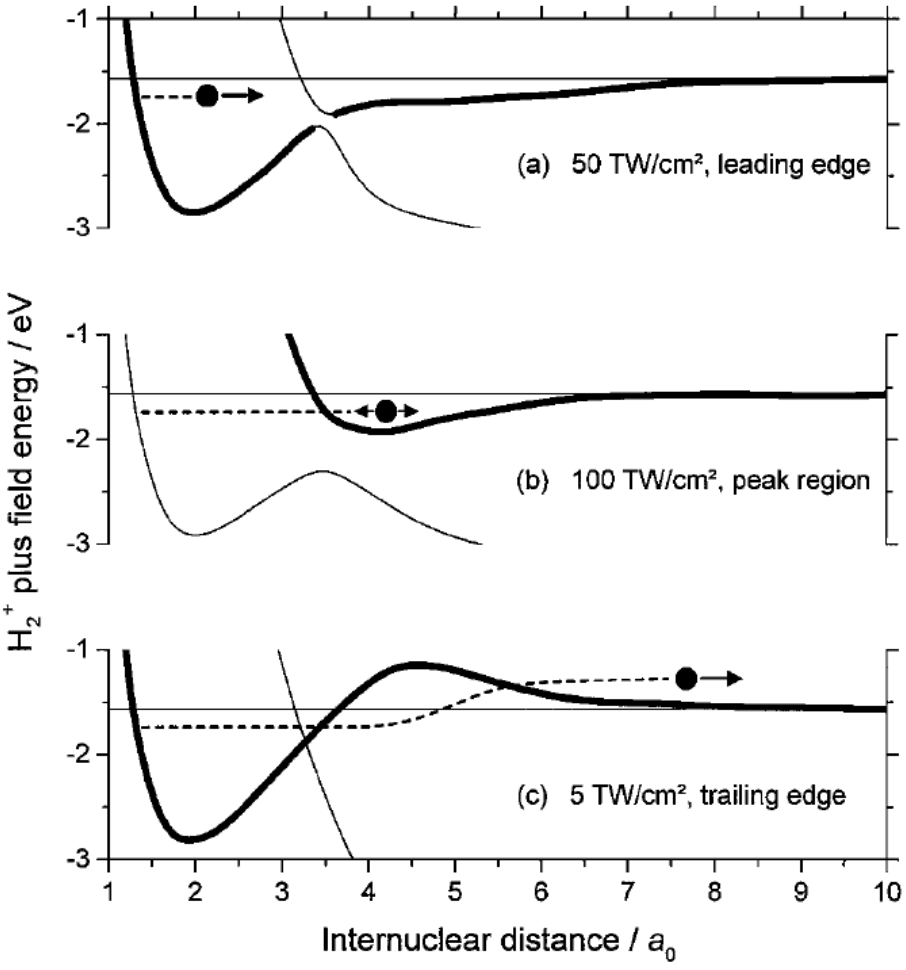

Fig. 2.9 The process of vibrational trapping of the wave packet (BH) above three-photon gap in the H_2^+ field –dressed potential curves.
From Frasinski at al. [42]

2.2.3 Bond Hardening

In the BH process, due to their weaker binding, high-lying vibrational states live longer than expected. As we go to higher initial vibrational levels, which lie above the crossing of the $1s\sigma_g$ and $2p\sigma_u$-ω curves in Fig. 2.8, the probability of photo-dissociation suddenly decreases because a portion of the initial vibrational population is "trapped" in the adiabatic well formed by the avoided crossing. BH depends on the intensity of the field, which determines the shape of the field-dressed adiabatic potential curves. If the intensity is too low, the adiabatic well will not be deep enough to trap the population. If the intensity is too high, the adiabatic well will be destroyed and the 'trapped' population will escape via the 1sσg asymptote and yield photo fragments with an unusually low kinetic energy (see Fig. 2.8).

The process of BH is illustrated in Fig. 2.9 [42]. Starting with the neutral molecule at an intensity of about 50 TW/cm^2, the wave packet is created in vibrational states just below the 1ω dissociation limit (Fig. 2.9(a)). This wave packet crosses the 3ω gap while the gap is still small. Most of the wave packet dissociates diabatically [42]. After some time the wave packet turns and comes back when the gap is wider and diabatic crossing is less probable and gets trapped in the laser-induced adiabatic state (Fig. 2.9(b)). All three processes described above (ATD, BS and BH) are often described with adiabatic Floquet potentials, and describe the dissociation of H_2^+ into p+H. CREI, on the other hand, describes breakup into p+p+e^- [86, 98].

2.2.4 Charge Resonance Enhanced Ionization

The experiments from the past one and a half decades reveal a particular sequential double ionization mechanism. In this mechanism the second ionization step always happens at a fixed range of internuclear distances [27, 31, 33, 89, 96].

The results were explained initially using BH [94], but no trapping was needed for interpreting the data [98]. The fact that the ionization probability is increased when the dissociating molecule passes a range of critical internuclear distances suggested that it was something else, which is now termed as CREI. At a critical internuclear distance the external field and the downhill ion potential together pull down the internuclear potential barrier sufficiently such that an electron localized on the uphill ion can escape.

CHAPTER 3 - Experiment

This section of the dissertation provides an overview of the experimental technique we used. Our aim was to study the ionization dynamics of atoms and molecules in an intense laser field. A multi-pass Ti:sapphire amplifier from the Kansas Light Source (KLS) (approx 1.5 mJ, 35 fs 800 nm pulses at a 1 kHz repetition rate) was used as the laser source and an Optical Parametric amplifier was used for wavelengths up to 2600 nm. For our electron ionization anisotropy experiments, we used 1850 nm laser pulses of 50 fs duration generated by a TOPAS optical parametric amplifier. The 1850 nm idler beam had approx 120 μJ of energy per pulse. The cold target recoil ion momentum spectroscopy (COLTRIMS) was used to detect the fragments of the molecules that we produced in the intense laser field. COLTRIMS allows us to detect both ions and electrons in coincidence.

3.1 Laser

The laser used in our experiments was a Ti:sapphire laser from KLS. This laser uses a titanium sapphire crystal and consists of two parts, the oscillator and the amplifier. The output laser beam is around 30 fs, 2 W and has a 1 kHz repetition rate. The electric field is assumed to have a Gaussian envelope:

$$E(t) = E_0 e^{-\left(\frac{t}{\tau}\right)^2} \cos(\omega t) \tag{3.1}$$

where ω, τ/2ln2 and E_0 represent the laser angular frequency, pulse duration (FWHM), and electric field amplitude respectively (see Fig. 3.1). An 800 nm, 3.5x10^{14} W/cm^2 laser pulse has about 11 cycles. The time averaged laser intensity is given as:

$$\mathrm{I} = \mathrm{I}_0 \mathrm{e}^{-2\mathrm{r}^2/\mathrm{w}^2}, \tag{3.2}$$

where w is the half width of the beam to the 1/e^2 intensity point, r is the radial distance from the center of the beam, I_0 is the intensity at the center of the field.

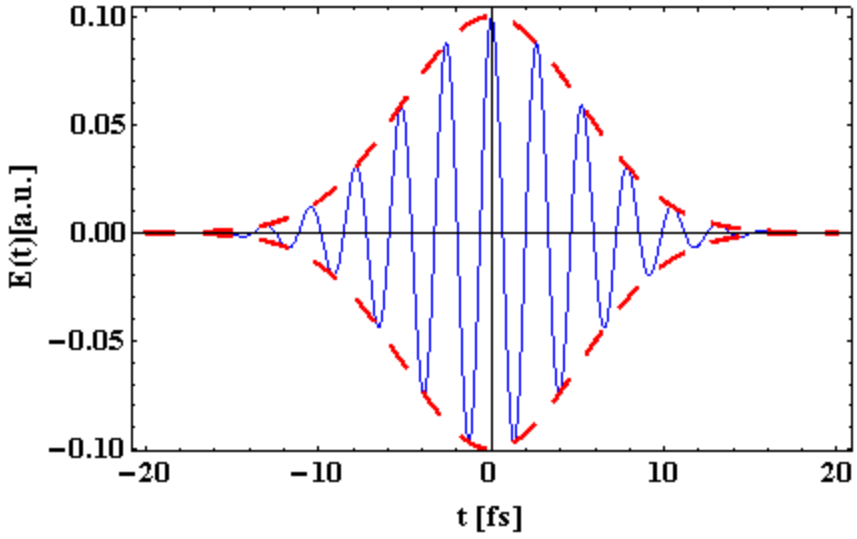

Fig. 3.1 Example of laser pulse of 10 fs FWHM and 800 nm wavelength. The amplitude of the electric field is 0.1a.u, which corresponds to 5.14x10^8 V/cm.

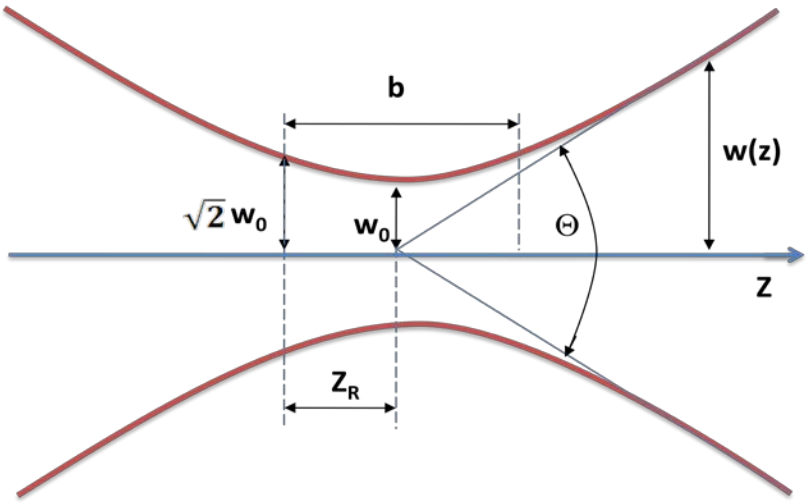

Fig. 3.2 The Gaussian beam width dependence on distance z. Θ is total angular spread, w_0 is the so-called beam waist radius, Z_R is the Rayleigh range, and b is the confocal parameter or depth.

The dependence of w on the axial distance z is shown on Fig. 3.2. Analytically it is given as

$$\begin{cases} w(z) = w_0\sqrt{1+\left(\frac{\lambda z}{\pi w_0}\right)^2} \\ w(z) = \frac{\lambda z}{\pi w_0} \quad \text{For } z \gg z_R \end{cases} \tag{3.3}$$

where z_R is the Rayleigh range [90],

$$z_R=\pi w_0^{\,2}/\lambda \ , \tag{3.4}$$

and the focal radius w_0 is related to the focal length f and beam radius w as for $z = z_R$. From (3.3) we have

$$w_0 = \frac{f\lambda}{\pi w(z)}, \qquad w(\pm z_R) = w_0\sqrt{2} \tag{3.5}$$

The distance between the two points corresponding to $z= \pm z_R$ is called the depth or focus of the beam: $b=2z_R$. The power passing through a circle of radius r in a plane perpendicular to the z direction can be written as

$$P(r,t) = P_0[1-\exp(-2r^2/w^2(z))] \tag{3.6}$$

where $P_0 = \frac{1}{2}\pi I_0 w_0^2$ is the total transmitted power. The peak intensity (corresponding to r=0) is the power passing through a circle of radius r in the limit $r\rightarrow 0$:

$$\begin{aligned} I(0,z) &= \lim_{r\to 0}\frac{P_0\left[1-\exp\left(-\frac{2r^2}{w^2(z)}\right)\right]}{\pi r^2} \\ &= \frac{P_0}{\pi}\lim_{r\to 0}\frac{\left[1-\exp\left(-\frac{2r^2}{w^2(z)}\right)\right]'}{[r^2]'} \\ &= \frac{P_0}{\pi}\lim_{r\to 0}\frac{\left[-(-2)(2r)\exp(-\frac{2r^2}{w^2(z)})\right]}{w^2(z)(2r)} \quad = \quad \frac{2P_0}{\pi w^2(z)}. \end{aligned}$$

This defines an effective area $A_{eff}=\pi w^2/2$.

The peak intensity at the focal point can be written as

$$I_0 = \frac{2P}{\tau R\pi w_0^2} \tag{3.7}$$

where P is the measured power (in the units of Watt), τ is pulse duration (sec) (~30 fs for long pulse), R is repetition rate (Hz) (1 kHz for our laser), and w_0 is beam radius (m).

3.2 COLTRIMS

COLTRIMS allows us to completely reconstruct vector momentum information for all the reaction fragments of an experiment. COLTRIMS consists of a gas jet, a spectrometer, and two time and position sensitive detectors sitting on both sides of the spectrometer. The spectrometer field separates and drives the electrons and ions in opposite directions onto the detectors. COLTRIMS can measure both ion and electron momentum. In our experimental COLTRIMS setup the gas jet and laser beam are perpendicular to each other, the electric and magnetic fields are parallel in the spectrometer, and we measured electrons and ions in coincidence.

The COLTRIMS apparatus provides us with [36, 93] 4π solid angle collection for ions and for low energy electrons, and allows ion and electron momentum measurement with a high resolution. COLTRIMS consists of the following main parts:

i) Vacuum chamber
ii) Gas jet
iii) Spectrometer
iv) Detectors
v) Magnetic coils
vi) Focusing mirror

These parts will be described next.

3.2.1 Vacuum chamber

The largest part of the COLTRIMS is a vacuum chamber, which contains five stages: the catcher, the main chamber (where the detectors are located), two intermediate chambers and a source chamber (Fig. 3.3). The last two are connected with a skimmer (0.5mm) and are evacuated using turbo-pump. The source chamber is usually kept at pressures in the 10^{-4} torr range, whereas the first and second intermediate chambers, which are separated by a 2mm diameter slit, are kept at 10^{-6} and 10^{-9} torr respectively. The intermediate chamber is connected to the main chamber (10^{-11} torr) with piezo-electric slit. The ion gauge is used to monitor all of our pressure. The catcher is used for removing the residual gas. (For details see [59])

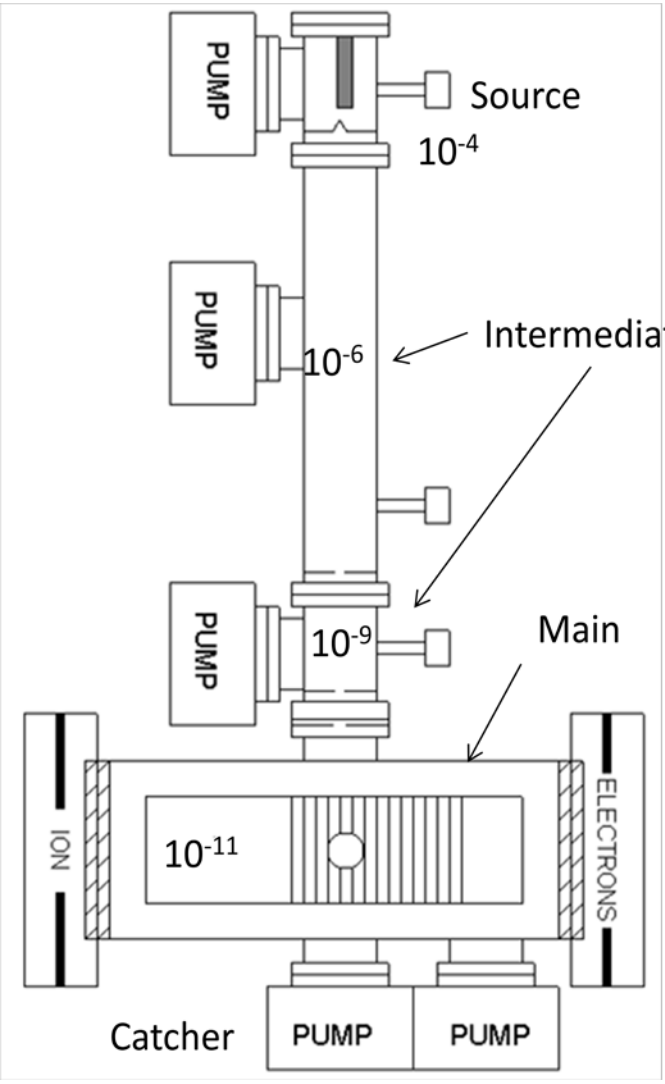

Fig. 3.3 Pumping stage of the COLTRIMS.
The source chamber is typically at 10^{-4} torr of pressure, the intermediate chambers are at 10^{-6} and 10^{-9} torr, the main chamber can reach the pressures around 10^{-11} torr. Laser beam direction is out of the plane of the paper.

3.2.2 Gas jet

The gas jet used in the COLTRIMS has to be cold in order for us to be able to measure recoil ion momentum because the typical value of the momentum is in the order of the molecular momentum spread at room temperature. The jet is made with a 30 μm nozzle followed by 0.5 mm skimmer, two 2 mm slits and a piezo-electric slit which adjustable from 40 μm to 2 mm wide. All this allows us to have an extremely thin jet, which has two advantages for high

intensity experiments. Firstly, target molecules are present mostly in the most intense part of the beam, and secondly, the small interaction volume contains on average less than a single target molecule.

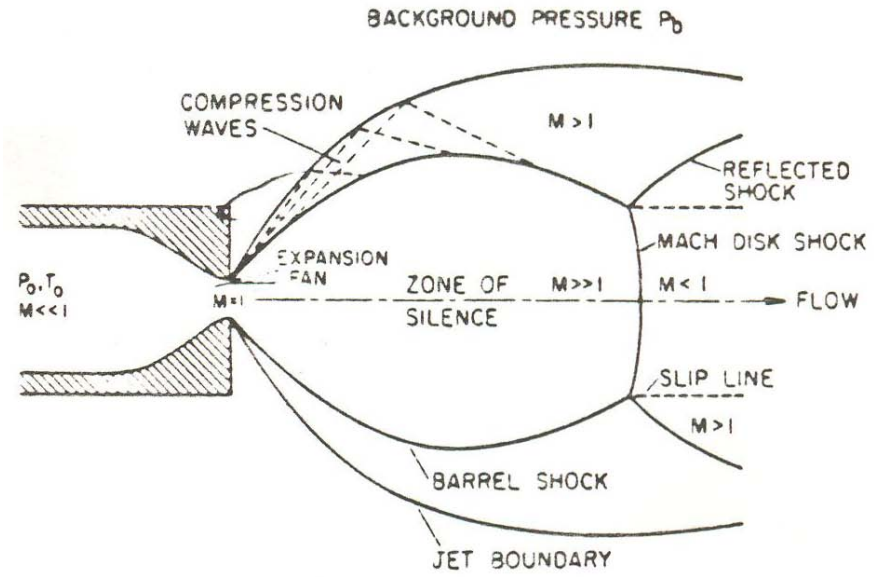

Fig. 3.4 Free-jet expansion. From [64].

Gas passing through the pin-hole forms the so-called: zone of silence (Fig. 3.4) [64]. In this region all gas molecules are moving at the same speed without interacting, which lowers the internal temperature of the gas in the zone of silence to only a few Kelvin. Its dimensions depend strongly on the ratio of gas supply pressure P_0 and the background pressure P_b of the expansion chamber. A skimmer, if it has appropriate position, can then cut out gas from the zone of silence, creating a very directional and a high velocity gas jet. At this juncture the length X_{zos} of the zone of silence is of particular interest:

$$X_{zos} = 0.67(P_0/P_b)^{1/2} \cdot d \tag{3.8}$$

where d is the diameter of the nozzle (slit). See appendix B for jet temperature and velocity.

3.2.3 Spectrometer

The spectrometer is usually made out of copper plates connected in a series with several resistors (Fig. 3.5). The voltage applied across spectrometer produces a uniform electric field.

The electric field separates positive and negative particles and sends them onto the detectors located at both ends of the spectrometer. Positively charged particles go to the ion side of the spectrometer, which is about 5 cm away from the interaction region, and the electrons go to the electron side separated by about 24 cm.

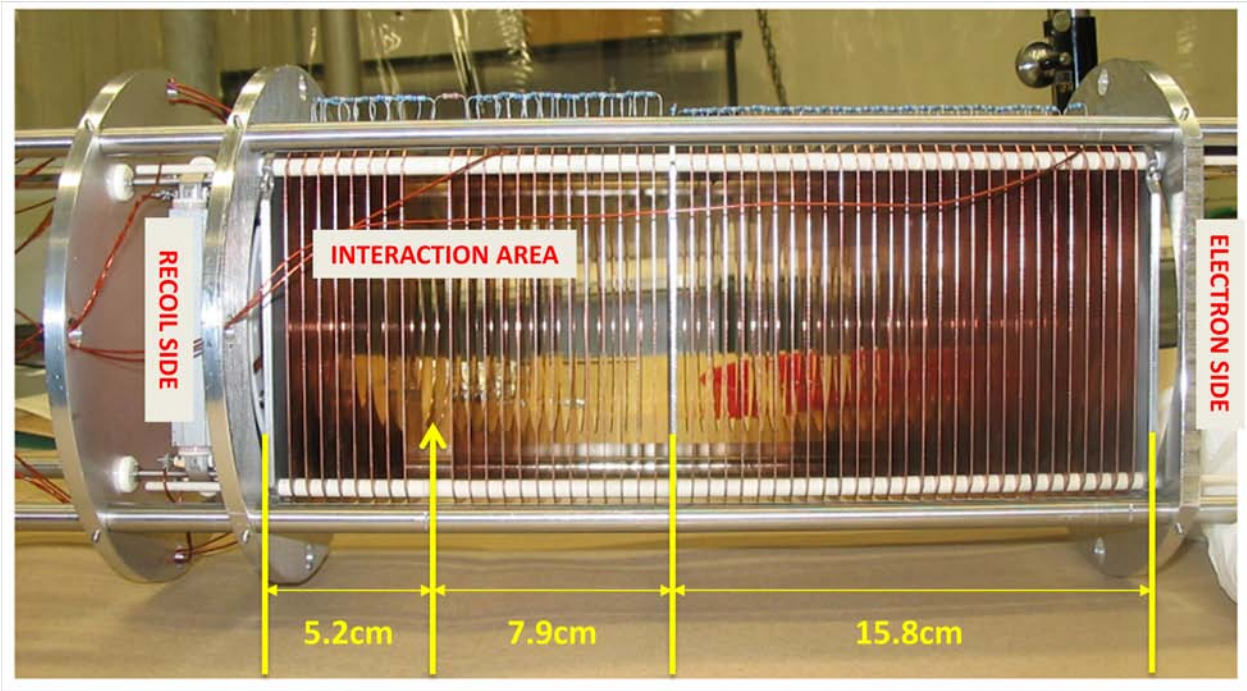

Fig. 3.5 Spectrometer.
(The photo was taken by former members of our group before assembling the COLTRIMS apparatus).

3.2.4 Detectors

Detection of the charged particles involves multi-channel-plates (MCP) (Fig. 3.6) and delay-line anodes (DLA) (Fig. 3.7) [78]. For the ion and electron side of the COLTRIMS detector two MCP (8cm in diameter) plates are used, aligned in a V shape (also known as a Chevron configuration). When a charged particle hits the front of the MCP it produces electrons which further multiply in the channels (Fig. 3.6). The main purpose of using a MCP is to amplify the charge of the detected particle so that a signal can be measured. The channels in the MCP are inclined around 8^{o} to the normal direction to guarantee that an incoming particle hits the wall of the channel for amplification.

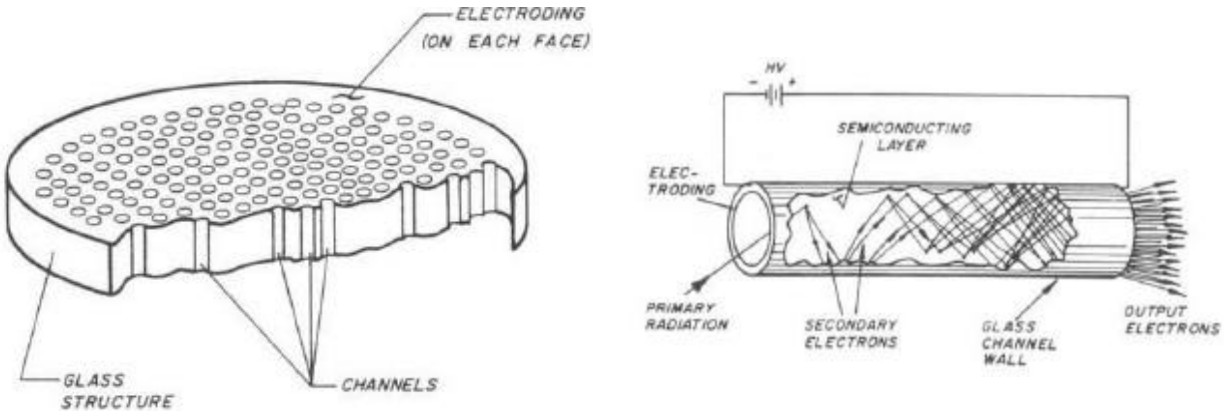

Fig. 3.6 Working principle of an MCP, electrons are multiplied in several million independent channels
(from J. L. Wiza, Reprinted from Nuclear Instruments and Methods, Vol. 162, (1979), pages 587 to 601).

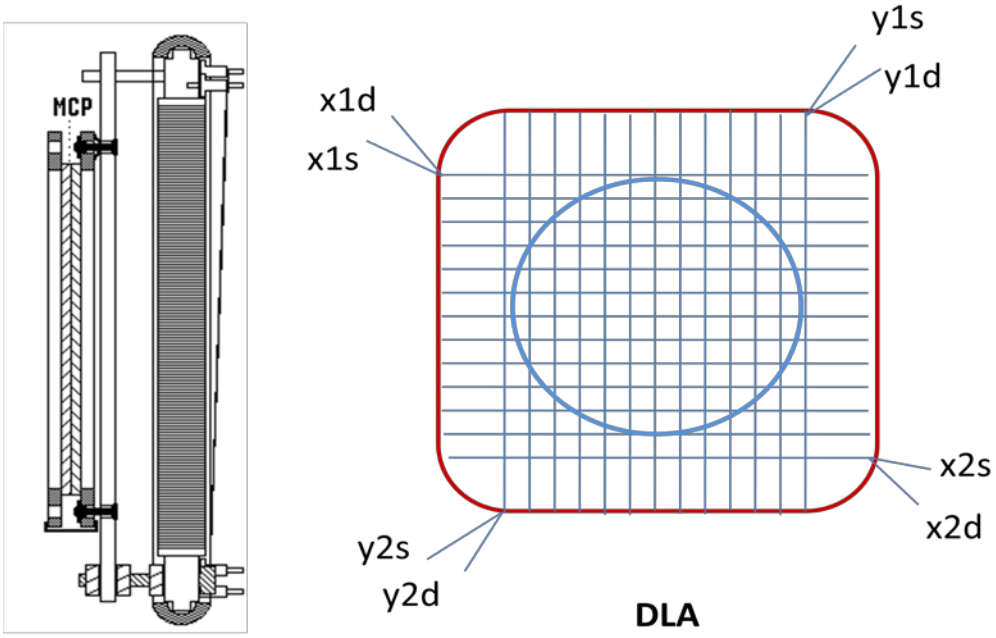

Fig. 3.7 Drawing of DLA- position and time sensitive detector with micro channel plates [78], and illustration of a pair of wires is wrapped around the ceramic squares.

We get our position signals from the DLA and we get the timing signal from the MCP. In the DLA a pair of wires (signal and reference) is wrapped around the ceramic squares in two perpendicular directions (x and y). There is a potential difference (around 50V) between the two wires, the one which is at lower voltage is called the “difference” and the one at the higher voltage is called the “signal” wire. The voltage difference causes an electron, once it hits the DLA to travel though the wires in the 4 directions (x1, x2, and y1, y2). These signals are then

sent to the difference amplifier where the noise gets subtracted from the total signal (x1s-xd1=x1…) and the real signal gets amplified. The position of the signal is determined by the difference in the time travelled through the wires. The pulses travel through the wires at the speed of light. The signals traveling velocity (calibration constant for DLA) is measured and known for each detector.

One can get the position of the signal using the expressions

$$x = g(x1 - x2) \text{ and } y = g(y1 - y2) \tag{3.9}$$

where g is the calibration constant (conversion factor for changing the timing signal into a position signal) and has a value near one mm/ns. The exact value for the detectors we used in the COLTRIMS setup is g=0.9 mm/ns.

3.2.5 Magnetic coils

For guiding charged particles to the detectors we used a combination of both electric and magnetic fields. For that purpose, our COLTRIMS used six coaxial magnetic coils separated from the center of the spectrometer as shown on Fig3.8. The large coils are used to create a homogeneous magnetic field across the spectrometer, and the other two pairs are used to correct it. The magnetic field can be calculated at any point x along the axis of the coil by using the formula

$$B = \frac{\mu_0 N I r^2}{2}\left((r^2 + (d + x)^2)^{-3/2} + (r^2 + (d - x)^2)^{-3/2}\right) \tag{3.10}$$

where N, I, r, and d are correspond to the number of turns, the current through the coil, the radius of the coil and the separation between the two coils (the starting point in our case is the center of the spectrometer, $\mu_o = 4\pi \times 10^{-7}$ Tm/A is the permeability constant).

We also used additional coils to cancel out the Earth's magnetic field. For that purpose, four Ribbon cables (95 inches long and 20 wires wide) were wrapped around the plastic frame as shown in Fig. 3.9. All of the wires are collinear with the two (horizontal and vertical) perpendicular lines to the spectrometer axis. In our experiments we were applying 1.6 A and 3 A to the coils which corresponded to total magnetic field of 6.1 Gauss and 12.8 Gauss respectively.

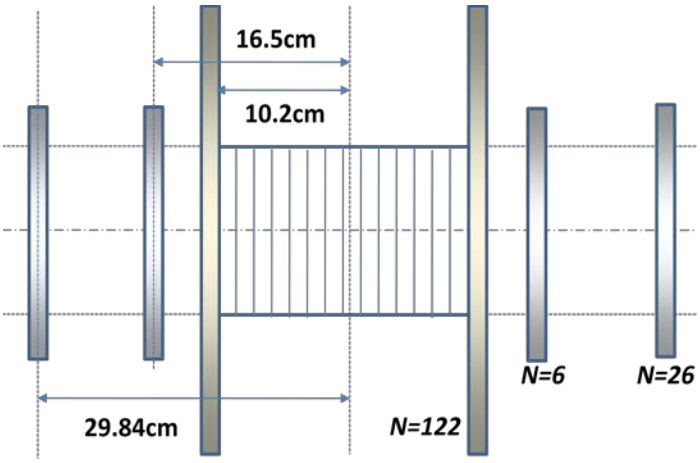

Fig. 3.8 Magnetic coils of the COLTRIMS apparatus.
The radius of the small four coils is 10.16cm and the radius of the two bigger coils is 33.0 cm. The number of the copper wire turns is 122 on large coils, 6 on the small two coils located near large ones, and 26 on the coils located furthest from the center of the spectrometer.

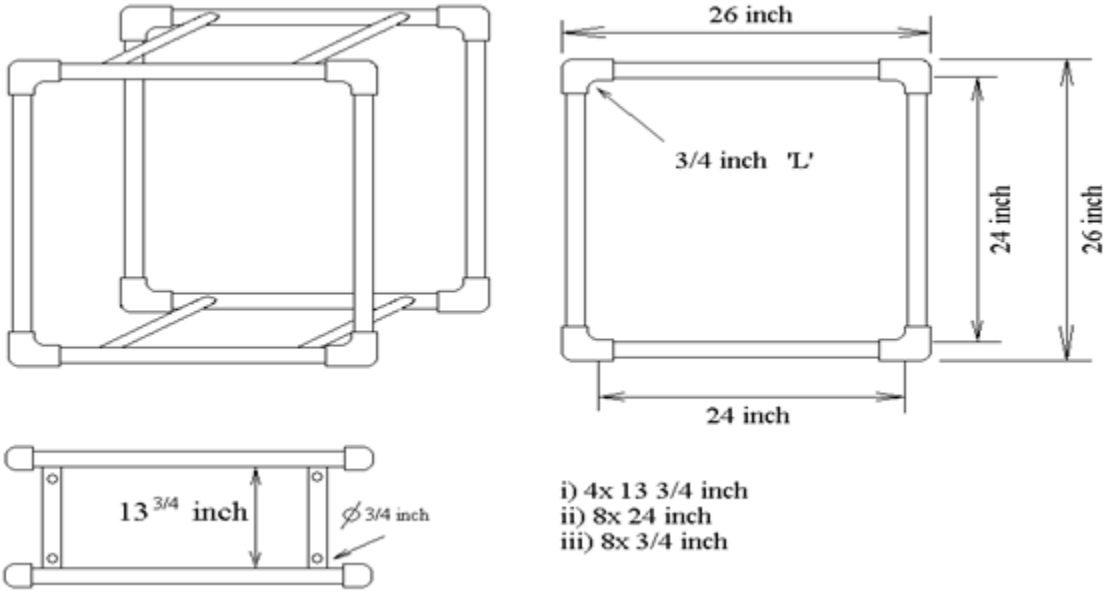

Fig. 3.9 Setup for the magnetic coil frame used to cancel the Earth's magnetic field. (top view).

3.3 Theory and Operation of Optical Parametric Amplifier

An Optical Parametric Amplifier (OPA) is a laser light source that emits light of variable wavelengths by an optical parametric amplification process [15, 17, 34]. It converts a laser pulse of one fundamental wavelength to short pulses of high intensity with a continuously tunable

wavelength. In the general case, an ultra short pulse of high intensity propagates in a nonlinear crystal to provide gain for a weak pulse at the signal wavelength. The infrared part of the spectrum is commonly used for investigating molecular structures [4-8, 11, 56, 76, 88]. Short infrared pulses are used in the detection of molecular bond breaking and forming [16, 65, 66]. Therefore, it is very important to develop techniques of producing femtosecond pulses tunable in the infrared and near-infrared region of the spectrum. Most of these techniques are based on parametric difference-frequency processes. Parametric processes are photon interactions in which one high frequency photon is annihilated and two low frequency photons are created. This section will describe the theory behind an OPA and how an OPA is designed and operated.

3.3.1 Parametric Amplification

Crystal materials lacking inversion symmetry can exhibit so-called $\chi^{(2)}$ nonlinearity [15]. Apart from frequency doubling and sum and difference frequency generation, this allows for parametric amplification. Parametric processes are photon interactions in which one high frequency photon is annihilated and two lower frequency photons are created (parametric down conversion).

Parametric amplification is a phenomenon where a signal can be amplified using a parametric nonlinearity and a pump wave. Here, the signal beam propagates through the crystal together with a pump beam of shorter wavelength. Photons of the pump wave are then converted into (lower-energy) signal photons and the same number of so-called idler photons; the photon energy of the idler wave is the difference between the photon energies of pumps and signal wave. As the pump energy is fully converted into the energy of signal and idler beams, the crystal material is not heated in this process.

When there is a phase mismatch, the relative phases of the waves will change during propagation, so that after some distance the power in signal and idler can be converted back toward the pump. Therefore, phase matching, which can be achieved only in a limited frequency range, is important for efficient amplification. Under certain special conditions, a very large phase-matching bandwidth may be achieved. A very beneficial property of optical parametric amplifiers is that fundamentally there is no dissipative process in the nonlinear crystal. The absence of heat generation makes OPA quite suitable for high power operation.

3.3.2 Theory

When the laser field interacts with media, the system changes its optical properties and can give nonlinear response [17]. The dependence of the characteristic polarization of the system on the applied field can be expressed as

$$\vec{p}(t) = \chi^{(1)}\vec{E}(t) + \chi^{(2)}(t)\vec{E}^2(t) + \ldots \tag{3.11}$$

where $\chi^{(1)}$ and $\chi^{(2)}$ are the first and second order nonlinear susceptibilities.

The reason why polarization plays such a key role in the description of nonlinear optical phenomena is that a time-varying polarization can act as the source of new components of the electromagnetic fields.

The wave equation in nonlinear optical media has the form

$$\nabla^2\tilde{E} - \frac{n^2}{c^2}\frac{\partial^2\tilde{E}}{\partial t^2} = \mu_0\frac{\partial^2\tilde{P}^{NL}}{\partial t^2} \tag{3.12}$$

where n is the usual linear refractive index, c is the speed of light in vacuum, and P^{NL} is the nonlinear part of the polarization. If the incident field consists of two frequency components,

$$\tilde{E}(t) = E_1 e^{-i\omega_1 t} + E_2 e^{-i\omega_2 t} + c.c., \tag{3.13}$$

the non-linear polarization will be given by the expression

$$\begin{aligned}\tilde{P}^{(2)}(t) = \varepsilon_0\chi^{(2)}[E_1^2 e^{-i\omega_1 t} + E_2^2 e^{-i\omega_2 t} + 2E_1E_2e^{-i(\omega_1+\omega_2)t} \\ + 2E_1E_2^* e^{-i(\omega_1-\omega_2)t} + c.c.] + 2\varepsilon_0\chi^{(2)}[E_1E_1^* + E_2E_2^*].\end{aligned} \tag{3.14}$$

The polarization contains different terms with different frequencies. One of the terms is $2\varepsilon_0\chi^{(2)}E_1E_2^*e^{-(\omega_1-\omega_2)t}$ with an amplitude of $P = 4\varepsilon_0 d_{eff}E_1E_2^*$ (for fixed field propagation and polarization directions), where $d_{eff} = 0.5\chi^{(2)}$ is the effective nonlinear coefficient of the media. It describes the process of difference frequency generation. The frequency of the generated wave is the difference of the applied fields. In terms of photons this means that for every photon created at a frequency of $\omega_3 = \omega_1-\omega_2$, the input photon at a frequency of ω_1 is destroyed and another photon ω_2 is created ($\omega_1 > \omega_2 < \omega_3$).

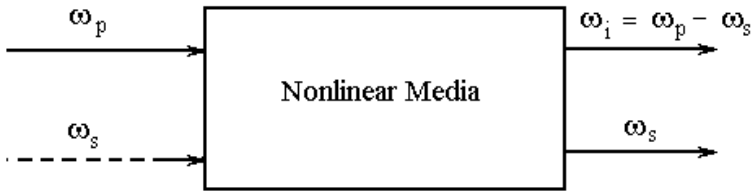

Fig. 3.10 Difference frequency generation (See text).

Consider the situation shown in Fig. 3.10, where optical waves at frequencies ω_p and ω_s interact in a lossless nonlinear optical medium to produce an output wave at a difference frequency of $\omega_i=\omega_p-\omega_s$. Now assume that ω_p is the frequency of the strong wave which we are going to call the "pump wave", and the wave with a frequency of ω_s is the "signal wave". Both waves are incident on the nonlinear lossless media. Then an idler wave with a frequency of $\omega_i=\omega_p-\omega_s$ ($\omega_p>\omega_i>\omega_s$) is generated.

If we represent the amplitude of the electric field as $E = Ae^{ikz}$, the nonlinear response of the media to the signal wave is

$$P_S = 4\varepsilon_0 d_{eff} A_p A_i e^{i(k_p+k_i)z} \tag{3.15}$$

and has the same form for the idler wave. Substituting these equations into the wave equation (3.12) and assuming lossless media and slowly varying amplitudes along the z direction, we come up with equations for amplitudes for the idler and signal waves

$$\frac{dA_i}{dz} = i\frac{2\omega_i}{n_i c} d_{eff} A_p A_S^* e^{i\Delta kz}, \qquad \frac{dA_S}{dz} = i\frac{2\omega_S}{n_S c} d_{eff} A_p A_i^* e^{i\Delta kz} \tag{3.16}$$

where $\Delta k = k_p - k_s - k_i$ is the phase mismatch.

3.3.3 Phase matching

Phase matching is an important factor in optical parametric amplification because the energy exchange between the pump and the signal waves depends on how perfectly they match. The intensity of a generated field depends on the wave vector mismatch $\Delta k=k_p-k_s-k_i$ as [15, 17]

$$I \sim \sin c^2\left(\frac{\Delta kL}{2}\right) \quad . \tag{3.17}$$

This means that the intensity of the signal decreases dramatically as Δk increases. The difficulty with setting $\Delta k=0$ arises because of the normal dispersion in media, i.e. due to the frequency dependent index of refraction.

For the case $\Delta k=0$ we can write

$$n_p\omega_p = n_s\omega_s + n_i\omega_i, \qquad \omega_p = \omega_s + \omega_i, \qquad \omega_p > \omega_i > \omega_s \tag{3.18}$$

Such that

$$n_p = \frac{n_s\omega_s + n_i\omega_i}{\omega_p} \tag{3.19}$$

$$n_p - n_i = (n_s - n_i)\frac{\omega_s}{\omega_p}. \tag{3.20}$$

A solution cannot be found for this system of equations because for a normal dispersion, $n_p>n_i$, $n_i>n_s$. Therefore the left-hand side of (3.20) is positive, but the right-hand side is negative. At this point we can make use of crystals which are birefringent. That means that the refractive index depends on the direction of the wave polarization. If the ω_p-wave is polarized in the direction corresponding to the lowest refraction index - say, extraordinary for an uniaxial crystal – then there are two possibilities for the signal and idler waves to have the same polarization (type I phase matching) or to be orthogonal (type II phase matching).

Angle tuning is one of the methods used to achieve phase matching. The nonlinear (uniaxial) crystal is rotated in such a manner that its optical axis makes an angle θ with the vector **k** of the pump wave. This wave can be polarized perpendicularly to the plane containing **k** and the optical axis or in the same plane. In the first case the refractive index would be ordinary (n_o), but in the second case it would be extraordinary (n_e), which depends on the angle θ. For $\theta=90^0$, n_e equals to some principle value, at $=0^0$ it equals to n_o. Precisely adjusting the angle between an optical axis and the wave vector of the incoming wave we can achieve such a value for n_e (θ) that the phases are matched. But even when phase matching is achieved there are still some walk-off effects which cause waves to drift from each other in space and time. It causes a decrease in effectiveness of the energy exchange between interacting waves.

3.3.4 TOPAS (Traveling-wave Optical Parametric Amplifier of Super Fluorescence)

TOPAS is a model of an optical parametric amplifier which is used in the James R. Macdonald Laboratory. The general principles of a TOPAS design are described below [47]. A calibration chart for TOPAS is given in Appendix C.

TOPAS employs one stage for the generation of super fluorescence and four light amplification stages arranged in a single BBO crystal. Wavelength tuning is performed by rotating the nonlinear crystal which is operated in a type II phase matching configuration. For type II phase matching, the polarization of the signal and idler waves are orthogonal. Therefore the signal and idler waves can be separated using a polarizer. TOPAS can be pumped with different kinds of lasers with a wavelength in the range from UV to near infrared [47]. The working principle of TOPAS can be broken down in to a three-step process:

1) Generate a broadband seed (seed = signal + idler) from a small portion of the pump.

2) Narrow the seed's spectrum and pre-amplify with a small portion of the pump.

3) Amplify the seed with most of the pump.

The incoming pump beam is split in three components upon entering the device. One of the components, which is just 15% of the total intensity, is used for generating of the seed. This component will complete three passes in the nonlinear crystal (NC). Figs. 3.11(a)-3.11(b)

The first pass is needed to produce the super fluorescence (SFL) in the NC and the second pass amplifies the collinear components of the SFL. TOPAS pumped by ~800 nm light generates IR wavelengths (1.1-1.6 μm for the signal and 1.6-2.6 μm for the idler). After the third pass, which amplifies the second one, the beam hits the center of the diffraction grating. The diffraction grating is used to reduce the spectral width of the seed (signal), to separate signal, idler and pump in space, and to make the wavelength tuning more precise in the wavelength range close to NC absorption band. The procedure for tuning the NC in TOPAS is arranged in such a way that the diffraction grating and the crystal are rotated together. The fourth pass in TOPAS is employed for the formation of a stable; nearly transform limited, and a low diffraction seed for the power amplifier (Figs. 3.12(a)-3.12(b)).

As a result of the three first passes we have a weak broad banded radiation pattern with a significant divergence in the vertical plane. With another small portion of the pump, the signal is amplified in the NC and shaped as if there was a small amplifying aperture in the far field of the seeder. This happens because when the pump and signal overlap in the NC, only a small part of the signal is amplified since the pump beam waist is small. The fifth pass is the final amplification. By this moment we have seed radiation which is coherent in space and time but weak, and it is amplified in the fifth pass with approximately 70% of the pump beam. This component of the pump beam and the seed are matched in size where they overlap in the NC for effective energy conversion. On the fifth pass the signal is amplified from several micro joules to the specified energy, depending on the energy of the pump. (Fig. 3.13(a) - 3.13(b))

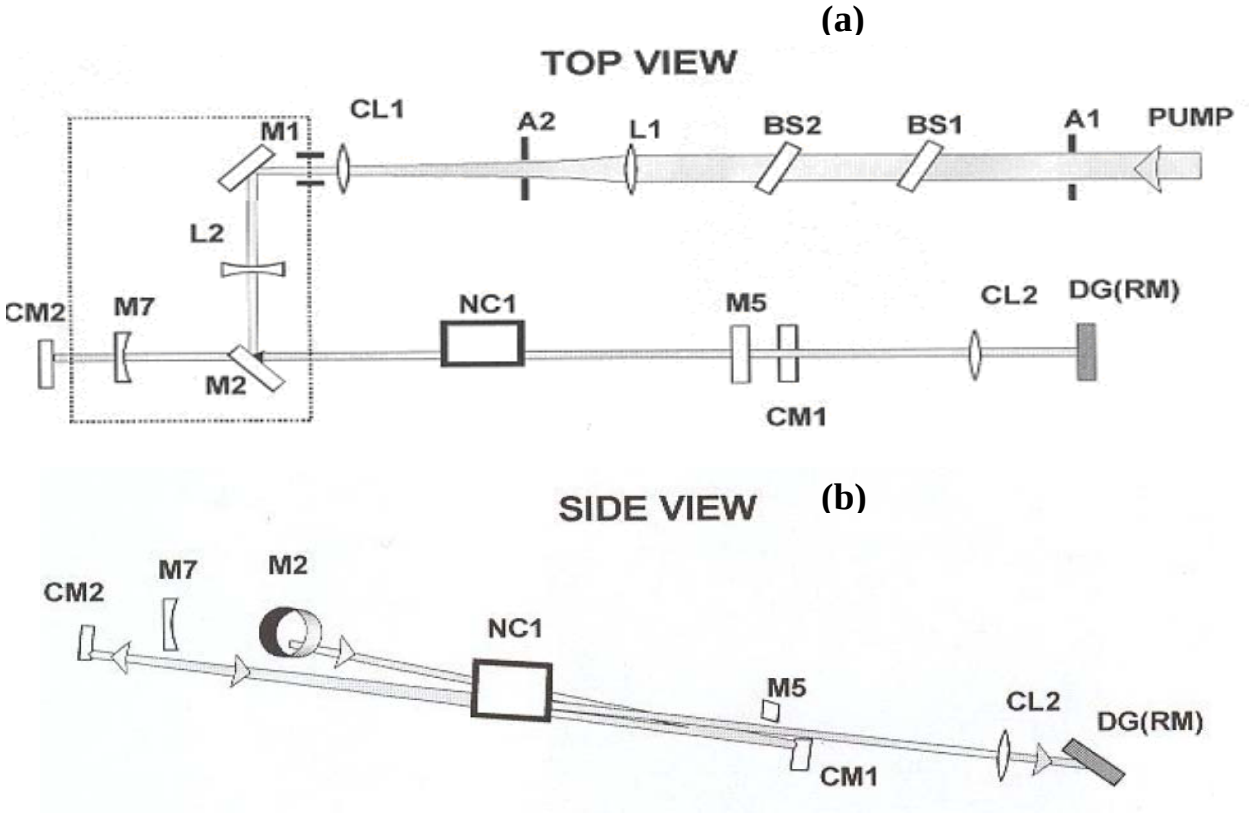

Fig. 3.11 Top view (a) and side view (b) of first, second, and third passes of beam in TOPAS (From [47]).

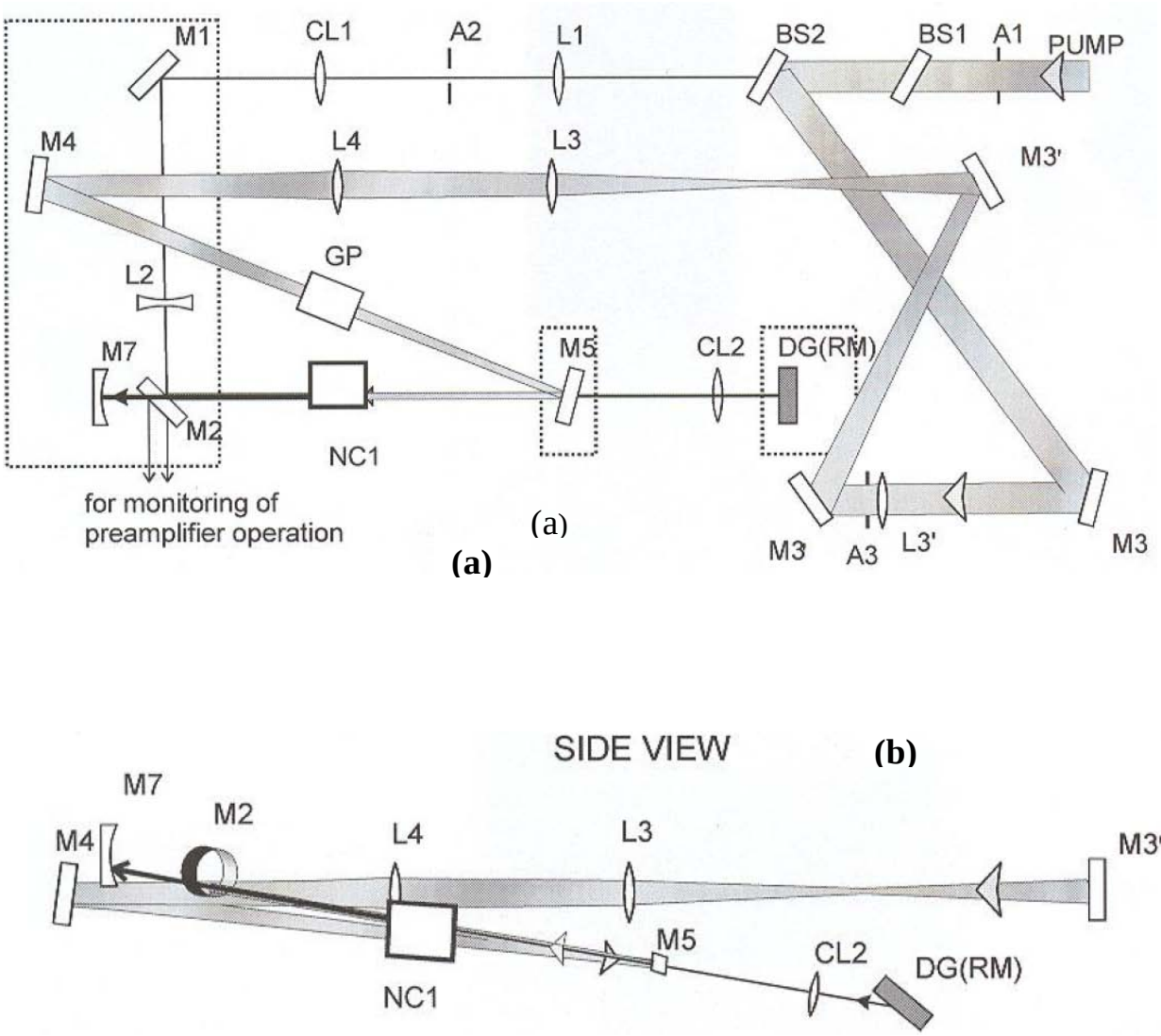

Fig. 3.12. Top view (a) and side view (b) of the fourth pass (pre-amplification of the seed beam) of the beam in TOPAS.
(From [47]).

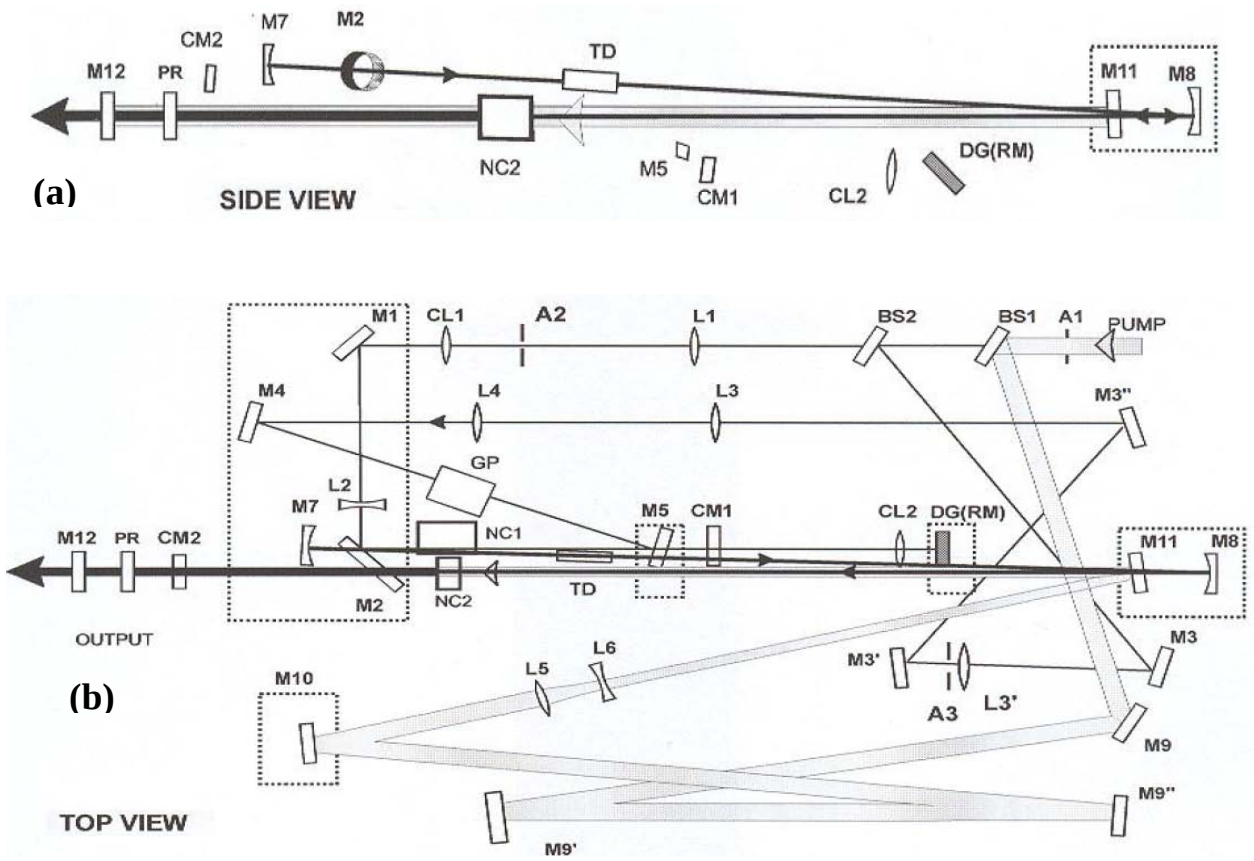

Fig. 3.13 Side view (3.13.1) and top view (3.13.2) of the fifth pass of the beam in TOPAS (final amplification, from [47]).

CHAPTER 4 - Data processing

In this chapter the data recording, processing and calibration of the experimental parameters will be discussed.

4.1. Data Acquisition

As mentioned in the previous chapter, COLTRIMS detectors contain MCPs and delay lines for obtaining time and position signals. For extracting the right signal from the DL it is important to introduce the parameter, which is called time sum. The sum of the time signals that travel through the two ends of the copper wires in the DL after the charged particle hits it, is a constant independent on the hit position

$$t1+t2=\text{constant} \tag{4.1}$$

where t1 (x1d, x1s, y1d, y1s) (See Fig. 3.7) and t2 (x2d, x2s, y2d, y2s) (See Fig. 3.7) correspond to the time travelled through one wire. The time signal is measured relative to the event registered on the MCP such that

$$t1+t2 - 2t_{mcp}= \text{time sum.} \tag{4.2}$$

In reality, there are two parallel wires wrapped around the ceramic frame of the DL (Fig. 3.7) such that we have two time sums:

$$\text{Time sum } x=x1+x2-2t_{mcp} \tag{4.3}$$

$$\text{Time sum } y=y1+y2-2t_{mcp} \ , \tag{4.4}$$

where x1, x2 and y1,y2 are time signals that travelled through perpendicular wires. Having the time sums is essential for assigning the values for position coordinates on the detector to the corresponding time of flight properly.

The schematic diagram of the data acquisition is shown on Fig. 4.1. The photodiode signal is used to initialize the system (start time), the signal is positive but our constant fraction discriminator (CFD) will only accept a negative signal input, so we have to invert the photodiode signal to negative using the inverter. After inverting the signal from the photodiode using the Ortec inverting transformer 100 (IT-100) and the amplifier, it is sent to the CFD Ortec 934 where

the signal gets accurate timing and digitalization. The CFD takes three different signals from the MCP recoil, the MCP electrons, and the photodiode. The three outputs from the photodiode signal are then sent to the time-to-digital convertor (TDC). The position signals from delay line are amplified by the delay line amplifier DLA 800 and are fed to the input channels of the TDC (8 position signals+ 2 timing signals). The TDC we used is a LeCroy 3377 multi-hit time-to-digital converter with 32 channels, capable of registering 16 hits per channel. It has 10 ns dead time after each hit so if the detector is hit by two particles (ion or electron) during this time, only one will be detected. From the TDS the digitalized signals are passed to a computer and analyzed using Lab-View program data.

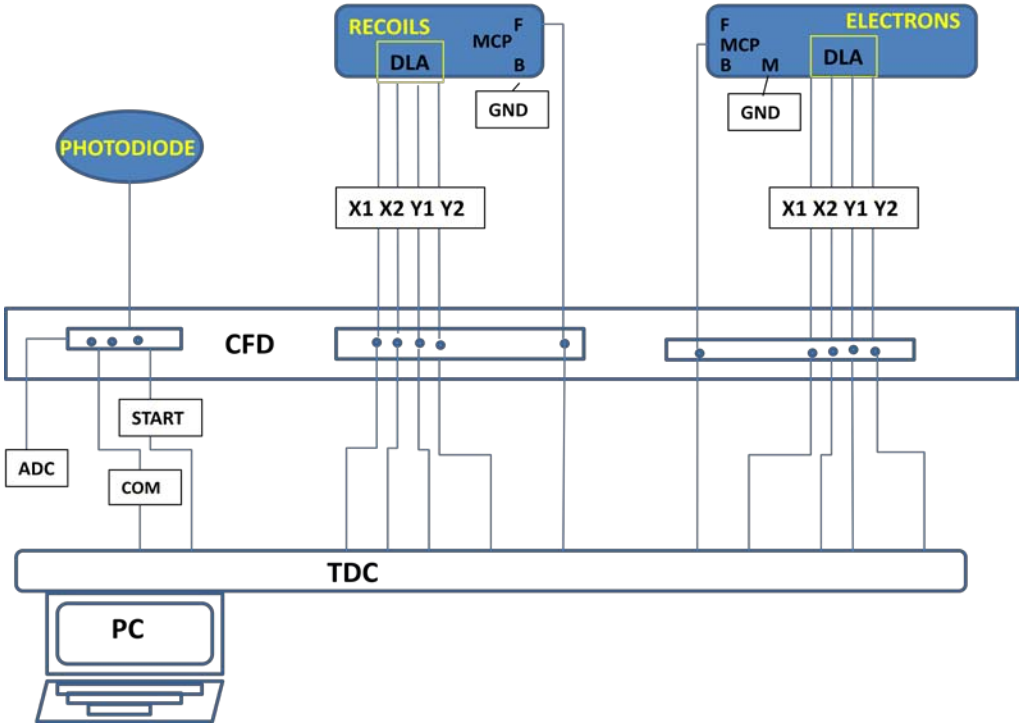

Fig. 4.1 Schematics of the data processing.

The FORTRAN code (appendix D) [59] is used to translate the timing and position information of our raw data into physical quantities like momentum and energy. Before using the code, a calibration of all experimental parameters needs to be performed. The calibration parameters can be found in the code itself. The parameters are the absolute time zero, the position zero, and the cyclotron period. The parameters related to the geometry of the setup such as time-of-flight distance, spectrometer length, and gap between the spectrometer grid and detector, are known.

4.2. Calibration

For relating the raw data to the real physical values, it is very important to have the correct value for time zero. An offset needs to be added to the time of flight to have a real time. In order to determine the time zero for the case when only ions are detected, the time-of-flight spectra are plotted. The peak values vs. square root of the ratio of mass over charge of the corresponding ion are plotted and fitted with a line. The intercept of the line with the time-of-flight axis gives us the value of the time zero.

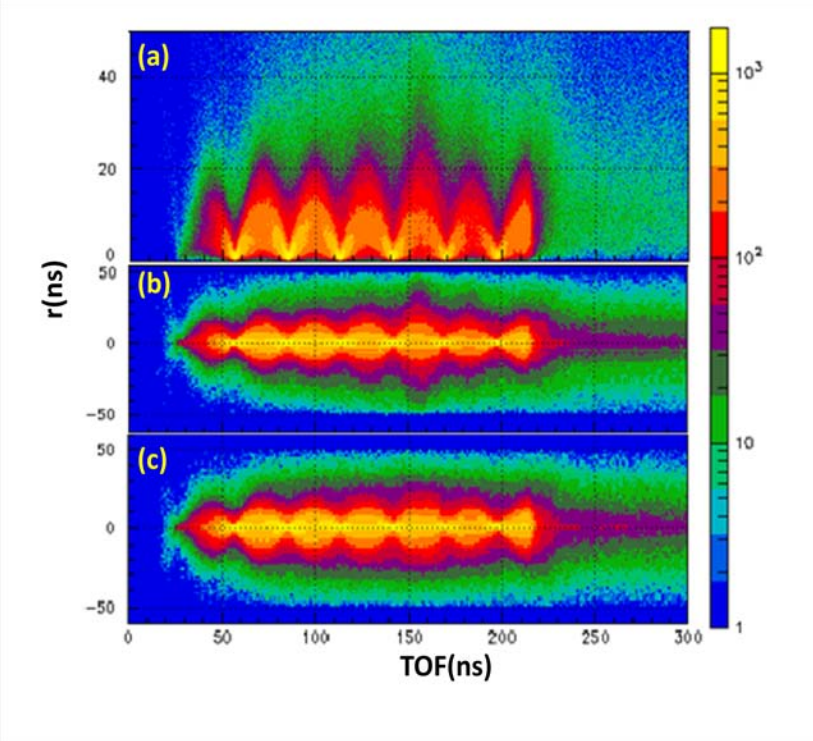

Fig. 4.2 (a) Nodes of the wiggle spectrum, 2D plot of the distance from the center of the detector to the electron hit position versus time of flight (TOF) of the electrons, (b) so called "x-fish" which is a plot of the electron hit position x coordinate versus TOF of electrons, (c) so called "y-fish" is the same as X-fish but TOF versus y coordinate of the hit position.

In our experiments we detect ions and electrons in coincidence, such that we can produce a very broad electron time-of-flight that will give several positions of nodes as a result of the cyclotron motion in the magnetic field as shown in Fig. 4.2. This so-called 'wiggle' spectrum is a plot of the distance from the center of the detector to the point where an electron hits the detector vs. time of flight. The nodes corresponding to the positions of the electron at the center of the

detector are spaced equally from each other and the time distance between them corresponds to the cyclotron period (T_c).

With a changing magnetic field the position of the nodes shifts. The node position is independent of the initial energy of the electrons and the electric field across the spectrometer. Depending on the magnetic field, the period of the cyclotron motion of the electron and corresponding time between the node positions are

$$T_c = \frac{2\pi m}{eB} \tag{4.5}$$

where T_c is the cyclotron period and is equal to the distance between any two consecutive node positions. B is the magnetic field, e is the electron charge, and m is the electron mass. The cyclotron frequency is

$$\omega_c = \frac{2\pi}{T_c} \tag{4.6}$$

Assuming that the electric and magnetic fields are parallel and in the z direction (Fig. 4.3), the distance travelled by the electron in the z direction can be written from classical mechanics as

$$Z = v_{\parallel} t + \frac{a t^2}{2} = v_{\parallel} t + \frac{e\mathcal{E} t^2}{2m} \tag{4.7}$$

$$\Rightarrow\ v_{\parallel} = \frac{Z}{t} - \frac{e\mathcal{E}}{2m} t \tag{4.8}$$

where a is the acceleration, $\mathcal{E}$ is the electric field, and m is the electron mass. The cyclotron radius can be written as $R = v_{\perp}/\omega_c$ where the cyclotron frequency is given by (4.6), $v_{\perp} = (v^2 - v_{\parallel}^2)^{1/2}$, and $v = (2E/m)^{1/2}$, E is the total energy.

The distance the electron hits from the center of the detector can be written as

$$r = 2R \left| \sin \frac{\omega_c t}{2} \right| \tag{4.9}$$

$$r = \frac{2}{\omega_c} \sqrt{v^2 - v_{\parallel}^2} \left| \sin \frac{\omega_c t}{2} \right| = \frac{2}{\omega_c} \sqrt{\frac{2E}{m} - \left(\frac{Z}{t} - \frac{e\mathcal{E}}{2m} t \right)^2} \left| \sin \frac{\omega_c t}{2} \right| \tag{4.10}$$

This expression is plotted for specific parameters in Fig. 4.4. One can fit the experimental wiggles with the wiggles given by expression (4.10) and find all the necessary parameters such as the cyclotron period (or frequency), absolute time-zero, and the electric field of the spectrometer.

Calibration of the intensity by can be done either using equation (3.7) or the momentum plots of the singly charged ions in circularly polarized light. The first method requires measuring the pulse duration and the focal radius of the beam. In the second method one can deduce the peak intensity from the measured drift momentum gained by an electron due to ionization by circularly polarized light. The value of the drift momentum an electron can gain in the circularly polarized field is directly proportional to the strength of the electric field, which is related to the peak intensity. Compared to the drift momentum gained by an electron in a linear pulse, the drift momentum gained by an electron in a circularly polarized pulse is independent of the phase at which the electron was born [30].

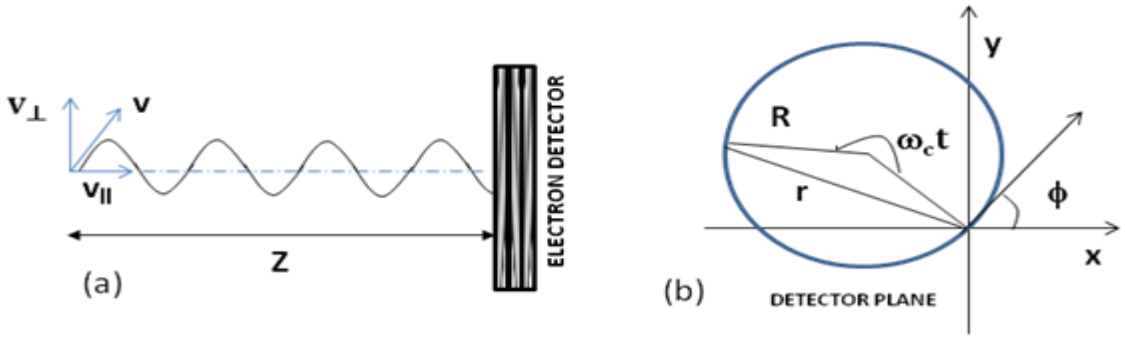

Fig. 4.3 (a) the schematics of the electron motion in the combined magnetic and electric fields which are parallel to each other and are perpendicular to the detector. (b) Electron trajectory projection in the perpendicular direction to the magnetic field.

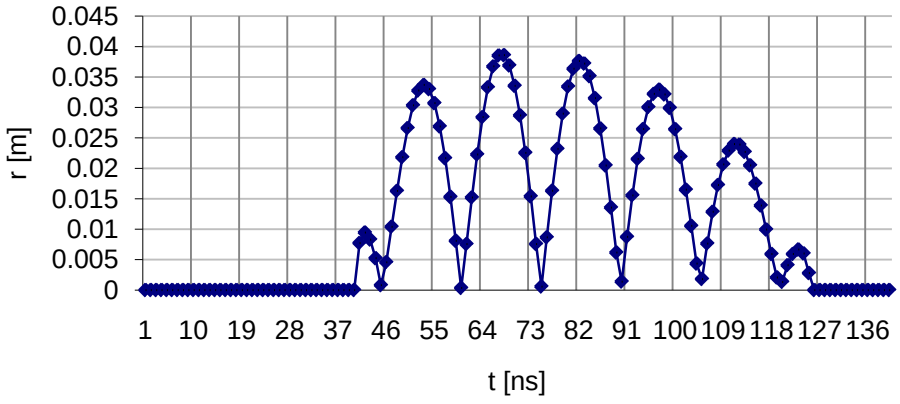

Fig. 4.4 Wiggle spectrum plotted from equation (4.10) for the magnetic field of 12 G, a voltage across the spectrometer of 33 V (1.38 V/cm), and 12 eV initial energy.

From Fig. 4.5 one can approximately find the drift momentum (by taking the distance between the peaks which is in atomic units) by using the following formula to calculate the peak intensity:

$$I = 2 * \left(\frac{\Delta p_z}{2}\omega\right)^2 \tag{4.11}$$

For a peak difference of 1.6 a.u. and 1.8 a.u. (Fig. 4.5) one can get (for ω=0.057a.u.) $5.8\text{x}10^{14}$ W/cm^2 and $7.4\text{x}10^{14}$ W/cm^2 correspondingly after converting from atomic units to W/cm^2.

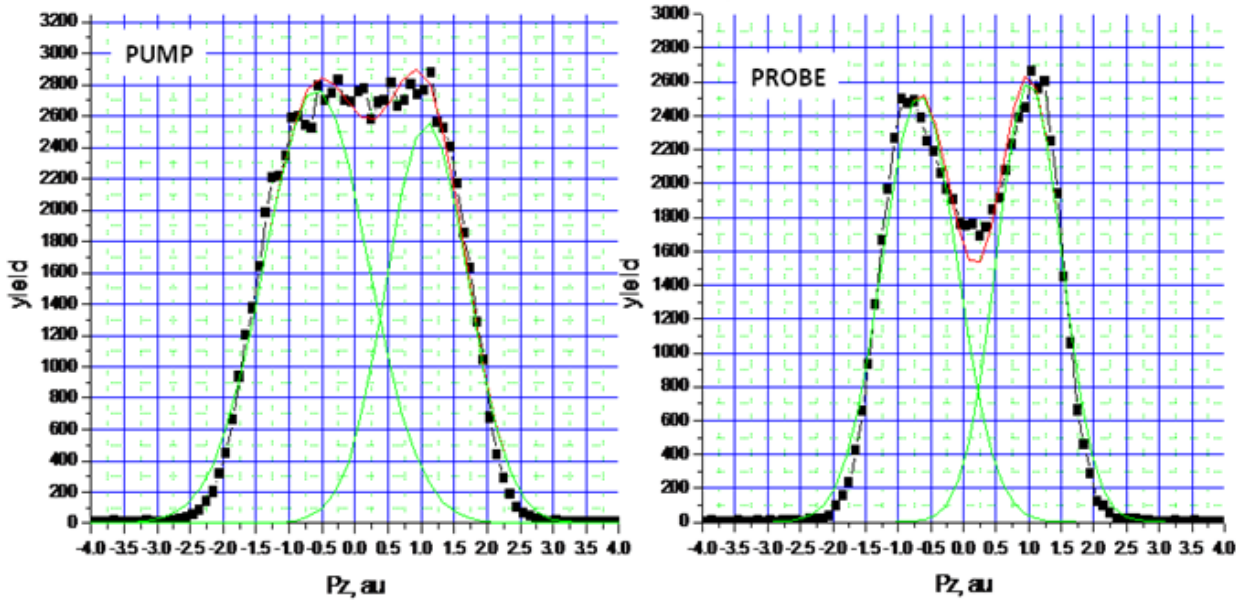

Fig. 4.5 Projection of the momentum of Ar^+ on the polarization plane for circularly polarized pump and probe pulses.

It is important to note that this method for determining the peak intensity is only valid in the case when the ionization rate changes rapidly before reaching the peak intensity. A more accurate way to determine the peak intensity is given in [5] where the experimental curve is fitted with the theoretical ionization rate as a function of the drift momentum at peak intensity for different temporal profiles. The obtained laser intensity is found to be independent of the temporal profile which proves that the calibration method used in this paper is correct.

CHAPTER 5 - Angular dependence of D_2 ionization

5.1 Introduction

The fact that strong-field ionization of the molecules strongly depends on the angle between the molecular axes and laser polarization direction is now well recognized. Knowing the angle-differential multi-photon ionization cross-sections (probabilities) allows us to understand most of the strong field phenomena quantitatively, such as high harmonic generation [22, 62], non-sequential ionization [41, 94], and above-threshold ionization [73]. Therefore, it is not surprising that understanding molecular ionization has become very important in strong field ionization studies. To interpret all these physical phenomena it is very important to know the angular dependence of molecular ionization.

The angular dependence can be determined by the character of the molecule's highest occupied molecular orbital (HOMO) [4]. Electrons which are ionized from the valence orbits of the neutral molecule contain more information about molecular orbital structure than what we can get from the molecular ions. The molecular orbital information can be obtained from the angular distribution of electrons ionized from aligned molecules [8].

The angular dependence of the field ionization can be measured experimentally either by using transient alignment generated by a weaker pump pulse [56], or by measuring the momentum of the molecular fragments and determining the angle between the field polarization and the molecular axis [4, 56, 74, 8]. In both cases the ionizing pulse should not disturb the initial distribution of the molecular axes. The measurements were usually performed on large linear molecules such as N_2, O_2, CO, CO_2, C_2H_2 [7, 56, 75]. Lighter molecules such as H_2 and D_2 pose a bigger challenge because it is much harder to control their dynamical alignment due to their low rotational inertia and low polarizability anisotropy. When placed in the intense laser field, H_2 and D_2 rotate very fast and change orientation significantly even during a short few cycle pulse. The reason is that they are very light. Despite these difficulties the angle-dependent ionization yield of pre-aligned D_2 molecules using 8 fs 800 nm laser pulses was estimated [16].

At the same time, Staudte and co-workers [88] came up with a method which does not require molecular alignment for measuring the angular dependence of the ionization. The method

is based on the fact that the same pulse dissociates a significant fraction of the ionized molecules via BS $H_2^+ \rightarrow H^+ + H^0$. The direction of the molecular axis before dissociation is determined by measuring the 3D momentum of the resulting protons. However it is not suitable for determining the angular dependence of ionization for linearly polarized pulses because BS itself is very anisotropic and molecules were found to rotate by up to 90° between ionization and dissociation events [74].

5.2. Molecular alignment

The laser interaction with the molecule can be described by considering the coupling of the laser with molecular degrees of freedom such as: electronic motion, vibrational motion, and rotational motion. The time scales for each of these motions are different, approximately attosecond (10^{-18}) for the electronic motion, femtosecond (10^{-15}) for the vibrational motion, and picoseconds (10^{-12}) for the rotational motion. Compared to atoms, the molecules are not an isotropic system, and the ionization of the molecules depends on the alignment direction, i.e., the angle between the molecular axis and the polarization direction of the laser field.

5.2.1 Adiabatic and non-adiabatic alignment

Molecules can be aligned by a laser pulse adiabatically or non-adiabatically, based on the difference of the rotational period of the molecule and the duration of the aligning laser field. If the laser pulse is longer than the rotational period ($\tau_{pulse} >> \tau_{rot}$), the molecules are aligned adiabatically which means that molecules orient themselves in the direction of the field during the pulse and go back to the original field free state upon the adiabatic turn-off of the laser field [43, 82]. In the case when the pulse duration is shorter than the rotational period of the molecule ($\tau_{pulse} << \tau_{rot}$), an intense pulse transmits large amount of the angular momentum to the molecular system, which causes a periodically reviving non-adiabatic alignment that sets in only after the pulse is turned-off [82].

The classical understanding of the non-adiabatic alignment is as follows: consider the situation when we have randomly oriented molecules in space under the action of the electric field of a pulse. During the kick from the laser pulse, molecules will obtain angular momentum.

Diatomic molecules whose internuclear axis has a larger initial angle with respect to the laser field will experience more torque and rotate faster compared to molecules having smaller angle and rotating with smaller angular momentum. Eventually faster molecules catch up with slower molecules, and as a result localization of density occurs and maximum alignment is achieved. After reaching maximum alignment the molecules will keep rotating with different velocities and the alignment will be destroyed [80, 35].

5.3 Ionization of randomly oriented hydrogen molecules

As described above the angle dependent ionization is studied commonly using aligned molecules and linearly polarized laser pulses. This method has certain limitations.

i) Has limited angular resolution and

ii) Is not appropriate for heteronuclear molecules as it is insensitive to the molecular orientation.

A newer method developed by the Ottawa group [88] uses circularly polarized light to ionize molecules (H_2), measuring electron and ion in coincidence. Advantages of the method are

i) A much higher resolution and

ii) No alignment of molecules required.

The main idea behind an alignment-free experiment is to use circularly polarized laser pulses, so that BS is still anisotropic with fragments emerging mostly within a 10° angle from the plane of circular polarization. In the plane of polarization, however, there is no preferred direction for the rotating electric field vector, and the molecular axis direction within this plane is not affected by a circularly polarized pulse. It is important to note that the final drift momentum of any emitted electron will be opposite to the direction of the vector potential of the laser field at the moment of ionization. In the case of circularly polarized light the drift momentum of the electron is perpendicular to the direction of the laser electric field at the moment of the ionization because the vector potential trails the rotating electric field vector by a quarter-cycle (Fig. 5.1). One can determine the dependence of the ionization yield on the angle between the molecule and the rotating electric field vector by measuring the distribution of relative angles within the plane of polarization between an electron and a proton coming from the same molecule.

In their experiment Staudte *et al.* [88] used H_2 as a target with 40 fs 800 nm circularly polarized pulses of intensities varying between 2 and 4.5×10^{14} W/cm^2. They found that the experimental ionization anisotropy (ratio of the ionization probabilities for the molecules aligned perpendicular and parallel to the laser field polarization direction) decreased from 1.3 to 1.18 with increasing intensity. They introduced the theoretical model, which reproduced the decrease of the ionization anisotropy with increasing the peak intensity, but the result they got overestimated the anisotropy. The anisotropy measured by Staudte *et al*. [88] at large intensity approaches the rate ratio 1.17 which was predicted by the tunneling molecular-ADK theory [92]. The reason for this could simply be the saturation effect, with increase in intensity the ratio of ionization for the molecules parallel and perpendicular to the field polarization approaches unity. One more possibility is that with change in intensity the ionization mechanism changes and correspondingly changes the observed ionization anisotropy. For example, for 800 nm pulses of intensities in the range $1.0 - 2.5 \times 10^{14}$ W/cm^2 (I_p = 15.43 eV), the Keldysh parameter γ -varies from 0.7 to 1.15, and the ionization mechanism changes to multi-photon ionization as the intensity decreases and the anisotropy increases.

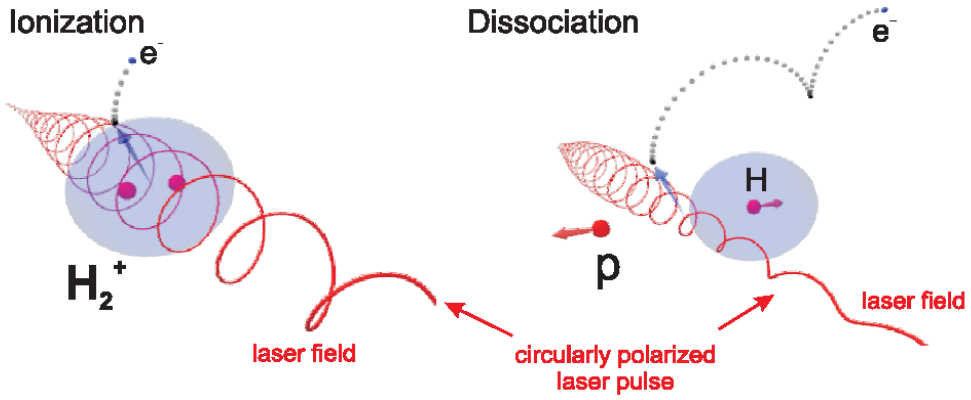

Fig. 5.1 Schematics of the process molecules undergo in the experiment (From [88]).
On the left, the ionization of the molecule by circularly polarized light, and on the right, the dissociation of the molecule into a proton and a hydrogen atom by the same pulse.

In our experiments, using the approach Staudte et. al [88] introduced, we further investigated the issues mentioned above. We used laser pulses of longer wavelength (1850 nm) and deuterium molecules as our target. The corresponding Keldish parameter ($\gamma < 0.5$) for 1850 nm at reasonable intensities for photo-ionization ($>10^{14}$ W/cm^2), corresponds to the tunneling regime.

5.4. Experimental setup

The 800 nm 1.5 mJ 35 fs pulses at 1 kHz repetition rate were generated by multi-pass Ti-sapphire amplifier. The pulses then were passed to the TOPAS optical parametric amplifier, which generated the 1850 nm laser pulses of 50 fs duration. After the fundamental and the signal (at 1415 nm) beams were separated, the 1850 nm idler beam had 120 μJ of energy per pulse (Fig. 5.2).

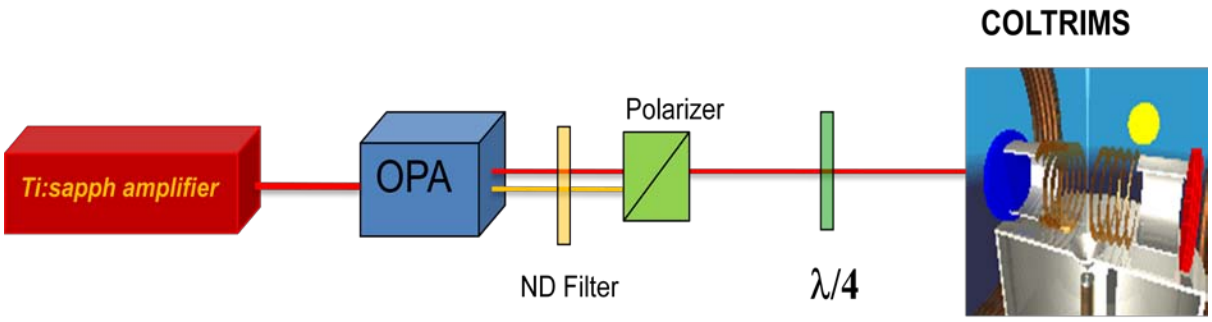

Fig. 5.2 Schematics of the setup used in our experiment.

For converting linearly polarized light to circularly polarized, we used a quarter waveplate from CVI Optics. After proper attenuation the beam was sent to the COLTRIMS apparatus were it was focused on a supersonic jet of deuterium molecules in the interaction region by a 75 mm focal length spherical on-axis mirror. The laser beam was normal to the gas jet and both of them were perpendicular to the axis of a uniform electric field (10 V/cm). The spectrometer was terminated on both sides by time and position sensitive delay-line anode detectors (Roendtek) for measuring electron and ion momentum in coincidence. A magnetic field of 13 Gauss, parallel to the spectrometer axis was applied to guide electrons to the detector and a smaller perpendicular magnetic field was supplemented to compensate for the Earth's magnetic field. The gas target density was adjusted so that much less than one charged fragment of each kind was detected per laser pulse. The peak intensity of the laser pulses were determined by measuring momentum distributions of intact D_2^+ ions as described in Chapter 4 [5].

5.5 Experimental results

We measured the relative angle between an emitted electron and a D^+ ion resulting in the plane of the circular polarization of our laser pulses from a single event [57]. In Fig. 5.3 the kinetic energy and the two-dimensional momentum spectra for D^+ ions is shown.

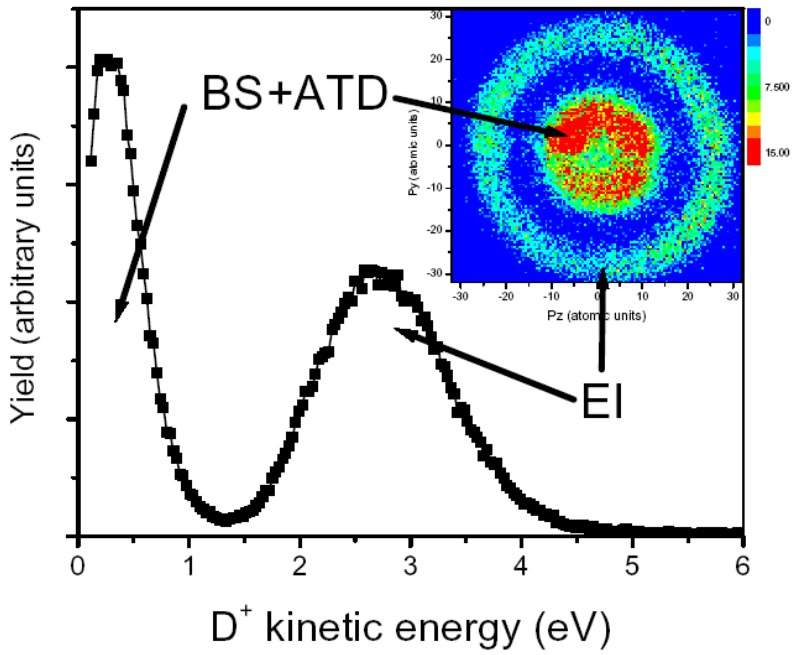

Fig. 5.3 Kinetic energy (KE) spectra of D^+ ions for circularly polarized, 1850 nm, 50 fs duration and 4×10^{14} W/cm^2 peak intensity laser pulse.
Inset: 2D momentum spectra for the ions. The low energies in the KE plot (connected with arrows to momentum spectra) correspond to BS and ATD, and the higher energy band corresponds to enhanced ionization (EI).

At the intensity used in our experiment (4×10^{14} W/cm^2 peak intensity) the energy spectrum includes two distinct bands. The lower energy band corresponds to one-photon BS and net two-photon ATD processes. In our analysis we could not resolve the BS and ATD bands and considered them together. At about 2.6 eV there is a broad peak, which corresponds to the double ionization (Coulomb explosion). We were only interested in the low energy band (0-1eV) (where deuterons are resulting from dissociation of the molecular ions) as we are measuring the angular dependence of a single ionization process. We were not able to detect the neutral D_0 fragment so we relied on the low overall count rate to ensure that both charged particles came from the same molecule.

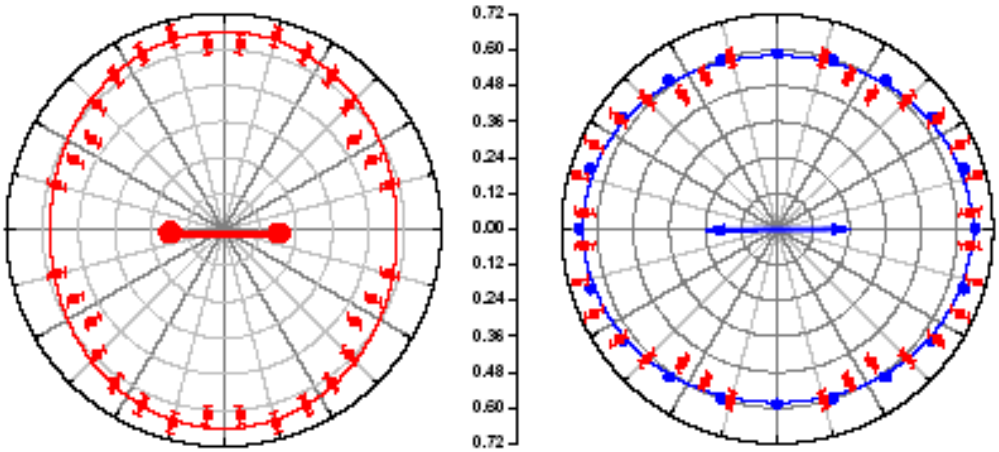

Fig. 5.4 Distribution of the relative angles between the ion and electron momentum. On the left, the experimental results for low energy 0-1 eV (red dots). Solid line corresponds to the best fit using the ellipse equation $A(\cos^2\theta + \varepsilon \sin^2\theta)$, where $\varepsilon = 1.15 \pm 0.05$ is the ratio of the coincident fragment and photoelectron yields at 90° and 0° angles. On the right, the theoretically calculated single ionization probability (blue dots) is compared to the experimental data (red dots are the same as the left ones but rotated by 90°). The probability is plotted as a function of the angle between the molecular axis and electric field polarization. The laser pulse used in the calculation was linearly polarized and had a 2×10^{14} W/cm^2 peak intensity. The blue solid line is a fit to the calculated anisotropy (for the best fit $\varepsilon = 1.12$).

In Fig. 5.4 the experimental distribution of the relative angles between the ion and electron momentum is shown. There is a slight anisotropy in the distribution with more electrons detected in direction perpendicular to the molecular axis. From the result we conclude that more molecules are ionized when their axes are parallel than when they are normal to the field since the ultimate drift velocity of a photoelectron is perpendicular to the instantaneous direction of the electric field vector at the moment of ionization. At the same field strength the ratio of the ionization probabilities for molecules aligned perpendicular and parallel to the laser field polarization is equivalent to the ratio of the photoelectron yields detected at angles of 0° and 90°. In our calculations the peak intensity of 2×10^{14} W/cm^2 for linearly polarized pulse is same as the 4×10^{14} W/cm^2 peak intensity for the circularly polarized pulses. From the experimental results we determine that for pulses with peak intensity of 4×10^{14} W/cm^2 the ratio of maximum and minimum ionization probabilities (corresponding to parallel and perpendicular alignments), is 1.15 (±0.05). This result agrees well with the values Staudte *et al* [88] obtained for hydrogen

molecules using 800 nm pulses and also agrees well with the result of the quasi-static molecular-ADK theory which assumes pure tunneling ionization [92].

5.6 Theoretically calculated ionization rates

For calculating ionization probabilities as a function of the angle between the molecular axis and the electric field of a linearly polarized laser pulse we developed a separate wave-function propagation model [38, 48, 91]. In this model we use the single active electron approximation to solve the time-dependent two-dimensional Schrödinger equation (TDSE) in the velocity gauge in Cartesian coordinates (we use atomic units, $e = m = \hbar = 1$),

$$i\frac{\partial}{\partial t}\Phi(x,y;t) = \left[\frac{P_x^2+P_y^2}{2} + \frac{P_x A(t)}{c} + V(x,y)\right]\phi(x,y;t) \qquad (5.1).$$

The soft-core Coulomb potential was used to model the electron-nuclei interaction

$$V(x,t) = -\sum_{j=\pm 1}\frac{Z_{eff}}{\sqrt{\left(x+j\frac{R_0}{2}\cos\theta\right)^2+\left(y+j\frac{R_0}{2}\cos\theta\right)^2+\alpha}} \qquad (5.2),$$

where P_x and P_y are the momentum components in x and y direction, and x and y are the electron coordinates in the plane of the laser polarization. The distance between nucleus is fixed at R_0 = 1.4, which corresponds to the equilibrium distance for the ground state of D_2. As mentioned earlier the laser polarization is linear in our calculation and it is pointing along the x axis. The angle between the laser polarization and the inter-nuclear axis is marked as θ. For a soft-core parameter α = 0.64 and an effective nuclear charge z_{eff} = 0.58 our single active electron model reproduces the ionization potential both at equilibrium internuclear distance and at infinite separation (with z_{eff} = 1). We use the split-operator Crank-Nicholson propagation scheme to solve the TDSE with a time step of 0.1. The numerical grid has 2000 and 800 points in the x and y direction, respectively, with the spatial steps $\Delta x = \Delta y = 0.3$. The laser electric field associated with the vector potential $\boldsymbol{A}$ is

$$E(t) = E_0 \sin(\omega t) sin^2\left(\frac{\pi t}{\tau}\right) = -\frac{\partial}{\partial t}A(t) \qquad (5.3),$$

with amplitude E_0, angular frequency ω and duration τ. The mask function applied was $\cos^{1/8}$ over a length of 60 and 30 from the ends of the rectangular numerical grid in x and y direction in order to suppress unphysical reflections. By calculating the probability for the electron to remain

bound P_{bound}, we can get the ionization probability as 1-P_{bound}. In order to ensure converged results, we propagate the wavefunction past the laser pulse until the ionization probability has stabilized.

The right column of the Fig. 5.4 shows the theoretically calculated ionization rate as a function of the angle θ for laser intensity 2×10^{14} W/cm^2, and wavelength and pulse duration of 1850 nm and 50 fs (FWHM), respectively. From the calculations we also conclude that molecules aligned parallel to the laser polarization are easier to ionize than those aligned perpendicularly, as expected. We obtained a value of 1.12 for the ratio of the ionization probabilities in the parallel and perpendicular directions to the polarization, which is in excellent agreement with our experimental value of 1.15±0.05.

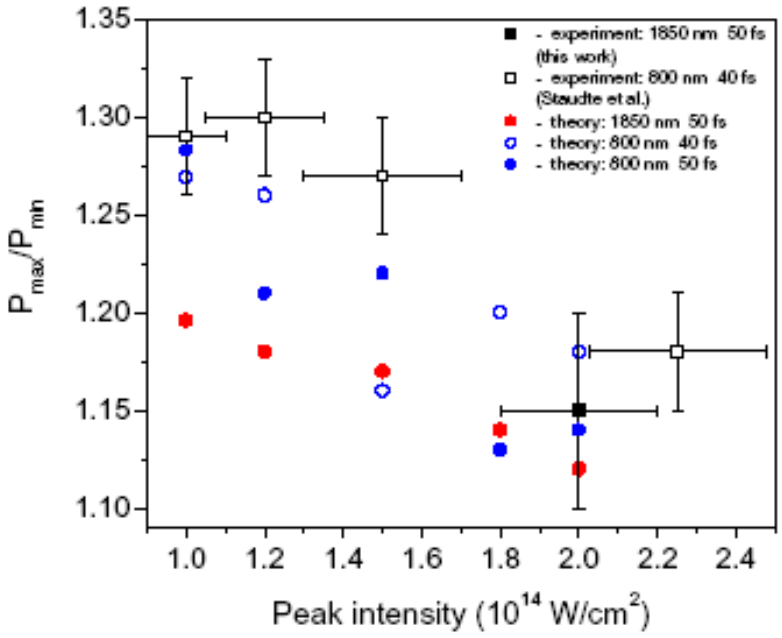

Fig. 5.5 Dependence of angular anisotropy of single ionization of D_2 on peak intensity. The black full and hollow squares correspond to our experimental results and results from the experiment done by Staudte et al [88]. Red dots represent the calculated anisotropy for 1850 nm, with 50 fs duration pulse. Hollow and full blue circles correspond to the theoretically calculated anisotropy for 800 nm but with 40 fs and 50 fs pulse duration cases respectively. The intensities for the experimental data were divided by 2 to compare to the theory.

In Fig. 5.5 the intensity dependence of the ionization anisotropy is shown for hydrogen molecules at 800 and 1850 nm wavelengths, with pulse lengths of 40 fs and 50 fs, as blue and red dots. The experimental results of Staudte *et al.* are also shown for comparison as black

hollow squares, and the full black square corresponds to our experimental result. One can notice that our theoretical results are slightly lower than the experimental ones. This slight discrepancy can be understood by the fact that we used a single intensity as peak intensity in our calculations, while in the experiment a range of intensities contributes to the final anisotropy due to spatial variations within the pulse. For lower intensities the anisotropy is higher and the single intensity calculations will give values, which are underestimated. Deviations in the intensity dependence of the anisotropy at 800 nm from a monotonous decrease are consistent with a numerical uncertainty in our calculated ionization probabilities of 0.3%.

5.7 Conclusion

In conclusion, using the coincidence measurements of the ions and the electrons we measure the angular dependence of the strong-field ionization probability of D_2 for 1850 nm circularly polarized pulse. We determined that this angular dependence exhibits a weak anisotropy with an ionization yield ratio of 1.15±0.05 favoring the ionization of molecules that are aligned parallel to the electric field. We also presented a 2D single active electron *ab initio* numerical model which accurately predicts the measured anisotropy, as well as its intensity dependence for both our experiment at 1850 nm and Staudte *et al.*'s at 800 nm wavelength. Both our experimental and theoretical values agree very well with the results of Staudte *et al.* for H_2, as well as with our own earlier estimates for D_2 obtained using dynamic alignment and few-cycle 800 fs pulses [16].

CHAPTER 6 - Dependence of bond softening and bond hardening on laser intensity, wavelength, and pulse duration for D_2^+

6.1. Introduction

The recent advances in femtosecond (fs) laser technology makes it possible to control, observe and analyze the time dependent nuclear dynamics in small molecules, and give us a better understanding of the basic concepts in quantum mechanics. With short and intense laser pulses it is possible to enable the time resolution of the nuclear motion in small diatomic molecules [19, 32, 40, 48, 49, 53, 76, 97].

Several researchers have been using time delayed laser pulses in pump-probe experiments with Coulomb explosion (CE) imaging of the molecular fragments. In such experiments, a neutral molecule is first ionized by a short pump-laser pulse [10, 14, 29, 37, 51, 55, 63, 66, 79, 84]. The pulses are only a few fs long and the pulse bandwidths are large compared to the vibrational level spacing. The pump pulse coherently excites a superposition of stationary vibrational states of the molecular ion, resulting in a moving nuclear wave packet. Using a second but delayed short probe-pulse the probability density of this wave packet can be imaged. The probe-pulse rapidly ionizes the molecular ion leading to its fragmentation by Coulomb explosion [25, 26, 44, 91]. From the kinetic energy release (KER) spectra for a sequence of pump-probe delays τ, the dynamics of the nuclear wave packet can be reconstructed [8, 37].

The time evolution of the wave packet can be calculated theoretically by solving the time dependent Schrodinger equation. Based on a quantum-mechanical model, we calculate the time evolution of an initial nuclear vibrational wave packet in D_2^+ generated by the rapid ionization of D_2 in an ultrashort pump-laser pulse. We plot the two-dimensional internuclear-distance-dependent power spectra by Fourier transformation of the nuclear probability density with respect to the time delay between the pump pulse and the instant destructive Coulomb-explosion imaging of the wave packet at the high-intensity spike of an intense probe-laser pulse, which serve as a tool for visualizing and analyzing the nuclear dynamics in D_2^+ in an intermittent external laser field. The external field models the pedestal to the central ultrashort spike of a

realistic probe pulse (Fig. 6.1). Variation in the intensity, wavelength, and duration of this probe-pulse pedestal allows us to identify the optimal laser parameters for the observation of field-induced bond softening and bond hardening in D_2^+.

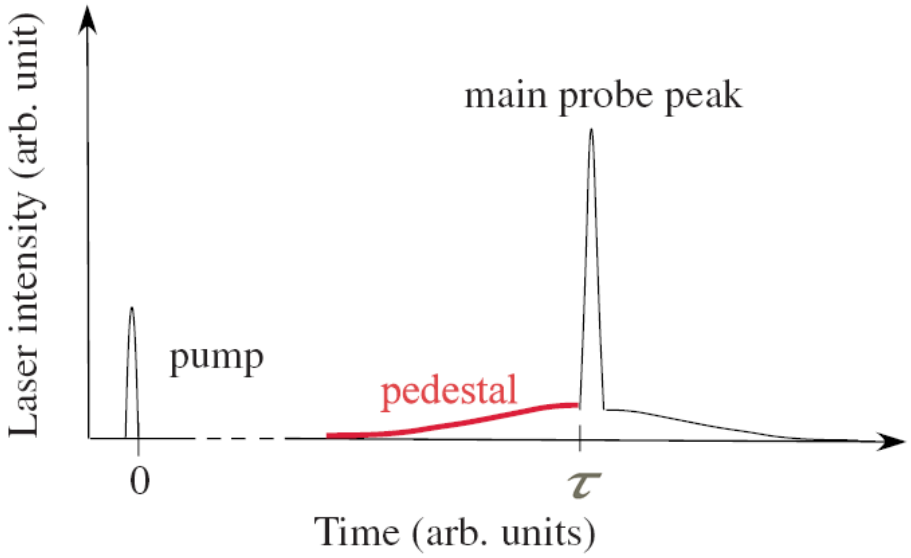

Fig. 6.1 Schematics of the pump and probe pulse sequence.
The main pulses are shown as black and the pedestal (Gaussian-shape) of the pulse as red. For our simulations we assume instantaneous CE by ionization in main peak of the probe pulse.

6.1.1 Schematics of pump-probe experiment

The schematic of the pump-probe setup is shown in Fig. 6.2. The first (pump) laser pulse ionizes a neutral D_2 molecule from its ground state and produces an ionic molecular wave packet. The resulting nuclear wave packet evolves on the $1s\sigma_g$ ground-state potential curve in the deuterium molecular ion within the Born-Oppenheimer (BO) approximation [18]. The wave packet will start to oscillate, and its propagation is monitored by the second (probe) pulse, which arrives after a certain time delay and removes the second electron and induces Coulomb explosion of the molecular ion which is CE imaged by the time-delayed intense probe laser. CE mapping [26, 39] allows the measured KER spectra [8, 37, 40, 55, 60, 69, 81] to be compared with theoretical models for the nuclear probability densities [44, 65, 68, 69, 91]. For instance, by direct numerical solution of the time-dependent Schrödinger equation using wave-packet propagation techniques (with simplified model assumptions, such as the representation of the

nuclear and/or electronic motion in reduced dimensionality [8, 24, 44, 48, 65, 91]), the approximate nuclear probability densities can be calculated for the simplest diatomic molecules, H_2^+ and its isotopologues. By recording the KER as a function of the delay τ the evolution of the nuclear probability density ρ(*R*,τ) [8, 37] is analyzed. The ρ(*R*,τ) graphs capture the nuclear dynamics in space (*R*) and time (τ) and allow the distinction of several pump-laser-induced phenomena, such as molecular fragmentation into different asymptotic dissociation channels and the coherent dephasing and revival [79] of bound vibrational wave packets in diatomic molecular ions [8, 16, 44, 61, 69, 81, 91].

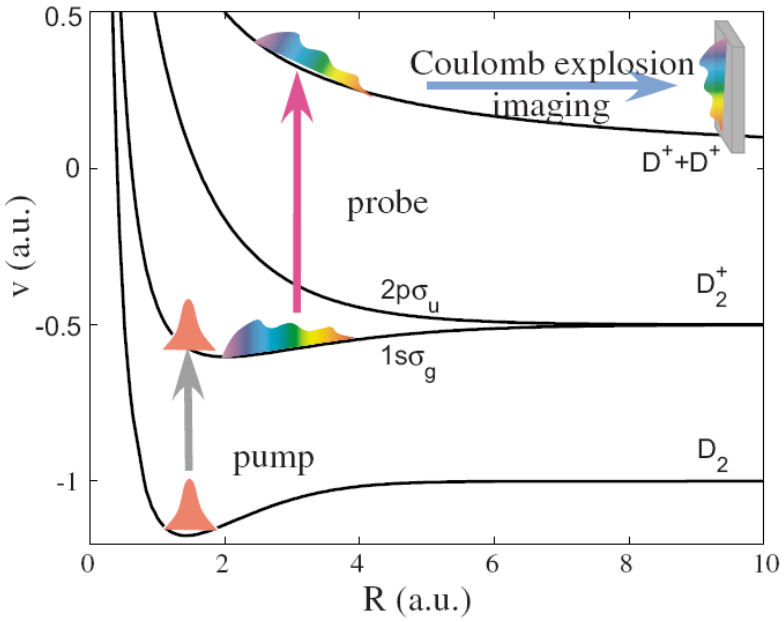

Fig. 6.2 Schematic diagram of the pump-probe setup.
A neutral wave packet is launched from D_2 potential curve to a D_2^+ $1s\sigma_g$ curve by the pump pulse. After a certain time delay an intense short probe pulse promotes the nuclear wave packet onto the $2D^+$ repulsive $1/R$ Coulomb explosion curve and allows for the detection of the fragment kinetic energy distribution.

6.1.2 Time series analysis of KER spectra

The time series analysis of the KER spectra is an alternative and less explored method for investigating the nuclear dynamics in diatomic (and possibly in more complex) molecules. This method applies equally well to nuclear probability densities that are calculated or derived from measured KER spectra by CE mapping and captures the nuclear dynamics in space and frequency. Basically in this method we are first eliminating the strong static background $\rho_{static}(R)$ in the nuclear probability density and then Fourier transforming $\rho_{dynamic}(R,\tau) = \rho(R,\tau) - \rho_{static}(R)$ as a function of τ over a finite range $0 < \tau < T$ at fixed internuclear distances. After this procedure we have the R-dependent representation of the nuclear probability density $\tilde{\rho}_{dynamic}(R,f)$ as a function of the frequency f (quantum-beat) and the power spectrum $P(R,f;T) = \left|\tilde{\rho}_{dynamic}(R,f)\right|^2$. The time-series analysis reveals features that are less obvious or not at all noticeable in the more conventional "space-time" analysis of KER spectra [8, 40, 44, 55, 61, 81, 91]. In previous investigations [91], the $P(R, f; T)$ was calculated, and the propagation of nuclear vibrational wave packets were examined in D_2^+ in comparison with the first measured *R*-dependent quantum beat spectra [40].

The pump and probe pulses need to be short enough (on the time scale of the nuclear vibrational motion) in order to resolve the nuclear dynamics in small diatomic molecules in time. The vibrational period for D_2^+ is about 20 fs and recent experiments succeeded in resolving the nuclear motion with pulses with a nominal length of about 6–8 fs [8, 40, 69]. Those intense and ultrashort pulses have shapes that strongly differ from the Gaussian or sin-squared profiles that are commonly used in model calculations. So in an attempt to model realistic pulses, we include a pedestal in addition to the main spike of the pulse. In particular, the pedestal-to-probe pulse can strongly modify the nuclear dynamics immediately before it is probed by the sudden ionization of the molecular ion in the *main* probe peak (Fig. 6.1). The time delays need to be sampled over a time interval of about 1ps, in order to distinguish adjacent vibrational quantum beats in D_2^+, and to produce KER power spectra of sufficient resolution [91]. This means that during a small fraction of the sampling time, a relatively weak pedestal field can leave a pronounced effect on the observed KER spectra. The pedestal pulses applied here will serve as prototypical

intermittent laser fields, for which we analyze the effects on the evolution of nuclear wave packets.

We analyze the nuclear motion in D_2^+ by discussing KER power spectra for an appropriate range of carrier frequencies, peak intensities, and pulse lengths of the oscillating laser field. This will allow us to (i) reveal the sensitivity of the laser-induced nuclear dynamics in response to the controlled change in the laser parameters frequency, intensity, and pulse length, (ii) assess the range of applicability of the Floquet interpretation [12,18] in *pulsed* laser small molecule interactions, and (iii) restrict the range of laser parameters at which transient field-induced effects, such as BS [1, 11, 21, 45, 54, 76, 83, 91, 95] into different asymptotic Floquet channels and BH [1, 11, 42, 46, 83, 91], are most prominently displayed. Unless indicated otherwise, we designate the vibrational ground states of D_2 and D_2^+ with the index $\nu = 0$ and excited states with $\nu \geq 1$.

6.2 Theory

6.2.1. Two-state model for the nuclear wave-packet dynamics in D_2^+

Assuming that the neutral D_2 molecules are singly ionized by an intense short pump-pulse, the quantum state of the resulting molecular ion can be approximated as

$$\Phi(\vec{r}, R; t) = \frac{1}{\sqrt{2}}\left[\chi_g(R,t)\phi_g(R,t) + \chi_u(R,t)\phi_u(R,t)\right] \tag{6.1}$$

where ϕ_g and ϕ_u are the D_2^+ electronic $1s\sigma_g$ and $2p\sigma_u$ states in BO approximation and $\vec{r}$ is the electron position vector. By projecting out the electronic states the bound and dissociating nuclear motions of the molecular ion can be described in this two-electronic-state model. For the evolution of the gerade χ_g and ungerade χ_u nuclear wave-function components a set of coupled equations can be obtained,

$$i\frac{\partial}{\partial t}\begin{pmatrix}\chi_g(R,t)\\ \chi_u(R,t)\end{pmatrix} = \begin{pmatrix}T_R + V_g(R) & D_{gu}(R)E(t-\tau)\\ D_{gu}(R)E(t-\tau) & T_R + V_u(R)\end{pmatrix} \times \begin{pmatrix}\chi_g(R,t)\\ \chi_u(R,t)\end{pmatrix} \tag{6.2}$$

where μ is the reduced mass of the nuclei, and $T_R = -\frac{1}{2\mu}\frac{\partial}{\partial R^2}$, $V_g(R)$ and $V_u(R)$ are the BO $1s\sigma_g$ and $2p\sigma_u$ potential curves. The linearly polarized laser field E is directed along the internuclear

axis, and rotation of the molecular ion is not taken into consideration. The dipole coupling between gerade and ungerade states is designated by $D_{gu} = \langle \phi_g | r | \phi_u \rangle$ [54].

We numerically solve Eq. (6.2) using the Crank-Nicholson method [44, 77, 91] with spacial steps ΔR=0.05 with R covering the range between 0.05 and 30.0 and time steps of Δt=1.0. (See [77, 91] for more details). We assume that the initial state of the molecular ion is bound,

$$\chi_g(R,0) = \sum_\mu a_\mu \chi_\mu(R)\,, \chi_u(R,0) = 0 \tag{6.3}$$

where $\{a_\mu\}$ are the set of amplitudes (in general complex) in the basis of stationary vibrational eigenstates $\{\chi_\mu\}$ of the D_2^+ electronic ground-state potential $V_g(R)$. The action of the pump pulse is modeled with Franck-Condon (FC) factors $\{|a_\mu|^2\}$ in sudden approximation and all phases are randomly set to zero in order to obtain the set of real amplitudes $\{a_\mu\}$ for the bound initial wave packet. Using imaginary time propagation the trial function on the ground-state BO potential curve of D_2 is propagated and the ground state wave function χ_0 of the neutral parent molecule is calculated. Subsequent projection on the D_2^+ vibrational states $\{a_\mu = \langle \chi_\mu | \chi_0 \rangle\}$ generates the real function $\chi_g(R,0)$. Without an external laser field, the two states in Eq. (6.2) are decoupled, and the nuclear wave function evolves as a bound nuclear wave packet on the $1s\sigma_g$ potential curve, undergoing characteristic cycles of dephasing and revival [44, 91].

The main peak of the probe pulse is time-delayed from the probe-pulse and is assumed to instantaneously ionize the molecular ion and induce CE. On the other hand, the probe-pulse pedestal is supposed to be weak enough to not contribute to the fragmentation of the molecular ion by CE. We do not include a pedestal to the pump pulse in our model (Fig. 6.1) as it would not change our numerical results presented below. Immediately following the end of the (main) pump pulse the simulation of the evolution of the initial wave packet in D_2^+ starts at time t=0 for a given delay τ, and ends at time t=τ, immediately preceding the main probe pulse, as indicated in Fig. 6.1. During the evolution, the pedestal (thick red line in Fig. 6.1)

$$E(t,\tau) = E_0 \sin[\omega(t-\tau)] exp\left[-2ln2\left(\frac{t-\tau}{L}\right)^2\right] \tag{6.4}$$

is the only external field that couples χ_g and

$$\chi_u(R,t) = \int_0^\infty dE\, a_E e^{-iEt} \chi_E(R)\,, \tag{6.5}$$

leading to the correlated motion of the nuclear wave packet on the $1s\sigma_g$ and $2p\sigma_u$ D_2^+ BO potential curves. The pedestal is characterized by its amplitude E_0, frequency ω, and the duration [full width at half maximum (FWHM) in the laser intensity] L. The dissociating part χ_u of the

nuclear wave packet is written in terms of (continuum) eigenstates $\{|\chi_E\rangle\}$ in the $2p\sigma_u$ BO potential with (undetermined) coefficients $\{a_E\}$. The numerical results for a range of these parameters will be discussed in Sec. 6.3 below.

6.2.2. R-dependent quantum-beat power spectrum

The amplitudes $\{a_\mu\}$ in Eq. (6.3) remain time independent during the field-free propagation from t=0 to the probe time delay τ. The nuclear probability density as a function of time at τ is

$$\rho(R,\tau) = \int dr|\Phi(r,R;\tau)|^2 = \left|\chi_g(R,\tau)\right|^2 + |\chi_u(R,\tau)|^2$$
$$= \sum_\mu \left|a_\mu\right|^2 \left|\chi_\mu(R)\right|^2 + \sum_{\mu\neq\nu} a_\mu^* a_\nu e^{-i(E_\nu - E_\mu)\tau} \chi_\mu^*(R)\chi_\nu(R) \qquad (6.6)$$

The diagonal term in μ (second line) is time independent and gives an incoherent background to the wave function probability density. By subtracting the diagonal contribution we get rid of incoherent static terms in Eq. (6.6). By Fourier transforming the coherent terms over the finite sampling time T, and taking the square of the result, we obtain the power spectrum

$$P(R,\omega;T) = \left|\sum_{\mu,\nu=0}^{N} a_\mu^* a_\nu \chi_\mu^*(R)\chi_\nu(R)\delta_T(\Delta\omega_{\mu,\nu} - \omega)\right|^2 \qquad (6.7)$$

where the complex-valued distribution is given as

$$\delta_T(\Omega) \equiv \frac{1}{2\pi}\int_0^T dt e^{i\Omega t} = \frac{1}{\pi} e^{i\Omega \mathrm{T}/2} \frac{\sin(\Omega \mathrm{T}/2)}{\Omega} \qquad (6.8)$$

and centered at the quantum-beat energies $\Delta\omega_{\mu,\nu}=\omega_\nu-\omega_\mu$. It is broadened due to the Fourier transformation over a *finite* time interval. In the limit of large sampling times, it becomes identical with the usual delta "function," and the power spectrum $P(R, \omega \infty)$ reproduces the quantum-beat spectrum at infinite resolution. In contrast, T=3 ps yields a finite-energy resolution of 2.7 meV, which allows for the distinction of quantum beats between virtually all populated vibrational states in the hydrogen molecular ion in $P(R, \omega ; T)$. Further details on the properties and interpretation of $P(R, \omega; \mathrm{T})$ can be found in [91].

It is important to note that result (6.7) was derived under the assumption of *free* wave-packet propagation. It does not apply if external fields are present during the time propagation. However, it nevertheless constitutes a valuable guideline for the interpretation of external field effects in molecular power spectra if the external field acts during a time interval that is short

compared to *T*. This condition is fulfilled in the recent experiment by Feuerstein *et al.* [40], where power spectra were measured with a sampling time of T=3 ps while the nuclear wave packet was exposed to an intermittent electric laser for less than 100 fs. All numerical examples in Sec. 6.3 below are calculated with T=3 ps and for pedestal pulse lengths of 200 fs or less. Equation (6.7) will therefore help in the interpretation of our numerical results. As shown below, this equation correctly describes the quantum-beat energy and several features that are related to the bound motion of the nuclei. It fails where strong-field effects become dominant, in particular, near the curve crossing points between field-dressed adiabatic molecular potential curves.

6.3. Numerical results

The interactions of the continuum wave (cw) laser field with the molecule in Floquet theory are described using adiabatic laser-dressed potential curves [46, 83, 95], which are also referred to as "Floquet adiabatic molecular potential curves" or simply "Floquet curves." The Floquet curves represent the field-free molecular potential curves that are shifted in energy due to the interaction with the laser field. The shift in energy depends on the net number of photons the molecule absorbs from the field. The absolute value of the Floquet energies is irrelevant and is given relative to a laser field with a fixed macroscopic number of photons. In our simulation we consider short laser pulses for which the cw Floquet picture may be not applicable without restrictions. Floquet potential curves are a suitable reference for the description of laser-molecule interactions with laser pulses of finite duration.

Fig. 2.8 shows the Floquet adiabatic potential curves for two different intensities, $5\text{x}10^{11}$ and 10^{13} W/cm^2 for D_2^+ in a 500 nm cw laser field, based on the two lowest field-free diabatic electronic potential curves of the molecular ion, $V_g(R)$ and $V_u(R)$ [13]. In the Floquet picture, field-free potential curves combine to form the field-dressed adiabatic potential curves. The Floquet curves are labeled as $1s\sigma_g - 2n\omega$ and $2p\sigma_u - (2n-1)\,\omega$, specifying the corresponding field-free potential curves and the net number of photons n that are released to the photon field. The dipole-allowed coupling between field-free potential curves of gerade and ungerade symmetries [18], due to the absorption or release of an odd number of photons, leads to characteristic "avoided" crossings between Floquet curves. The avoided crossings near internuclear distances of R=4 and R=3 originate in the exchange of one and three photons, respectively, between the

molecular ion and cw laser field. An increase in the laser intensity increases the gap between adjacent adiabatic field-dressed potential curves.

Depending on the laser intensity the potential well can be formed near avoided crossing point by the potential curves. The well is referred to as BH well, in which molecular probability density is trapped and the corresponding quantum states are called BH states. The shape of the BH well depends on the laser intensity [1, 11, 42, 46, 83]. At higher intensities it becomes shallower and wider, and, at sufficiently high intensities, looses the ability to bind BH states. In contrast to the BH well, the less energetic Floquet potential curve below the gap forms a barrier that may enable BS [1, 11, 21, 45, 76, 83, 95], i.e., dissociation of the molecule due either to classically allowed over-the-barrier escape or by tunneling.

The KE is determined by the number of absorbed photons. The dipole-allowed absorption of one or three photons leads to dissociation into the 1-ω and 3-ω dissociation channel, respectively. Dissociation by the effective absorption of an even number of photons can also occur, without violating the dipole selection rule, by proceeding over two avoided crossings. For example, exposed to sufficiently large laser intensities, D_2^+ can dissociate into the 2-ω channel by first absorbing three and then releasing one photon.

Even though the numerical results presented in this work are in strong support of the interpretation of the laser influenced nuclear motion in D_2^+ based on (time independent) Floquet potential curves, we briefly mention an interesting alternative *dynamical* interpretation [23, 67]. BH, which is also referred to as "vibrational trapping" or "dynamical dissociation quenching," has been discussed by Châteauneuf *et al.* [23] in terms of the time-periodic potential curves $V_{\pm}(R, t)$ that are obtained by diagonalization of the field-free $1s\sigma_g$ and $2p\sigma_u$ BO potential curves subject to the time-dependent dipole coupling matrix elements $D_{gu}(R, t)$ at fixed t and R. The authors showed that the dynamical interplay between the time-dependent force associated with the upper $V_+(R, t)$ curve and the moving nuclear wave packet can lead to the efficient quenching of the laser-induced dissociation. This is in agreement with the classical interpretation of the nuclear motion receiving an inward directed restoring force if the moving potential barrier included in $V_+(R, t)$ is appropriately synchronized with the nuclear motion. This dynamical interpretation of BH was experimentally confirmed for the nuclear motion in H_2^+ and D_2^+ in a 70 fs 1.6 μm laser pulse that was modulated on the time scale of the nuclear vibrational motion (10 fs) [67]. The

modulation was obtained by the coherent superposition of two laser pulses and provided an adjustable pulse envelope that controls the motion of the vibrational wave packet.

In secs. 6.3.1-6.3.3, we will discuss the bound and dissociating nuclear motion of D_2^+ in a laser pulse by examining how power spectra are affected by the laser pedestal parameters intensity, frequency, and duration. Even though all simulations were carried out for (pedestal) laser pulses with a finite pulse length, we will show that the terminology developed based on the Floquet picture is appropriate. For example, even though stable BH states can only exist in cw laser fields, we find evidence for transient BH states in laser *pulses* over a large range of pulse lengths.

6.3.1. Intensity dependence

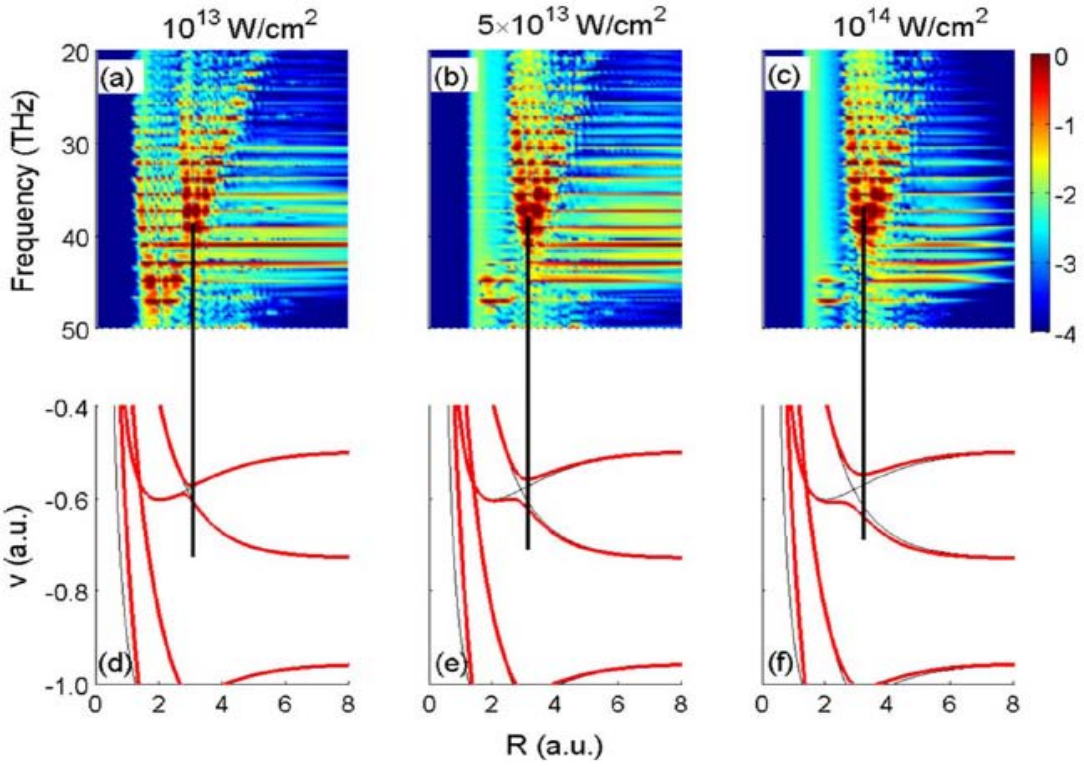

Fig. 6.3 Dependence of initial FC vibrational wave packet of D_2^+ on pedestal intensity. Graphs are plotted for 200 nm pedestal laser pulses with different intensities of $0.1x10^{14}$ W/cm^2 [(a) and (d)], $0.5x1x10^{14}$ W/cm^2 [(b) and (e)], and $1x10^{14}$ W/cm^2 [s (c) and (f)]. Graphs (a)-(c) correspond to quantum-beat frequency and internuclear distance dependent power spectra in a logarithmic scale, and graphs (d)-(f) are field-dressed potential curves (res lines) for corresponding intensities. Field-free potentials are plotted as thin black lines.

Fig. 6.3 shows the R-dependent power spectra $P(R,\omega;T)$ for D_2^+ propagating through 200 nm 20 fs (FWHM) Gaussian pedestal laser pulses for different peak intensities (upper panels) and the corresponding Floquet field-dressed potential curves which are displayed in red in the lower panels. The three columns show results for pedestal intensities of 10^{13} (left), $5x10^{13}$ (middle), and 10^{14} W/cm^2 (right column). Note that the field-free adiabatic molecular potential curves are also included in the lower panels as thin black lines. As for all other numerical results shown further below, the molecular ion is assumed to be produced by the rapid ionization of D_2 and is characterized by a FC distribution of stationary vibrational states, as described above.

For the frequency and R range shown in Fig. 6.3, the R dependence in the power spectra [7] reflects the nodal structure of the product of the probability densities $|a_\mu|^2$ and $|a_\nu|^2$ of the two adjacent stationary vibrational states $|\chi_\mu\rangle$ and $|\chi_\nu\rangle$ that beat against each other with the frequency $f = \Delta\omega_{\mu,\nu}/2\pi$ [91]. The thin black vertical lines facilitate the association of minima of the 1-ω BH wells in the power spectra (upper row of graphs in Fig. 6.3) with BH wells in the Floquet potential curves (lower row). For the displayed intensities, the power spectra show a significant amount of nuclear probability density that is intermittently trapped in the 1-ω BH well.

The nuclear probability density in the 1-ω BH well increases with intensity at the expense of probability that is associated with the bound motion of the molecular ions in field-dressed $1s\sigma_g$ potential curve. The power spectra confirm the intuitive expectation that dissociation across the 1-ω BS barrier, either by classical over-the-barrier motion of the two nuclei or by tunneling, (i) increases with increasing peak intensity and (ii) progresses by first depleting the highest vibrational state components of the nuclear wave packet with vibrational quantum numbers $\nu \geq 4$ (at quantum-beat frequencies near 40 THz) (left column in Fig. 6.3) to the lowest vibrational components of the initial FC distribution (right column).

6.3.2. Wavelength dependence

For shorter wavelengths and otherwise identical laser parameters, the character of the power spectra changes. In comparison with the 200 nm results in Fig. 6.3, the power spectra calculated for 800 nm in 6.4 indicate that the nuclear motion in D_2^+ sensitively depends on the carrier wavelength.

To a large extent, this change can be understood within the Floquet picture. As the photon energy decreases, the spacing in energy between Floquet potential curves decreases. This decrease increases the significance of couplings between more than two curves, which, in turn, may result in the overlap of (1-ω with 3- ω) BH wells and their bond-prohibiting flattening. At 800 nm and 10^{13} W/cm^2 peak intensity (left column in Fig. 6.4), the power spectrum shows only weak evidence for the temporary trapping of nuclear probability density in the 1-ω BH well that is centered near *R*=5. The molecular ion remains most likely bound in the electronic ground state. At the higher intensities (middle and right columns), dissociation via BS becomes increasingly important but cannot be as clearly assigned to the 1-ω BS barrier as for the case of 200 nm wavelength.

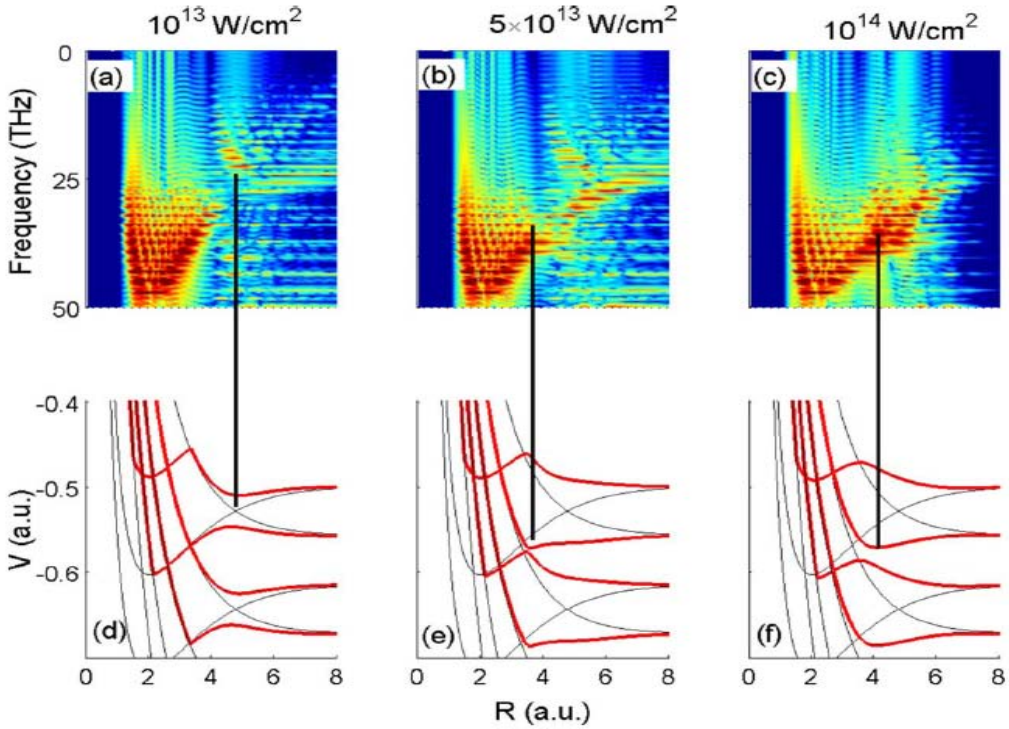

Fig. 6.4 Same as Fig. 6.3, but for 800 nm pedestal laser pulses.

At 800 nm and $5x10^{13}$ W/cm^2 (middle column in Fig. 6.4), the 1-ω BH well has disappeared in the Floquet potential curve (graph e) and BH is mostly confined to the 3-ω BH well centered at smaller distances near *R*=3.5 in the power spectrum. The same applies to the highest shown intensity (10^{14} W/cm^2, right column) where dissociation via 1-ω, and to a lesser extent, 3-ω BS, strongly decreases the molecular ion's chance for survival in the bound electronic ground state. Note that graph (b) also shows weak evidence for BH states in the 1-ω well near *R*=5 due to temporary vibrational trapping during the increasing laser intensity of the pedestal, although graph (e) would prohibit such states.

A more systematic study of the wavelength dependence of BS and BH is shown in Fig. 6.5 for power spectra (upper row) and Floquet potential curves at a fixed intensity of 10^{13} W/cm^2. Since the crossing point in the field-free potential curves (thin black lines in the lower panels) changes with the photon energy, we expect that the laser wavelength will affect BS and BH.

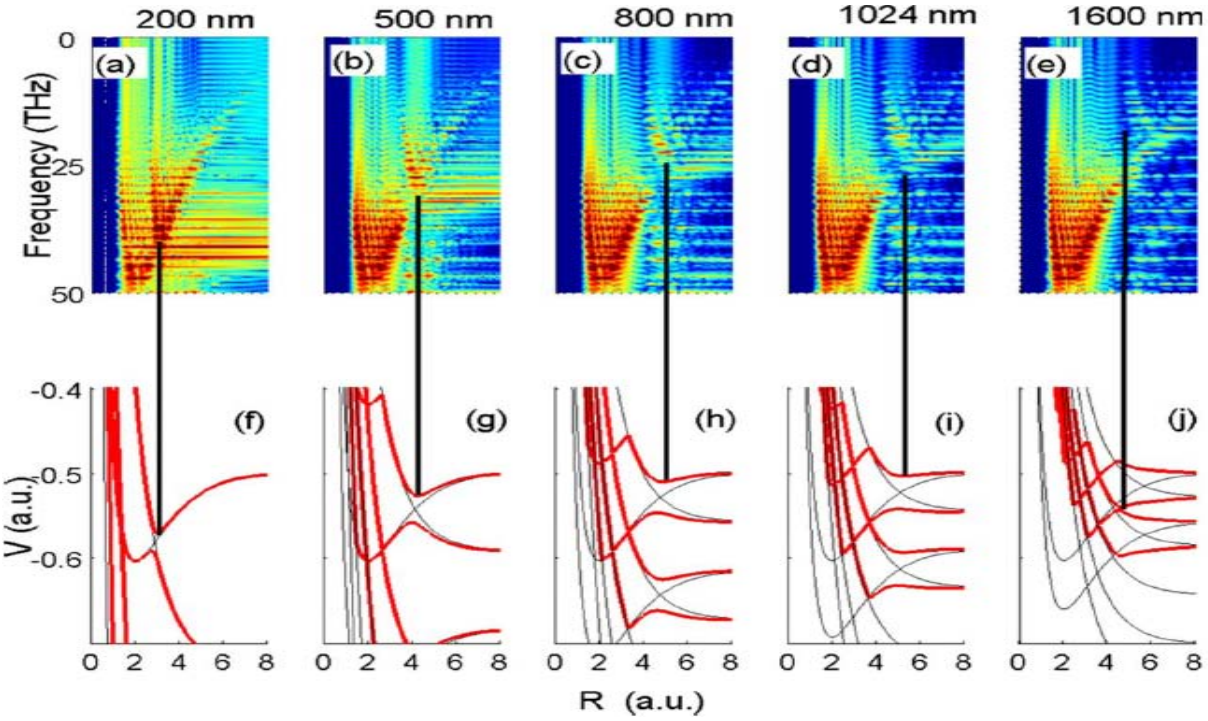

Fig. 6.5 Dependence of the initial FC vibrational wave packet of D_2^+ on the laser wavelength (Same logarithmic color scale as in Fig. 6.3). Graphs are plotted for 10^{13} W/cm^2 peak intensity pedestal laser pulses with different wavelength of 200 nm [(a) and (f)], 500 nm [(b) and (g)], 800 nm [(c) and (h)], 1024 nm [(d) and (i)], and 1600 nm [(e) and (j)]. Graphs (a)-(e) correspond to quantum-beat frequency and internuclear distance dependent power spectra in a logarithmic scale, and graphs (f)-(j) are field-dressed potential curves (res lines) for corresponding intensities. Field-free potentials are plotted as thin black lines as above.

The power spectra in graphs (a)–(e) show that dissociation by BS decreases with increasing wavelength, while the 1-ω BH well moves to larger internuclear distances. For 200 nm wavelength graphs (a) and (f) show a very prominent 1-ω BH well due to the strong coupling between the $1s\sigma_g$ and $2p\sigma_u$ electronic states. For this wavelength, all vibrational eigenstates in the initial FC distribution above v=2 are being depleted by BS, while the deep BH well traps even the highest initially occupied vibrational states.

For 500 nm (Figs. 6.5(b) and 6.5(g)) the 1- ω BH well remains populated but receives less probability density than for the case of 200 nm, while the nuclear motion is more likely to remain bound in the electronic ground state. This trend continues for 800, 1024, and 1600 nm (three right columns in Fig. 6.5) to the point that BH in the 1- ω well disappears at 1600 nm. This also follows from the comparison of Figs. 6.3(c) and 6.4(c) above. As the wavelength increases, BS through and over the 3- ω well becomes energetically possible for an increasing number of stationary vibrational states of the nuclear wave packet.

However, as the simulated power spectra show, the peak intensity of 10^{13} W/cm^2 is too low for three-photon processes to become relevant. Therefore, 3-ω BS and BH are not clearly noticeable in Fig. 6.5. In the left four columns of Fig. 6.5, the positions of the 1-ω BH well agree in power spectra and Floquet potential curves. At 1600 nm, however, according to the Floquet picture the 1- ω BH has disappeared and BH is expected to happen near the 3- ω crossing point (Fig. 6.5(j)). This prediction of the cw Floquet picture is not fully confirmed in the power spectrum in Fig. 6.5(e) that shows very weak evidence of 1-ω BH states centered near R=7 and no apparent traces of 3-ω BS or BH.

This mismatch is related to the fact that the Floquet picture assumes infinite pulse lengths, while at 1600 nm the power spectrum simulates the propagation of the nuclear wave packet across a pedestal pulse with a length of L=20 fs (FWHM), corresponding to the illumination of the wavepacket by the pedestal laser pulse over just two optical cycles and with a rapidly changing envelope. We therefore interpret this discrepancy as due to both the onset of the breakdown of the Floquet picture for short pulses, and more importantly, an *effective* laser intensity in the power spectra that is much smaller than the peak intensity for which the Floquet curves were calculated.

6.3.3. Pulse-length dependence

The combined effect on the power spectra of changing pulse duration and wavelength is shown in Fig. 6.6. The panels in this figure are ordered with pedestal wavelengths increasing from 200 (top) to 1600 nm (bottom). The pedestal length increases from L=50 (FWHM, left) to 200 fs (right). For each wavelength (each row), the BH probability decreases with increasing pulse length. Even though one might expect longer pedestal pulses to enable more pronounced BH due to longer trapping times, our simulations show the opposite trend which we assign to the dominant influence of the pulse energy. Longer pedestals transfer more energy to the molecule. This favors both dissociation by BS directly out at the electronic ground state (leaving less probability to be potentially trapped in a BH well) and the decay of BH states by nonadiabatic couplings to dissociative potential curves that are neglected in the BO approximation [18].

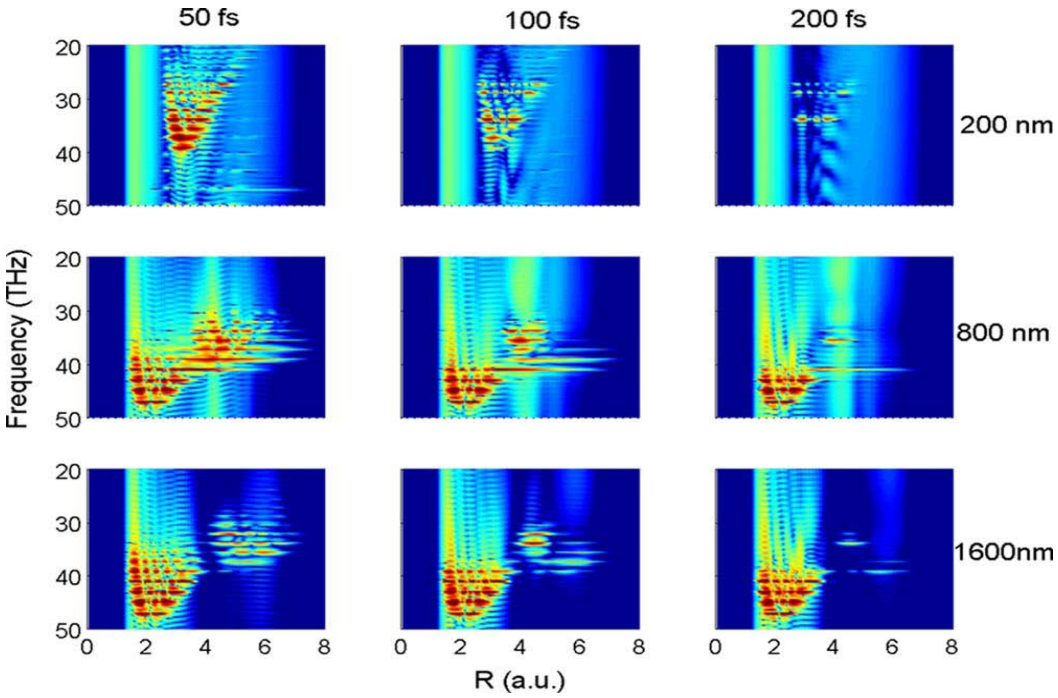

Fig. 6.6 Quantum-beat frequency and internuclear distance dependent power spectra in log scale.
(Same color scale as in Fig. 6.4). For fixed peak intensity of 10^{14} W/cm^2 the propagation of an initial FC wave packet is plotted for different (200, 800, 1600 nm) wavelengths and pedestal lengths (FWHM 50, 100, and 200 fs).

At shorter wavelengths, the same pedestal pulse envelope includes more optical cycles. Thus, the power spectra in Fig. 6.6 with the shortest wavelength and longest pulse duration are

most amenable to their interpretation within the Floquet picture. However, this trend is somewhat difficult to follow over a large range of pulse lengths, since, for high pulse durations (high pulse energies) BS can dominate to the point that all bound states become depleted. This is illustrated in the top right corner of Fig. 6.6. For a wavelength of 200 nm (top row), BS dissociation is rapidly depleting the electronic ground state and leaves a noticeable population in the 1-ω BH well only for the lowest shown pulse energy (L=50 fs). At 800 and 1600 nm, in contrast, the electronic ground state remains populated at all displayed pulse lengths but, as expected, gets increasingly depleted with increasing pulse length by BS over and through the 1-BS barrier. The comparison of all panels in Fig. 6.6 suggests that BH is most pronounced at the shortest wavelengths and for the shortest pedestals. The comparison with Fig. 6.3 above shows that BH at short wavelengths is robust over a large range in peak intensities.

6.4. Conclusion

We imaged the nuclear dynamics of the D_2^+ molecules in short laser field with different peak intensities, wavelengths, and pedestal lengths by simulating the R-dependent quantum-beat power spectra. The power spectra were analyzed in terms of field-dressed Floquet potential curves focusing on dissociation by BS and BH. Except for the longest wavelengths used in our simulations (1600 nm), we confirmed the Floquet picture as appropriate for characterizing the main features of the nuclear dynamics in few-cycle laser pulses despite its inherent cw assumption. Our simulations suggest that pulses with a wavelength between 200 to 300 nm, a peak intensity of about 10^{14} W/cm^2, and a duration of less than 50 fs (FWHM) are well suited for the observation of transient vibration trapping of the molecular motion in the 1-ω BH well. At wavelengths of 1600 nm, we found that dissociation proceeds via both 1-ω and 3-ω BS. For the same wavelength, our simulations indicate transient trapping in the 3-ω BH well. To the best of our knowledge, existing technology [5, 8] allows for the detailed experimental test of our findings.

CHAPTER 7 - Conclusion

In conclusion, we covered the basics concepts and theory related to the behavior of atoms or molecules in strong laser fields, experimental setup used in our experiments and the technique of data processing in chapters 2 to 4.

In chapter 5, we measured the angular dependence of the strong-field ionization probability for D_2 in 1850 nm circularly polarized infrared laser pulses without having to align the molecules first. We determined that this angular dependence exhibits a weak anisotropy with an ionization yield ratio of 1.15±0.05 favoring the ionization of molecules that are aligned parallel to the electric field. We also presented a 2D single active electron *ab initio* numerical model which accurately predicts the measured anisotropy, as well as its intensity dependence for both our experiment [57] at 1850 nm and Staudte *et al.*'s at 800 nm wavelength [88]. Both our experimental and theoretical values agree very well with the results of Staudte *et al.* for H_2, as well as with our own earlier estimate for D_2 [16] obtained using dynamic alignment and few cycle 800 fs pulses.

In chapter 6, we investigated the nuclear dynamics in D_2^+ for different peak intensities, wavelengths, and pedestal lengths of the laser pulses, based on simulated *R*-dependent quantum-beat power spectra [58]. By analyzing these spectra in terms of field-dressed Floquet potential curves we focused on dissociation by BS and transient binding of the nuclear motion by BH. We confirmed that, despite the incoherent cw assumption, the Floquet picture is suitable for characterizing the main features of nuclear dynamics, such as BS, BH in few-cycle laser pulses, except for the longest wavelength we used in simulations (1600 nm). From the simulations we concluded that peak intensity of about 10^{14} W/cm^2, pulses with a wavelength between 200 to 300 nm, and a duration of less than 50 fs (FWHM) are most suitable for the observing the vibration trapping of the molecular motion in the 1- ω BH well. At wavelengths of 1600 nm dissociation can proceed via both 1-ω and 3-ω BS, and our simulations indicate transient trapping in the 3-ω BH well at the same wavelength. Existing technologies [49, 40] can be used to test our findings experimentally.

Bibliography

[1]. H. Abou-Rachid, T. T. Nguyen-Dang, and O. Atabek, J. Chem. Phys. **114**, 2197 (2001).

[2]. P. Agostini, F. Fabre, G. Mainfray, G. Petite, and N. K. Rahman, Phys. Rev. Lett. **42**, 1127 (1979).

[3]. M. V. Amosov, N. B. Delone, and V. P. Krainov, Sov. Phys. JETP **64**, 1191 (1986).

[4]. A. S. Alnaser, S. Voss, X. M. Tong, C. M. Maharjan, P. Ranitovic, B. Ulrich, T. Osipov, B. Shan, Z. Chang, and C. L. Cocke, Phys. Rev. Lett. **93**, 113003 (2004).

[5]. A. S. Alnaser, X. M. Tong, T. Osipov, S. Voss, C. M. Maharjan, B. Shan, Z. Chang, C. L. Cocke, Phys. Rev. A **70**, 023413 (2004).

[6]. A. S. Alnaser, X. M. Tong, T. Osipov, S. Voss, C. M. Maharjan, P. Ranitovic, B. Ulrich, B. Shan, Z. Chang, C. D. Lin, and C. L. Cocke, Phys. Rev. Lett. **93**, 183202 (2004).

[7]. A. S. Alnaser, B. Ulrich, X. M. Tong, I. V. Litvinyuk, C. M. Maharjan, P. Ranitovic, T. Osipov, R. Ali, S. Ghimire, Z. Chang, C. D. Lin, and C. L. Cocke, Phys. Rev. A **72**, 030702(R) (2005).

[8]. A. S. Alnaser, C. M. Maharjan, X. M. Tong, B. Ulrich, P. Ranitovic, B. Shan, Z. Chang, C. D. Lin, C. L. Cocke, and I. V. Litvinyuk, Phys. Rev. A **71**, 031403(R) (2005).

[9]. T. Osipov, PhD thesis, KSU 2003.

[10]. S. Baker, J. S. Robinson, C. A. Haworth, H. Teng, R. A. Smith, C. C. Chirilă, M. Lein, J. W. G. Tisch, J. P. Marangos, Science **312**, 424 (2006).

[11]. A. D. Bandrauk and M. L. Sink, J. Chem. Phys. **74**, 1110 (1981).

[12]. S. R. Barone, M. A. Narcowich, and F. J. Narcowich, Phys. Rev. A **15**, 1109 (1977).

[13]. D. R. Bates, K. Ledsham, and A. L. Stewart, Philos. Trans. R. Soc. London, Ser. A **246**, 215 (1953).

[14]. A. Bhattacharjee and K. R. Dastidar, Phys. Rev. A **72**, 023419 (2005).

[15]. N. Bloembergen, Encounters in Nonlinear optics, Harvard University, (1996).

[16]. I. A. Bocharova, H. Mashiko, M. Magrakvelidze, D. Ray, P. Ranitovic, C. L. Cocke and I. V. Litvinyuk, Phys. Rev. A **77**, 053407 (2008)

[17]. R. W. Boyd, Nonlinear Optics, Academic Press, 2003. Second edition.

[18]. B. H. Bransden and C. J. Joachain, Physics of Atoms and Molecules, 2nd ed. (Prentice-Hall, London, 2003).

[19]. T. Brixner, T. Pfeifer, G. Gerber, M. Wollenhaupt, and T. Baumert, in Femptosecond Laser Spectroscopy, edited by P. Hannaford (Springer, New York, 2005), Chap. 9.

[20]. J. P. Brichta, W-K Liu, A. A. Zaidi, A. Trottier, and J. Sanderson J. Phys. B **39**, 3769 (2006)

[21]. P. H. Bucksbaum, A. Zavriyev, H. G. Muller, and D. W. Schumacher, Phys. Rev. Lett. **64**, 1883 (1990).

[22]. K. S. Budil, P. Salieres, M. D. Perry, A. L'Huillier, Phys. Rev. A **48**, R3437 (1993).

[23]. F. Châteauneuf, T. T. Nguyen-Dang, N. Ouellet, and O. Atabek, J. Chem. Phys. **108**, 3974 (1998).

[24]. S. Chelkowski, P. B. Corkum, and A. D. Bandrauk, Phys. Rev. Lett. **82**, 3416 (1999).

[25]. S. Chelkowski and A. D. Bandrauk, Phys. Rev. A **65**, 023403 (2002).

[26]. S. Chelkowski, A. D. Bandrauk, A. Staudte, and P. B. Corkum, Phys. Rev. A **76**, 013405 (2007).

[27]. K. Codling and L. J. Frasinski, J. Phys. B **26**, 783 (1993).

[28]. P. B. Corkum, Phys. Rev. Lett. **71**, 1994 (1993).

[29]. P. B. Corkum and F. Krausz, Nat. Phys. **3**, 381 (2007).

[30]. P. B. Corkum, N. H. Burnett, and F. Brunel, Phys. Rev. Lett. **62**, 1259 (1989)

[31]. C. Cornaggia, J. Lavancier, D. Normand, J. Morellec, P. Agostini, J. P. Chambaret, and A. Antonetti, Phys. Rev. A **44**, 4499 (1991).

[32]. M. Dantus and V. V. Lozovoy, Chem. Rev. (Washington, D.C.) **104**, 1813 (2004).

[33]. P. Dietrich and P. B. Corkum, J. Chem. Phys. **97**, 3187 (1992).

[34]. V. G. Dmitriev, G. G. Gurzadyan, D. N. Nikogosyan, "Handbook of nonlinear Optical Crystals", Springer Series in Optical Sciences, Volume 64.

[35]. P. W. Dooley, I. V. Litvinyuk, K. F. Lee, D. M. Rayner, M. Spanner, D. M. Villeneuve, and P. B. Corkum, Phys. Rev. A **68**, 023406 (2003).

[36]. R. Dörner, V. Mergel, O. Jagutzki, L. Spielberger, J. Ullrich, R. Moshammer, H. Schmidt-Böcking, Physics Reports **330**, 95 (2000).

[37]. T. Ergler, A. Rudenko, B. Feuerstein, K. Zrost, C. D. Schröter, R. Moshammer, and J. Ullrich, Phys. Rev. Lett. **97**, 193001 (2006).

[38]. B. Feuerstein and U. Thumm, Phys. Rev. A **67**, 063408 (2003).

[39]. B. Feuerstein and U. Thumm, J. Phys. B **36**, 707 (2003).

[40]. B. Feuerstein, Th. Ergler, A. Rudenko, K. Zrost, C. D. Schröter, R. Moshammer, J. Ullrich, T. Niederhausen, and U. Thumm, Phys. Rev. Lett. **99**, 153002 (2007).

[41]. D. N. Fittinghoff, P. R. Bolton, B. Chang, and K. C. Kulander, Phys. Rev. Lett. **69**, 2642 (1992).

[42]. L. J. Frasinski, J. H. Posthumus, J. Plumridge, K. Codling, P. F.Taday, and A. J. Langley, Phys. Rev. Lett. **83**, 3625 (1999).

[43]. B. Friedrich and D. Herschbach, Phys. Rev. Lett. **74**, 4623 (1995).

[44]. B. Feuerstein and U. Thumm, Phys. Rev. A **67**, 043405 (2003).

[45]. A. Giusti-Suzor, X. He, O. Atabek, and F. H. Mies, Phys. Rev. Lett. **64**, 515 (1990).

[46]. A. Giusti-Suzor and F. H. Mies, Phys. Rev. Lett. **68**, 3869 (1992).

[47]. Guide for standard TOPAS model.

[48]. F. He, A. Becker, and U. Thumm, Phys. Rev. Lett. **101**, 213002 (2008).

[49]. I. V. Hertel and W. Radloff, Rep. Prog. Phys. **69**, 1897 (2006).

[50]. V. S. Popov, Physics-Uspekhi **47** (9), 855 (2004).

[51]. P. Johnsson, J. Mauritsson, T. Remetter, A. L'Huillier, and K.J. Schafer, Phys. Rev. Lett. **99**, 233001 (2007).

[52]. L. V. Keldish, Sov. Phys. JETP **20**, 1307 (1965).

[53]. M. F. Kling, Ch. Siedschlag, A. J. Verhoef, J. I. Khan, M. Schultze, Th. Uphues, Y. Ni, M. Uiberacker, M. Drescher, F. Krausz, and M. J. J. Vrakking, Science **312**, 246 (2006).

[54]. K. C. Kulander, F. H. Mies, and K. J. Schafer, Phys. Rev. A **53**, 2562 (1996).

[55]. F. Légaré, K. F. Lee, I. V. Litvinyuk, P. W. Dooley, A. D. Bandrauk, D. M. Villeneuve, and P. B. Corkum, Phys. Rev. A **72**, 052717 (2005).

[56]. I.V. Litvinyuk, K. F. Lee, P. W. Dooley, D.M. Rayner, D. M. Villeneuve, and P. B. Corkum, Phys. Rev. Lett. **90**, 233003 (2003).

[57]. M. Magrakvelidze, F. He, S. De, I. Bocharova, D. Ray, U. Thumm, and I. V. Litvinyuk, Phys. Rev. A, **79**, 033408 (2009).

[58]. M. Magrakvelidze, F. He, T. Niederhausen, I. V. Litvinyuk, and U. Thumm, Phys. Rev. A, **79**, 033410 (2009).

[59]. C. Maharjan Ph. D. thesis, KSU 2007.

[60]. F. Martín, J. Fernández, T. Havermeier, L. Foucar, Th. Weber, K. Kreidi, M. Schöffler, L. Schmidt, T. Jahnke, O. Jagutzki, A. Czasch, E. P. Benis, T. Osipov, A. L. Landers, A.

Belkacem, M. H. Prior, H. Schmidt-Böcking, C. L. Cocke, and R. Dörner, Science **315**, 629 (2007).

[61]. J. McKenna, W. A. Bryan, C. R. Calvert, E. M. L. English, J. Wood, D. S. Murphy, I. C. E. Turcu, J. M. Smith, K. G. Ertel, O. Chekhlov, E. J. Divall, J. F. McCann, W. R. Newell, and I. D. Williams, J. Mod. Opt. **54**, 1127 (2007).

[62]. I. Mercer, E. Mevel, R. Zerne, A. L'Huillier, P.Antoine, and C. -G.Wahlström, Phys. Rev. Lett. **77**, 1731 (1996).

[63]. L. Miaja-Avila, G. Saathoff, S. Mathias, J. Yin, C. La-o-vorakiat, M. Bauer, M. Aeschlimann, M. M. Murnane, and H. C. Kapteyn, Phys. Rev. Lett. **101**, 046101 (2008).

[64]. D. R. Miller, Atomic and molecular beam methods, vol. 1, ch. Free Jet Sources, p. 14ff, Oxford University Press, Oxford/New York, (1988).

[65]. D. S. Murphy, J. McKenna, C. R. Calvert, I. D. Williams, and J. F. McCann, New J. Phys. **9**, 260 (2007).

[66]. D. S. Murphy, J. McKenna, C. R. Calvert, W. A. Bryan, E. M. L. English, J. Wood, I. C. E. Turcu, W. R. Newell, I. D. Williams, and J. F. McCann, J. Phys. B **40**, S359 (2007).

[67]. H. Niikura, P. B. Corkum, and D. M. Villeneuve, Phys. Rev. Lett. **90**, 203601 (2003).

[68]. H. Niikura, D. M. Villeneuve, and P. B. Corkum, Phys. Rev. Lett. **92**, 133002 (2004).

[69]. H. Niikura, D. M. Villeneuve, and P. B. Corkum, Phys. Rev. A **73**, 021402(R)(2006).

[70]. T. Niederhausen Ph.D. thesis, KSU 2007.

[71]. G. G. Paulus, W. Becker, W. Nicklich, and H Walther, J. Phys. B **27** L703 (1994).

[72]. G. G. Paulus , W. Nicklich, H. Xu, P. Lambropoulos, and H. Walther, Phys. Rev. Lett. **72**, 2851 (1994).

[73]. G. G. Paulus , F. Grasbon, A. Dreischuh, and H. Walther, R. Kopold, and W. Becker Phys. Rev. Lett. **84**, 3791 (2000).

[74]. D. Pavicic, K. F. Lee, D. M. Rayner, P. B. Corkum, and D. M. Villeneuve, Phys. Rev. Lett. **98**, 243001 (2007).

[75]. G. Petite, P. Agostini, and H .G. Muller, J. Phys. B **21**, 4097 (1988).

[76]. J. H. Posthumus, Rep. Prog. Phys. **67**, 623 (2004).

[77]. W. H. Press, S. A. Teukolsky, W. T. Vetterling, and B. P. Flannery, Numerical Recipes Cambridge University Press, Cambridge, England, (1992).

[78]. http://www.roentdek.com

[79]. R. W. Robinett, Phys. Rep. **392**, 1 (2004).

[80]. F. Rosca-Pruna and M. J. J. Vrakking, Phys. Rev. Lett. **87**, 153902 (2001).

[81]. A. Rudenko, T. Ergler, B. Feuerstein, K. Zrost, C. D. Schröter, R. Moshammer, and J. Ullrich, Chem. Phys. **329**, 193 (2006).

[82]. H. Sakai, C. P. Safvan, J. J. Larsen, K. M . Hilligsøe, K. Hald, and H. Stapelfeldt, J. Chem. Phys. **110**, 10235 (1999).

[83]. K. Sändig, H. Figger, and T. W. Hänsch, Phys. Rev. Lett. **85**, 4876 (2000).

[84]. G. Sansone, E. Benedetti, F. Calegari, C. Vozzi, L. Avaldi, R. Flammini, L. Poletto, P. Villoresi, C. Altucci, R. Velotta, S. Stagira, S. De Silvestri, and M. Nisoli, Science **314**, 443 (2006).

[85]. K. J. Schafer, B. Yang, L. F. DiMauro, and K. C. Kulander , Phys. Rev. Lett. 70, 1599(1993)

[86]. T. Seideman, M. Yu. Ivanov, and P. B. Corkum, Phys. Rev. Lett. **75**, 2819 (1995)

[87]. A. Staudte, D. Pavičić, S. Chelkowski, D. Zeidler, M. Meckel, H. Niikura, M. Schöffler, S. Schössler, B. Ulrich, P. P. Rajeev, Th. Weber, T. Jahnke, D. M. Villeneuve, A. D. Bandrauk, C. L. Cocke, P. B. Corkum, and R. Dörner, Phys. Rev. Lett. **98**, 073003 (2007).

[88]. A. Staudte, S. Patchkovskii, D. Pavičić, H. Akagi, O. Smirnova, D. Zeidler, M. Meckel, D. M. Villeneuve, R. Dörner, M. Yu. Ivanov, and P. B. Corkum, Phys. Rev. Lett. **102**, 033004 (2009).

[89]. D. T. Strickland, Y. Beaudoin, P. Dietrich, and P. B. Corkum, Phys. Rev. Lett. **68**, 2755 (1992).

[90]. E. Siegman. LASERS. University Science Books, 1986.

[91]. U. Thumm, T. Niederhausen, and B. Feuerstein, Phys. Rev. A **77**, 063401 (2008).

[92]. X. M. Tong, Z. X. Zhao, and C. D. Lin, Phys. Rev. A **66**, 033402 (2002)

[93]. J. Ullrich, R. Moshammer, A. Dorn, R. Dörner, L. Ph. H. Schmidt and H. Schmidt-Böcking, Rep. Prog. Phys. **66** , 1463 (2003).

[94]. B. Walker, E. Mevel, B. Yang, P. Breger, J. P. Chambaret, A. Antonetti, L. F. DiMauro, and P. Agostini, Phys. Rev. A **48**, R894 (1993).

[95]. D. Williams, P. McKenna, B. Srigengan, I. M. G. Johnston, W. A. Bryan, J. H. Sanderson, A. El-Zein, T. R. J. Goodworth, W. R. Newell, P. F. Taday, and A. J. Langley, J. Phys. B **33**, 2743 (2000).

[96]. A. Zavriyev, P. H. Bucksbaum, J. Squier, and F. Saline, Phys. Rev. Lett. **70**, 1077(1993).

[97]. A. H. Zewail, J. Phys. Chem. A **104**, 5660 (2000).

[98]. T. Zuo and A. D. Bandrauk, Phys. Rev. A **52**, R2511 (1995).

Appendix A - Atomic units

The SI unit system is based on four constants of the nature: length - meter, time - second, mass - kilogram and current - ampere. In atomic physics it is more convenient to use atomic units where,

Atomic unit of action:	$\hbar$	=	1
Atomic unit of mass:	m_e	=	1
Atomic unit of charge:	e	=	1
Atomic unit of the Coulomb force constant:	$1/4\pi\varepsilon_0$	=	1

The unit of the length in atomic units set as Bohr radius of the hydrogen. The Bohr radius is the radius of the orbit of the electron in the ground state of the hydrogen:

$$a_0 = \frac{(4\pi\varepsilon_0)\hbar^2}{me^2} = 5.29177 \times 10^{-11} m \qquad \text{(A.1)}$$

The unit of the mass is taken as the mass of the electron, the unit of the charge is electrons charge, and unit of the angular momentum is ħ. The unit of the velocity is taken as velocity of the electron in the first Bohr orbit of hydrogen:

$$v_0 = \frac{e^2}{(4\pi\varepsilon_0)\hbar} = \alpha c \qquad \text{(A.2)}$$

where α is the fine structure constant and equal to 1/137 and c the speed of the light, so in atomic units speed of the light is 137 a.u..

In atomic units for energy we will have:

$$E_n = -\frac{Z^2}{2n^2} \qquad \text{(A.3)}$$

For hydrogen the energy in atomic units is -0.5 a.u. such that the atomic unit of the energy (which is called hartree) is 27.2 eV.

The table below summarizes the transition from atomic units to SI units.

dimension	formula	a.u.	SI units
length	a_0	1	5.29177×10^{-11} m
time	a_0/v_0	1	2.41888×10^{-17} s
mass	m_e	1	9.10938×10^{-31} kg
charge	q_e	1	1.60218×10^{-19} C
velocity	v_0	1	2.18769×10^{6} m/ s
intensity	$1/2\ c\varepsilon_0(e/(4\ \pi\varepsilon_0 a_0^2))^2$	1	3.50953×10^{16} W/cm^2
energy	$e^2/(4\ \pi\varepsilon_0 a_0)$	1	27.2116 eV = 1 hartree
momentum	$m_e v_0$	1	1.99285×10^{-24} kg m /s
angular momentum	$\hbar = a_0 m_e v_0$	1	1.05457 x 10−34 kg m^2/ s
frequency	$v_0/(2\pi a_0)$	1	6.57969×10^{15} Hz
angular frequency	v_0/a_0	1	4.13414×10^{16} Hz
action	$\hbar = e^2/(4\ \pi\varepsilon_0 v_0)$	1	1.05457×10^{-34} J s
electric field	$e/(4\ \pi\varepsilon_0 a^2{}_0)$	1	5.14221×10^{11} V/m
magnetic field	$\hbar/(e a_0^2)$	1	2.35052×10^{5} T

Table A.1 Transition from atomic units to SI units.

Appendix B - Jet velocity and temperature

Measuring jet velocity and temperature experimentally is straight forward. We measure (plot) the time of flight spectrum and 2D momentum of the target jet and background gas in the detector plane (x,y) (direction of the jet is along y axis, targets used were D_2 and H_2, and mostly H_2O and H_2 as background gases).

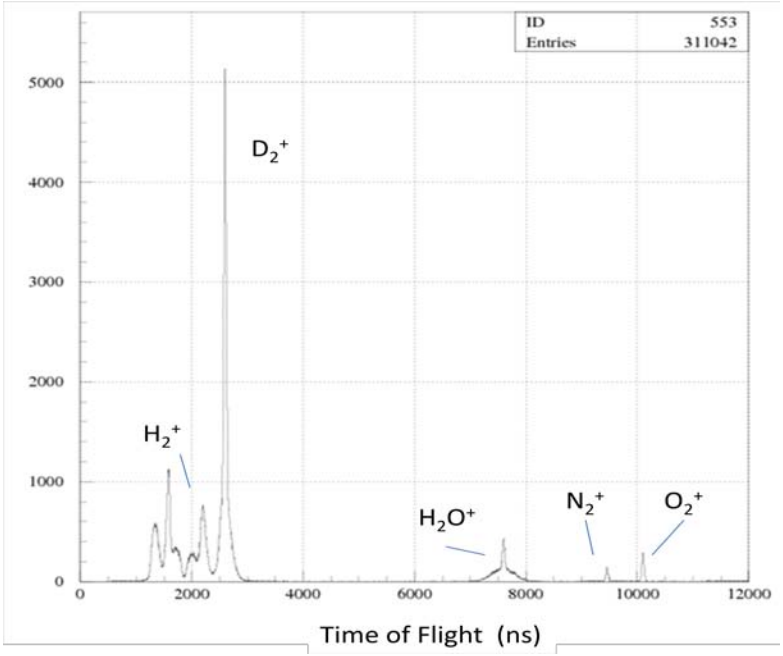

Fig. B.1 Time-of-flight plot for D_2 target.
The voltage across the spectrometer is 10V. The ion flight distance is 5.2 cm.

Fig. B.1. shows the time-of flight spectra for D_2 target. Gating on time-of-flight (TOF) for each background gas we plot the p_y distribution. Fitting it with the Maxwell-Boltzmann (Gaussian) distribution gives us the jet temperature and velocity. The Boltzmann distribution is given as:

$$f_{\vec{p}}(p_y) = \left(\frac{m}{2\pi k_B T}\right)^{1/2} \exp\left(-\frac{p_y^2}{2k_B T}\right) \qquad \text{(B.1.)}$$

where k_B is Boltzmann's constant.

We are fitting data using a Gaussian which has form: $y=y_0+A\exp(-(x-x_c)^2/(2w^2))$ where A corresponds to the term in front of the exponent in (B.1) and has units of sec/m $w^2=mk_BT$ and has units of inverse momentum squared. From Fig. B.1, using fitting parameters for the temperature we get:

$$T = \frac{(1.7\times1.99\times10^{-24}\ kg\ m/s)^2}{4\times1.66\times10^{-27}kg\times1.38\times10^{-23}J/K} = 124K = -149℃ \quad \text{(B.2)}$$

$$T = \frac{(5.5\times1.99\times10^{-24}kg\ m/s)^2}{18\times1.66\times10^{-27}kg\times1.38\times10^{-23}J/K} = 291K = 18℃ \quad \text{(B.3)}$$

where (B.2) corresponds to the temperature of the jet ions and the (B.3) corresponds to the hot background temperature.

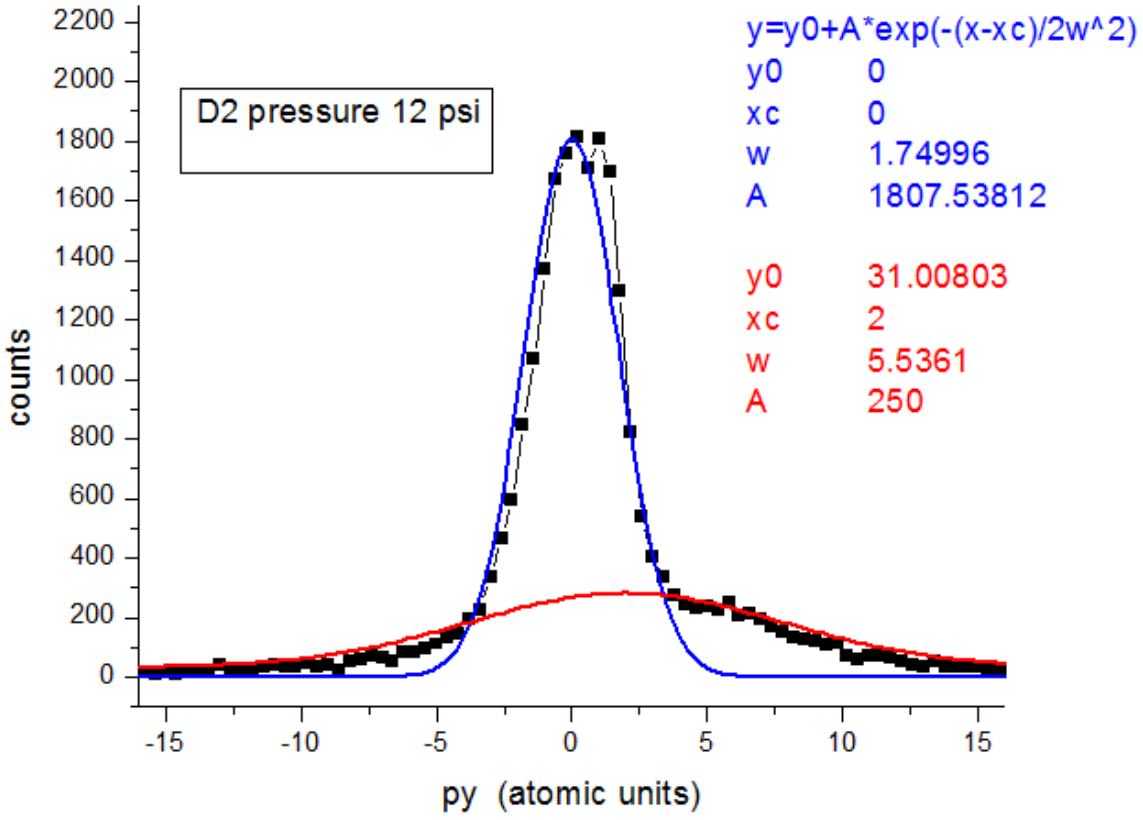

Fig. B.2 p_y momentum distribution for the H_2O background gas in the case of backing pressure 12 psi of the D_2 target.
The data is fitted using Gaussian as $y=y_0+Aexp(-(x-x_c)^2/(2w^2))$ where $w^2=mk_BT$, k_B is Boltzmann constant, $A=(m/(2k_BT\pi))^{0.5}$, x_c is the distance from the origin on x axis, y_0 on the y axis, w is $FWHM*2*(ln4)^{0.5}$. The blue fit corresponds to the D_2 ions and the red fit corresponds to the hot background.

The jet velocity relative to the background can be calculated using fitting parameter x_c (has units of the momentum in atomic units). From Fig. B.2, for the D_2 gas jet and gating on H_2O TOF we found x_c=2 relative to thebackground. $p_y=x_c$(at x=0) => $v_y=x_c/m$ where m is the mass of the D_2 in our case. Thus

$$v_{jet} = \frac{2\times1.99\times10^{-24}}{4\times1.66\times10^{-27}kg}\frac{kg\ m}{s} = 599.4\frac{m}{s}$$

Appendix C - OPA calibration

To ensure that we obtain correct signal and idler readings from the OPA we calibrated using a spectrometer. Fig. C.1 shows the calibration plot for counts vs. wavelength for this spectrometer.

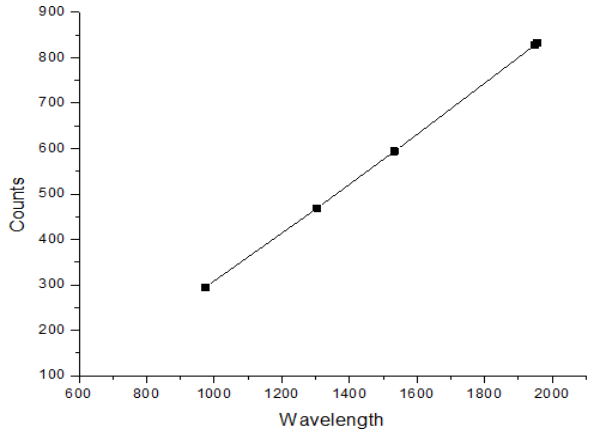

Fig. C.1 Spectrometer calibration

Table C.1 summarizes the OPA signal and the spectrometer counts, the third column is obtained using calibration curve in Fig. C.1.

OPA Signal	**Spectrometer count**	**Spectrometer wavelength (nm)**	**OPA Idler**	**Spectrometer count**	**Spectrometer wavelength (nm)**
1280	444	1239.6	2077.38	962	~2160
1310	464	1287.5	2002.93	900	~2075
1340	480	1317.5	1936.64	849	1993.2
1370	500	1353	1877.23	825	1942.8
1400	519	1385	1823.68	785	1880.1
1430	539	1422.96	1775.17	759	1825
1460	554	1450.5	1731.02	726	1769.5
1490	560	1460.5	1690.66	706	1729.4
1520	571	1485.7	1653.63	674	1674.5
1550	576	1490.9	1619.53	647	1623.95
1580	_	_	1588.02		
1610	_	_	1568.32		

Table C.1 OPA and spectrometer readings.

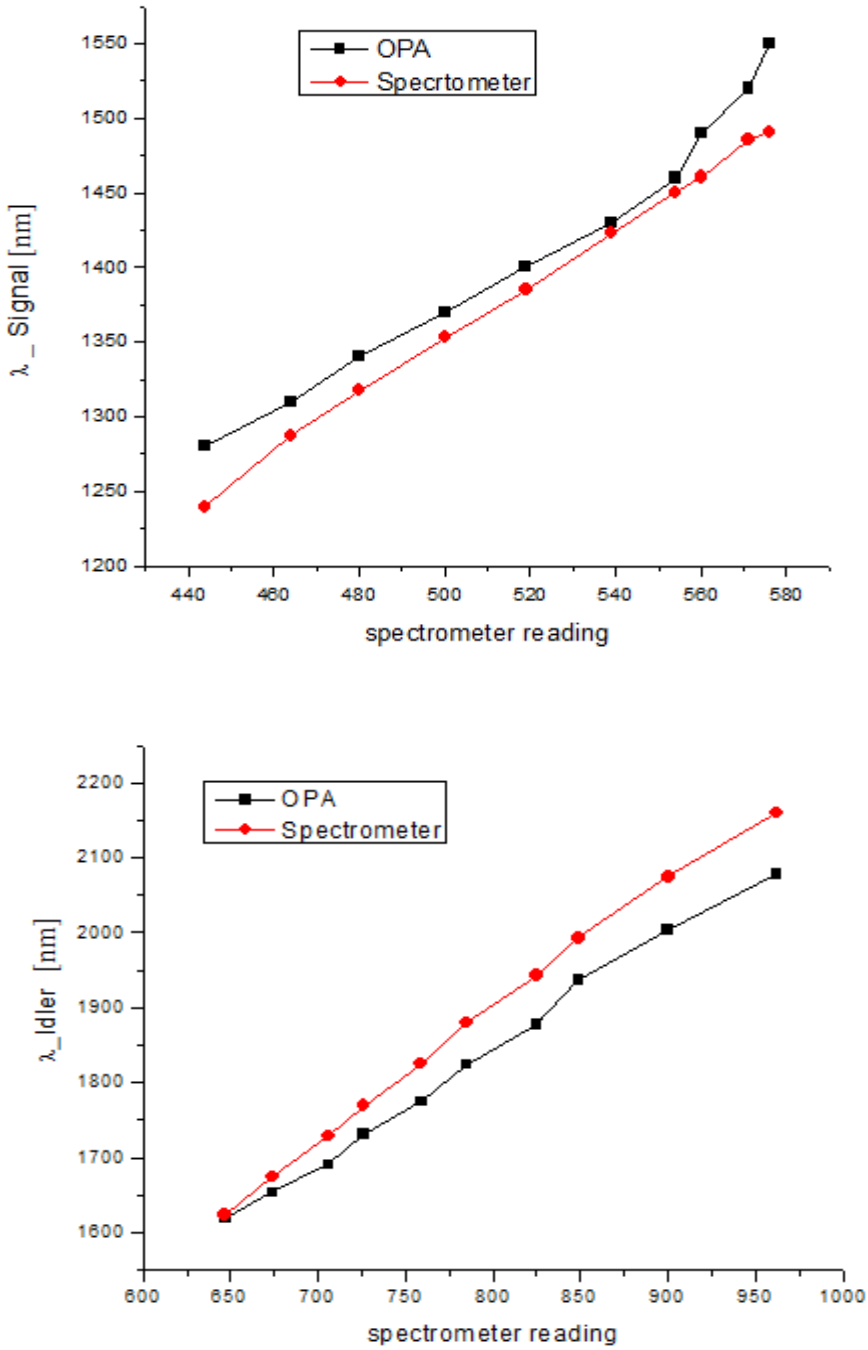

Fig. C.2 Comparing the software reading (OPA Black) with the spectrometer calibration (Spectrometer red) for Signal and Idler pulses.

The output from OPA Output: TOPAS (DM3 Closed) Polarization: S-V I-H			
S **wavelength(nm)**	**S+I** **energy (µJ)**	**S** **wavelength(nm)**	**S+I** **energy (µJ)**
1140	10	1420	280
1160	100	1440	270
1180	190	1460	260
1200	260	1480	245
1220	300	1500	215
1240	310	1520	210
1260	320	1540	160
1280	320	1560	85
1300	315	1580	35
1320	305	1600	35
1340	300	1620	
1360	295		
1380	290		
1400	280		

Table C.2 The OPA output datasheet provided by manufacturer.

Power outputs measured OPA entry power= 1.4 W						
(S) nm	**(I) nm**	**power (mW)**		**(S) nm**	**(I) nm**	**power (mW)**
1160	2496.52	7		1410	1806.99	390
1170	2451.43	10		1420	1790.83	375
1180	2408.66	20		1430	1775.17	380
1190	2368.04	55		1440	1760	365
1200	2329.41	110		1450	1745.29	360
1210	2292.63	210		1460	1731.02	350
1220	2257.57	230		1470	1717.17	345
1230	2224.11	310		1480	1703.72	320
1240	2192.14	330		1490	1690.66	300
1250	22161.57	362		1500	1677.97	270
1260	2132.31	370		1510	1665.63	250
1270	2104.27	390		1520	1653.63	200
1280	2077.38	400		1530	1641.95	190
1290	2051.57	410		1540	1630.59	200
1300	2026.77	410		1550	1619.53	160
1310	2002.93	405		1560	1608.75	130
1320	1980	420		1570	1598.25	120
1330	1957.92	400		1580	1588.02	110
1340	1936.64	385		1590	1578.05	100
1350	1916.13	400		1600	1568.32	60
1360	1896.34	410		1610	1568.32	50
1370	1877.23	415		1620	1549.57	-
1380	1858.78	405				
1390	1840.94	410				
1400	1823.68	405				

Table C.3 OPA output.

Appendix D - FORTRAN Code

Following is the subroutine (only part changing for each experiment) of the main program which analyses the raw data for electrons and ions and generates the Lab view plots. For more details see [9, 59].

```
c*************************************************************************************
c Filename:    analyse_labview.f
c Subroutines: analyse, booking, histout
c Functions:   tof_to_pe, coss, ceil, cubic
c Description: Analyzes data and generates all of the same spectra which
c              labview generates. This routine analyzes both electrons and
c              recoils.
c*************************************************************************************
c-------------------------------------------------------------------------------------
      subroutine analyse(tdc,cnt,counts,adc,nadc,scl,nscl,param)
C -------------------------------------------------------------------------------------
c ************************ Declare Variables ***************************************
       implicit none
       integer*4 cnt(32), adc(*),scl(*),nscl, nrec, nel, energy, counts(*)
       integer*4 mu1, mu2, qu1, qu2
       integer ln, rn, tn, bn, cpn, nadc, param, k,m,l, parama
       integer left, right, up, down, mcp, i
       real tdc(32,16),flux
       real tim, m1, m2, q1, q2, xshift, yshift, x, shift
       real s1, E1, z, s2, E2, E, s, q, Ef, sp
       real a1,a2,t1,t2,tofall,xr3,yr3,xr4,yr4,rtof3,rtof4,dif,sum
       real xr_20,yr_20,re,Ez,Exy,pz,py,px,rr
       real xe1,xe2, xe_0, ye1,ye2, ye_0, te1,te2,te_0
       real edx1,edx2, edy1,edy2, gxe, gye, re1,re2,tr_0
       real xr1,xr_0, yr1,yr_0, rtof1,rtof2, xr2,yr2, gx,gy, gxr,gyr
       real xesum, yesum, xesd, yesd, xrsum, yrsum, xrsd, yrsd, rr1d
       real pxe, pxe1, pye, pye2, pze, pze2,pze3, ppe,ppe2,pe1,pe2, le1
       real pev, totalr, temp, temp2,pp1,pp2, pe
       real tof_to_pe, rndm, coss, cos1, cos2           ! function
       real vy1, vy2, vz1, vz2, et1, et2
       real cosfi, fi, cosbt, betta, v1, v2
       real alpha, pxe_prime, pye_prime, theta, theta_prime, inc, dalpha
       real ppr, pr, prrx, prry, prrz, prrz2, prd, prs !pxr, pyr, pzr,
       real pxr(4), pyr(4), pzr(4), tsum, prd2, prdif
       real tsumxe, tsumye, tsumxr, tsumyr
       real rec(3,16),el(3,16)
```

```
      real omega, c
      real onex(16),twox(16),oney(16),twoy(16),cp(16),ec,xcm,ycm
      real xp,yp,angler,anglee
      real pau, vjet, PI, me, mu, mar, mn2
      real nx, ny, nz
      real dt, rtof0, etof, edx, edy
      real pxtot,pytot,pztot
      double precision cubic                    ! function
c ********************** Initialize Constants ************************************
      parameter (PI=3.14159265359)
      parameter (mu=1.661E-27)                  ! proton mass (kg)
      parameter (me=9.1094E-31)                 ! electron mass (kg)
      parameter (mar=6.634E-26)                 ! Argon atomic mass (kg)
      parameter (mn2=2.324E-26)                 ! N2 atomic mass (kg)
      data omega/0.224/ !GHz(B=gauss)cyclotron frequency calculated from wiggles
      data pau/1.993E-24/                        ! a.u. of momentum
      data ec/1.602E-19/                         ! electron charge
      data xesum/-89.56/                         ! electron time sums
      data xesd/4./
      data yesum/-88.88/
      data yesd/4./
      data xrsum/-107.64/                       ! recoil time sums
      data xrsd/2./
      data yrsum/-104.57/
      data yrsd/2./
      data gx/1.064/                            ! gain factor for electron detector
      data gy/1.064/                            ! 0.5[mm/ns]
      data gxr/1.064/                           ! gain factor for recoil detector
      data gyr/1.064/
      vjet=9.E-4                                !gyr*(delta(ns))/tof(ns)
      data te_0/-20./                           ! electron zero time
      data tr_0/-11./                           ! recoil zero time
c     data rtof0/1./                            ! recoil peak time in ns
      data xe_0/0.1/                            ! electron detector center
      data ye_0/0.6/
      data xr_0/0./                             ! recoil detector center
      data yr_0/0./
      data xr_20/0./                            ! recoil detector center
      data yr_20/0./
c ********************** Set Analyze Paramters ************************************
      s    = 0.235                              ! electron distance [m]
      s1   = 0.0636                             ! recoil distance [m]
```

```
      E    =100.                                  ! electric field [V/m]
      q    = 1.*ec                                ! electron charge
c***************** Set Charge and mass of recoil products*****************************
      q1 = 1*ec                                   ! charge of Ar(N2)+
      q2 = 1*ec                                   ! charge of Ar(N2)+
      m1 = 28.                                    ! mass of N2+
      m2 = 28.                                    ! mass of N2+
c     m1 = 40.                                    ! mass of Ar+
c     m2 = 40.                                    ! mass of Ar+

c ************* End of Constants and analyze parameters ******************************
c ************************** Time Sums ***********************************************
c******************** Calculate all Time Sums*****************************************
      tsumxe=-(2*tdc(10,1)-tdc(15,1)-tdc(16,1))
      tsumye=-(2*tdc(10,1)-tdc(3,1)-tdc(4,1))
      tsumxr=-(2*tdc(9,1)-tdc(5,1)-tdc(7,1))
      tsumyr=-(2*tdc(9,1)-tdc(6,1)-tdc(8,1))
c****************** populate Time Sum histograms************************************
      call hf1(1,tsumxe,1.)
      call hf1(2,tsumye,1.)
      call hf1(3,tsumxr,1.)
      call hf1(4,tsumyr,1.)
      call hf2(-1,tsumxe,tsumye,1.)
      call hf2(-2,tsumxe,tdc(1,1)-tdc(2,1),1.)
      call hf2(-4,tsumye,tdc(3,1)-tdc(4,1),1.)
      call hf1(-5,tdc(1,1)-tdc(2,1),1.)
      call hf1(-6,tdc(3,1)-tdc(4,1),1.)
c ***************************************************************************************
c ******************** Electron positions and MCP ************************************
c ******** Here we obtain the electron time and position data ************************
      left  = 15
      right = 16
      down  = 3
      up    = 4
      mcp   = 10
      ln = cnt(left)
      do i=1,cnt(left)
            onex(i)=tdc(left,i)+.5*rndm()
      enddo
      rn = cnt(right)
      do i=1,cnt(right)
            twox(i)=tdc(right,i)+.5*rndm()
```

```
      enddo
      bn = cnt(down)
      do i=1,cnt(down)
            oney(i)=tdc(down,i)+.5*rndm()
      enddo
      tn = cnt(up)
      do i=1,cnt(up)
            twoy(i)=tdc(up,i)+.5*rndm()
      enddo
      cpn = cnt(mcp)
      do i=1,cnt(mcp)
            cp(i)=tdc(mcp,i)+.5*rndm()
      enddo
      nel = 4
      call resort(nel,cp,cpn,onex,ln,twox,rn,     ! now resort the hits
      *            oney,bn,twoy,tn,
      *            xesum,yesum,xesd,yesd,
      *            el)
c     if(nel.lt.1.) return
c ***************************************************************************
c ********************** Analyze Electrons ***********************************
c ******* Here we analyze the electron time and position data ********************
      etof = tdc(11,1)-el(1,1)-te_0               ! electron time of flight
      edx1 = gx*el(2,1)                           ! mm/2  electron positions
      edy1 = gy*el(3,1)
      edx1 = edx1+xe_0
      edy1 = edy1+ye_0
      re = sqrt(edx1**2+edy1**2)
      c = tan(omega*etof/2.)
      re1  = sqrt((edx1+0)**2+(edy1-0)**2)
      pxe  = 5.E5*me*omega*(edx1/c+edy1)/(2.*pau) !electron momenta counter clockwise
      pye  = 5.E5*me*omega*(edy1/c-edx1)/(2.*pau)
c     pxe  = 5.E5*me*omega*(edx1/c-edy1)/(2.*pau)  !electron momenta  clockwise
c     pye  = 5.E5*me*omega*(edy1/c+edx1)/(2.*pau)
      pze  = (1.E9*me*s/etof - 1.E-9*E*q*etof/2.)/pau
      ppe  = sqrt(pxe**2+pye**2)
      pe   = sqrt(ppe**2+pze**2)           ! total electron momentum [a.u.]
      pev  = 27.2*pe**2/2.                 ! total electron momentum [eV]
      Ez =27.2*pze**2/2.
      Exy=27.2*ppe*2/2.
c ********************** End Analyze Electrons ***********************************
c ******************** Recoil positions and MCP ***********************************
```

```
c ******** Here we obtain the recoil time and position data **************************
       left  = 5
       right = 7
       down  = 6
       up    = 8
       mcp   = 9
c ********************************************************************************
c************************ Handle "param"*****************************************
c      parama=param/1000.+(1.+(-0.5*Rand()))
       parama=param+(1.+(-0.5*Rand()))
       param=parama
c********************** Done handling "param"*************************************
       ln = cnt(left)
       do i=1,cnt(left)
              onex(i)=tdc(left,i)+.5*rndm()
       enddo
       rn = cnt(right)
       do i=1,cnt(right)
              twox(i)=tdc(right,i)+.5*rndm()
       enddo
       bn = cnt(down)
       do i=1,cnt(down)
              ney(i)=tdc(down,i)+.5*rndm()
       enddo
       tn = cnt(up)
       do i=1,cnt(up)
              twoy(i)=tdc(up,i)+.5*rndm()
       enddo
       cpn = cnt(mcp)
       do i=1,cnt(mcp)
              cp(i)=tdc(mcp,i)+.5*rndm()
       enddo
       nrec=2
       call resort(nrec,cp,cpn,onex,ln,twox,rn,
       *            oney,bn,twoy,tn,
       *            xrsum,yrsum,xrsd,yrsd,
       *            rec)
c******************** Get recoil times of flight from the TDC************************
c      rtof=tdc(11,1)-rec(1,1)+tr_0
       rtof1=tdc(11,1)-rec(1,1)+tr_0
       rtof2=tdc(11,1)-rec(1,2)+tr_0
       rtof3=tdc(11,1)-rec(1,3)+tr_0
```

```
      rtof4=tdc(11,1)-rec(1,4)+tr_0
      do k=1,4
            tofall=tdc(11,1)-rec(1,k)+tr_0
            call hf1(553,tofall,1.)
      enddo
c********************* Retrieve position of the recoil hit*****************************
      xr1 = gxr*rec(2,1)
      yr1 = gyr*rec(3,1)
      call hf1(11,rec(2,1),1.)
      call hf1(12,rec(3,1),1.)
      xr2 = gxr*rec(2,2)
      yr2 = gyr*rec(3,2)
      call hf1(13,rec(2,2),1.)
      call hf1(14,rec(3,2),1.)
      rr = sqrt(xr1**2+yr1**2)
c     xr1 = gxr*rec(2,1)-xr_0
c     yr1 = gyr*rec(3,1)-yr_0
c     xr2 = gxr*rec(2,2)-xr_20
c     yr2 = gyr*rec(3,2)-yr_20
c********************** Reset hit position relative to the detector center************
c     xr1 = xr1+xr_0
c     yr1 = yr1+yr_0
c********************* Done with Recoil hit position*********************************
c     xp=xr1*cos(angler)+yr1*sin(angler)      !recoil detector rotation
c     yp=yr1*cos(angler)-xr1*sin(angler)
c     rr1=sqrt((xr1+0)**2+(yr1+5)**2)
c ***************************************************************************************
c ************************* Analyze Recoils ***************************************
c ******************* Here we analyze the recoil time and position data **************
      shift = 0.                ! usually varies from 10-25 for the sq room COLTRIMS
      xshift = shift*sqrt(m1*ec/q1)
      yshift = shift*sqrt(m2*ec/q2)
c     x      = (rtof1-xshift)*1E-9
c     tim    = 2.*s1*m1*mu/(q1*E*x)
c     tim    = (tim*1.E9 + yshift)
c********************** Calculate recoil momentums**********************************
      pzr(1) = (1.E9*m1*mu*s1/(rtof1-xshift)- 1.E-9*E*q1*(rtof1-xshift)/2.)/pau
      pyr(1) = (5.E5*m1*mu*(yr1-yr_0)/(rtof1-xshift))/pau
      pxr(1) = (5.E5*m1*mu*(xr1-xr_0)/(rtof1-xshift))/pau
      et1    = 27.2*((pxr(1))**2+(pyr(1))**2+(pzr(1))**2)/(2.*m1*1836.)
      pzr(2) = (1.E9*m2*mu*s1/(rtof2-yshift)- 1.E-9*E*q2*(rtof2-yshift)/2.)/pau
      pyr(2) = (5.E5*m2*mu*(yr2-yr_20)/(rtof2-yshift))/pau
```

```
       pxr(2) = (5.E5*m2*mu*(xr2-xr_20)/(rtof2-yshift))/pau
      et2    = 27.2*((pxr(2))**2+(pyr(2))**2+(pzr(2))**2)/(2.*m1*1836.)
c-------------------------------------------------------------------------------
       prrx   = pxr(1)-pxr(2)
       prry   = pyr(1)-pyr(2)
       prrz   = pzr(1)-pzr(2)
       pz = pzr(1)+pzr(2)
       py = pyr(1)+pyr(2)
       px = pxr(1)+pxr(2)
       prs = sqrt((px)**2+(py)**2+(pz)**2)
c      totalr = 27.2*((pxr(1)-pxr(2))**2+
c      *               (pyr(1)-pyr(2))**2+
c      *               (pzr(1)-pzr(2))**2)/(52.*1836.)
       totalr=et1+et2
c **************************** End Analyze Recoils **********************************
       pxtot = px+pxe
       pytot = py+pye
       pztot = pz+pze
c **************************** Fill Histograms ************************************
       call hf1(150,etof,1.)
       c if(pze.gt.0.) then
c      if (ppe.lt.5.) then
c      if (pxe.lt.0.5.and.pxe.gt.-0.5) then
c      if (pye.lt.0.5.and.pye.gt.-0.5) then
c      if(pze.lt.0.5.and.pze.gt.-0.5) then
       if (re.lt.50.) then
       call hf2(100,edx1,edy1,1.)
       call hf2(200,etof,re1,1.)
       call hf2(201,etof,edx1,1.)
       call hf2(202,etof,edy1,1.)
       call hf2(700,prs,totalr,1.)              ! Energy vs mom.
       call hf2(710,pxe,pye,1.)
       call hf1(720,pze,1.)
       call hf1(721,pxe,1.)
       call hf1(722,pye,1.)
       call hf1(723,ppe,1.)
       call hf2(730,pze,pye,1.)
       call hf2(740,pze,pxe,1.)
       call hf2(750,pze,ppe,1.)
       call hf1(3000,pev,1.)
       call hf1(3010,Ez,1.)
       call hf1(3020,Exy,1.)
```

```
c      end if
c      end if
c 11   end if
c 12   end if
c 13   end if
c 14   end if
c      end if
       call hf2(510,xr1,yr1,1.)
       call hf2(511,xr2,yr2,1.)
       if(tofall.gt.18800.and.tofall.lt.19650.) then
c      if (rr.gt.60.) then
       call hf1(311,pxtot,1.)
       call hf1(312,pytot,1.)
       call hf1(313,pztot,1.)
       call hf2(400,pev,totalr,1.)
       call hf1(520,px,1.)
       call hf1(521,py,1.)
       call hf1(522,pz,1.)
       call hf1(530,pzr(1),1.)
       call hf1(531,pzr(2),1.)
       call hf1(551,rtof1,1.)
       call hf1(552,rtof2,1.)
       sum = rtof1 + rtof2
       dif = rtof2 - rtof1
       call hf2(600,rtof1,rtof2,1.)                ! Pipico
       call hf2(650,sum,dif,1.)                    ! Rotated Pipico
       call hf2(800,pzr(1),pyr(1),1.)              ! Recoil momentum
       call hf2(930,(param/1000.),totalr,1.)       ! KER
       call hf1(931,totalr,1.)
c      endif
c      endif
       end if
       end if
       end
c ********************** End Fill Histograms ***************************************
C-------------------------------------------------------------------------------------
      subroutine booking(histfile)
C-------------------------------------------------------------------------------------
      call hbook1(1,'Electron Time Sum X',50,-100.,-50.,0.)
       call hbook1(2,'Electron Time Sum Y',50,-100.,-50.,0.)
       call hbook1(3,'Recoil Time Sum X',50,-130.,-80.,0.)
       call hbook1(4,'Recoil Time Sum Y',50,-130.,-80.,0.)
```

```
      call hbook1(11,'rec21',50,-100.,100.,0.)
      call hbook1(12,'rec31',50,-100.,100.,0.)
      call hbook1(13,'rec22',50,-100.,100.,0.)
      call hbook1(14,'rec32',50,-100.,100.,0.)
      call hbook2(100,tEDetect,300,-100.,100.,300,-100.,100.,0.)! Elec Detector
      call hbook1(150,'etof1',300,-10.,500.,0.)
      call hbook2(200,tWiggle,600,0.,300.,500,0.,130.,0.)       ! Wiggles
      call hbook2(201,'x; etof; edx',250,0.,300.,250,-200.,200.,0.)
      call hbook2(202,'y; etof; edy',250,0.,300.,250,-200.,200.,0.)
      call hbook1(311,'pxtot',800,-100.,100.,0.)
      call hbook1(312,'pytot',800,-100.,100.,0.)
      call hbook1(313,'pztot',800,-100.,100.,0.)
      call hbook2(400,'Eelectr,Erecoil',450,0.,50.,450,0.,50.,0.)
      call hbook2(510,tRDetect,100,-5.,5.,100,-5.,5.,0.)        !Recoil Detector
      call hbook2(511,'xy r2',100,-5.,5.,100,-5.,5.,0.)
      call hbook1(520,'pxr',800,-100.,100.,0.)
      call hbook1(521,'pyr',800,-100.,100.,0.)
      call hbook1(522,'pzr',800,-100.,100.,0.)
      call hbook1(530,'pzr1',450,-100.,100.,0.)
      call hbook1(531,'pzr2',450,-100.,100.,0.)
      call hbook1(551,'rtof1',350,0.,19000.,0.)
      call hbook1(552,'rtof2',350,0.,19000.,0.)
      call hbook1(553,'rtofall',350,0.,20000.,0.)
      call hbook2(600,tPipico,400,0.,8000.,400,0.,8000.,0.)     ! Pipico
c     call hbook2(601,tPipico,400,0.,2000.,400,0.,2000.,0.)     ! Gated Pipico
      call hbook2(650,tPipRot,400,0.,8000.,400,-4000.,4000.,0.) ! Rotated Pipico
c     call hbook2(651,tPipRot,400,1500.,3000.,400,0.,1500.,0.)  ! Rotated+gated
      call hbook2(700,'tEvsP',200,0.,200.,400,0.,40.,0.)        ! Energy vs mom
      call hbook2(710,'e px py; pxe; pye',250,-4.,4.,250,-4.,4.,0.)
      call hbook1(720,'pze',450,-10.,10.,0.)
      call hbook1(721,'pxe',450,-10.,10.,0.)
      call hbook1(722,'pye',450,-10.,10.,0.)
      call hbook1(723,'ppe',450,-10.,10.,0.)
      call hbook2(730,'e pz py;pze;pye',250,-4.,4.,250,-4.,4.,0.)
       call hbook2(740,'e pz px;pze;pxe',250,-4.,4.,250,-4.,4.,0.)
      call hbook2(750,'e pz ppe;pze;ppe',250,-4.,4.,250,0.,4.,0.)
      call hbook2(800,'Recoil mom;pzr;pyr',350,-50.,50.,350,-50.,50.,.0)
      call hbook2(930,'KER;Delay (fs);KER',20,0.,100.,2400,0.,20.,.0)
      call hbook1(931,'totalr',450,1.,50.,0.)
      call hbook1(3000,'total electron Energy (eV)',300,-1.,100.,0.)
      call hbook1(3010,' Energy z comp (eV)',300,-1.,100.,0.)
      call hbook1(3020,' Energy xy comp (eV)',300,-1.,100.,0.)
```

```
      end
c ********************** End Book Histograms ***************************************
c ***************************** Helper Subroutine ***********************************
C--------------------------------------------------------------------------------------
      real function tof_to_pe(tof)
C--------------------------------------------------------------------------------------
      implicit none
      real tof, pau
      real s1,e1,s2,e2,q,m
      real a1,a2,t,t1,result
      real cubic          ! function
      pau = 1.993E-24     ! 1 a.u. of momentum
      q   = 1.602E-19
      m   = 9.1094E-31
      s1  = .006          ! m
      E1  = 344.7         ! V/m
      s2  = .15
      E2  = 0.
      a1  = q*E1/m
      a2  = q*E2/m
      t   = tof*1.E-9     ! to get time in secs
c     te2 = etof2*1.E-9
c     te1 = etof1*1.E-9
      t1  = cubic(t*(2*a2-a1)/(a1-a2),   ! general case
     *            (2*s1+2*s2-a2*t*t)/(a1-a2),
     *            t*2*s1/(a2-a1))
c     t1  = cubic(-t,6*s1/a1,-2*t*s1/a1) ! s2=2s1 drift
      result = m*(s1/t1-a1*t1/2.)
      tof_to_pe = result/pau
      end
C--------------------------------------------------------------------------------------
      subroutine normal(x1, y1, z1, x2, y2, z2, nx, ny, nz)
C--------------------------------------------------------------------------------------
      implicit none
      real x1, y1, z1, x2, y2, z2, nx, ny, nz, x, y, z
      real l1, l2, l3
      x  = (y1*z2-y2*z1)
      y  = (z1*x2-z2*x1)
      z  = (x1*y2-x2*y1)
      l1 = sqrt(x1*x1+y1*y1+z1*z1)
      l2 = sqrt(x2*x2+y2*y2+z2*z2)
      l3 = sqrt(x*x+y*y+z*z)
```

```
       if(l1.eq.0.or.l2.eq.0.or.l3.eq.0.) then
              nx = 0.
              ny = 0.
              nz = 0.
       else
              nx = x/l3
              ny = y/l3
              nz = z/l3
       endif
       end
C-------------------------------------------------------------------------------
       real function coss(x1, y1, z1, x2, y2, z2)
C-------------------------------------------------------------------------------
       implicit none
       real x1, y1, z1, x2, y2, z2
       real scal, l1, l2
       scal = x1*x2+y1*y2+z1*z2
       l1   = sqrt(x1*x1+y1*y1+z1*z1)
       l2   = sqrt(x2*x2+y2*y2+z2*z2)
       if(l1.eq.0..or.l2.eq.0.) then
              coss = 0.
       else
               coss = scal/(l1*l2)
       endif
       end
C-------------------------------------------------------------------------------
       integer function ceil(x)
C-------------------------------------------------------------------------------
       implicit none
       real x
       if(x-int(x).eq.0.) then
              ceil = int(x)
       else
              ceil = int(1.+x)
       endif
       end
C-------------------------------------------------------------------------------
      subroutine histout
C-------------------------------------------------------------------------------
c      call hindex
c      call hrput(0,histfile,'N')
       call hrout(0,icycle,' ')
```

```
      call hrend('als98')
      close(1)
      end
C-------------------------------------------------------------------------------
      real function cubic(a,b,c)
c     the real root of the cubic equation with coefficients 1,a,b,c
c     MAKE SURE TO CHOOSE THE RIGHT ROOT IN CASE OF 2 OR 3 REAL
C-------------------------------------------------------------------------------
      implicit none
      real a, b, c
      double precision n, aa, bb, cc, q, r, d, s, t, z, z2, z3, PI
      PI = 3.14159265359
      n  = 2.0E-8
c     n  = EXP(((log(sqrt(a*a))+2*log(sqrt(b*b))
c     *        +3*log(sqrt(c*c))))/14.)
      aa = a/n
      bb = b/n**2
      cc = c/n**3
      q  = (3.*bb-aa*aa)/9.
      r  = (9.*aa*bb-27.*cc-2.*aa*aa*aa)/54.
      d  = q*q*q + r*r
      if(d.le.0.)then
            t  = acos(r/sqrt(-q*q*q))
            z3 = 2.*sqrt(-q)*cos(t/3.) - aa/3 !real root #1 right most
            z2 = 2.*sqrt(-Q)*cos((T+2.*PI)/3.) - aa/3.; ! real root #2
            z  = 2.*sqrt(-Q)*cos((T+4.*PI)/3.) - aa/3.; !real root #3 same if D=0
      else
            if(r+sqrt(d).gt.0.) then
                  s = (R+sqrt(D))**(1./3.)
            else
            s = -(-R-sqrt(D))**(1./3.)
            endif
      if(r-sqrt(d).gt.0.) then
            t = (R-sqrt(D))**(1./3.)
       else
            t = -(-R+sqrt(D))**(1./3.)
      endif
            z = s + t - aa/3.
      endif
      cubic = z*n
        end
c ************************* End Helper Subroutines*************************
```